CRANFIELD UNIVERSITY

CRANFIELD DEFENCE AND SECURITY

PhD Thesis

Academic Year 2012-2013

D WOOD

Shock propagation in a complex laminate

Supervisors: P Hazell
And
G Appleby-Thomas

October 2012

This thesis is submitted in partial fulfillment of the requirements for the degree of Doctor of Philosophy

Abstract

The shock response of a complex laminate has been investigated using a single stage gas gun, with manganin pressure gauges employed to investigate the shock profile. The complex laminate investigated was known by the acronym TWCP and is a tape wrapped carbon fibre composite with phenolic resin matrix. Carbon fibre composites are used in the aerospace industry due to their high strength to weight ratio, so understanding of different loading conditions is needed. To investigate the shock response of the TWCP, four weave orientations were studied. The orientations investigated with respect to the shock front were 0° (parallel to the shock front or perpendicular to the direction of travel), 25°, 45° and 90° (perpendicular to the shock front or parallel to the direction of travel). As well as the TWCP the shock response of the matrix material, a phenolic resin Durite SC-1008 was also investigated.

For the phenolic resin matrix material a non-linear Hugoniot was found in the U_S-u_p plane with the equation of $U_S = 2.14 + 3.79u_p - 1.68u_p^2$. Such non-linear Hugoniot behaviour has been seen in other polymeric materials, *e.g.* PMMA. In the pressure-volume plane deviation was seen in the higher pressure data most likely due to the materials non-linear response.

For the TWCP composite, linear Hugoniots were found for all four orientations with the corresponding equations shown below.

- 0° $U_S = 3.69 + 0.59u_p$
- 25° $U_S = 3.45 + 0.73u_p$
- 45° $U_S = 3.44 + 1.12u_p$
- 90° $U_S = 3.96 + 0.46u_p$

The four Hugoniots are comparable in nature and it is possible to assign a single Hugoniot with the equation $U_S = 3.56 + 0.84u_p$ through the majority of data points. The largest deviation from this "average" response was obtained from the 90° orientation due to the high elastic sound speed of this weave angle. Convergence was also seen between the Hugoniots in the U_S-u_p plane towards the higher u_p values (approximately 1 mm μs^{-1}). In the pressure-u_p plane there was very little difference between all of the experimental data, meaning that for the stress in this material, orientation makes no difference.

Contents

List of Figures

List of Tables

Nomenclature

Symbol	Units	Meaning
A	cm^2	Area
β		A constant of the material and gauge
c_B	mm μs^{-1}	Bulk sound speed
C_{ij}	GPa	Elastic constants
c_L	mm μs^{-1}	Longitudinal sound speed
c_0	mm μs^{-1}	Intercept of the Hugoniot
c_S	mm μs^{-1}	Shear sound speed
Δ_{el}	GPa	The Manganin gauge response in the elastic region
ΔR	Ω	Change in resistance of the manganin gauge
Δ W		Work done
E	GPa cm^3 g^{-1}	Internal energy
E	GPa	Young's modulus
ε		Strain
ε_v		Volumetric strain of the gauge
F	N	Force
G	GPa	Shear modulus
G_g	GPa	The Lamé constant of the gauge
K	GPa	Bulk modulus
L	GPa	Longitudinal modulus
m	g cm^{-3}	Mass
M_g	GPa	Longitudinal modulus for the manganin gauge
M_m	GPa	Modulus of the sample material
P	GPa	Pressure in the sample
ρ	g cm^{-3}	Density of the material
ρ_0	g cm^{-3}	Initial density of the material
R_0	Ω	Resistance of the manganin Gauge
S	Unitless	Slope of the Hugoniot
σ_x	GPa	Longitudinal stress in the sample. This takes into consideration any strength the material has

Symbol	Units	Meaning
σ_y	GPa	Lateral stress of the sample (perpendicular to the direction of the shock wave)
T	K	Temperature
t	Seconds	Time
τ	GPa	Shear strength
u_0	mm μs^{-1}	Initial particle velocity
u_p	mm μs^{-1}	Particle velocity
U_S	mm μs^{-1}	Shock velocity
V	cm^3 g^{-1}	Volume
V	V	Voltage
ν	Unitless	Poisson's ratio
Y	GPa	Yield strength
Y_g	GPa	Yield strength of the gauge
Z	mm μs^{-1}	Impedance

Acknowledgements

I would primarily like to thank my family for helping me reach this point in my life, especially my parents for all of their support. I would also like to thank my friends for the support given over the years, especially the guys I have shared an office with (James W, James L and Mike) for useful scientific talks. I also have to say thank you to Andrew Roberts for teaching me the techniques needed to perform the experiments as well as helping me fix the gun when I broke it. Also thank you Paul and Gareth for helping me along my path of learning at Cranfield University during the PhD. For the more random thanks I have to give a mention to the greatest band in the world Iron Maiden, the best music to write a thesis to. Read on to see if the answer is 42 and "so long and thanks for all the fish"[1].

[1] Douglas Adams, Hitchhikers to the Galaxy

Chapter 1

Introduction

The purpose of this thesis is to investigate the shock response of a complex laminate, where laminates are a subdivision of composites. More specifically the composite that was researched here is a type of carbon fibre composite known as TWCP which is a tape wrapped carbon fibre composite which has a phenolic resin matrix. Composites are materials that consist of at least two distinct constituents, which have different properties [1, Pages 1-3]. Depending on the constituents used the internal geometries can be complex in nature. Applications in which composites are used are extremely diverse and can range from explosives [2], to potting compounds for electronics [3], armour materials [4], materials in the aerospace industry [4, 5, 6] or even the automotive industry [7, 8]. In the context of fibre reinforced systems there tend to be two phases, a reinforcement phase, where most of the strength is derived and a continuous phase, known as the matrix material. An example of the most recent use of carbon fibre composites is in the Boeing Dreamliner 787 [9]. With this aerospace vehicle the fuselage, majority of the wings, and several other primary structures are predominantly made of carbon fibre composites. Composites are highly beneficial for such applications due to their high strength to weight ratio. Due to these properties fuel efficiency is increased in this transcontinental aircraft, while allowing the retention of the range and speed of a medium aircraft. Due to these benefits composites are becoming ever more prevalent within multiple industries, not just

the aerospace industry. During the lifetime of aerospace vehicles, multiple conditions will be encountered such as impacts from birds or small objects for aeroplanes; or plasma, radiation, micrometeor impact or the stress associated with initial launch for spacecraft [10]. These conditions will lead to a wide range of impact parameters which will include, but are not exclusive to, shock loading. Shock loading is a worst case scenario, but an important one due to the possible catastrophic failure it can lead to. Due to this it is important to understand how shock waves interact with composites under a variety of loading conditions.

Experiments have been performed on multiple composite materials in the shock regime. Millett *et al.* [3] performed shock impact on a simple composite. The composite in question was an epoxy resin doped with alumina particulates, *e.g.* the types of material used as potting compounds in electronics. They found that higher alumina percentages led to shock behaviour being offset from the epoxy only Hugoniot by a consistent amount.

The more common type of composites investigated are fibre reinforced composites. These have either unidirectional fibres (all orientated in one direction) or fibre weave in a usually plastic matrix. Many different types of fibres can be used for example carbon (the type of fibre concerned here), glass, aramid (*e.g.*kevlar) among others.

Work on glass fibre composites under shock loading has been performed by multiple authors including Tsai *et al.* [11], Dandekar *et al.* [12, 13], Millett *et al.* [14] and Zaretsky *et al.* [15]. It was found using plate impact experiments that for glass fibre composites, a thicker sample will lead to a longer rise time. The Hugoniot for the composite sat between the Hugoniot's of the resin material and the glass fibres. Orientation of the fibres has an important effect on the shock response of these composites. By orientating the fibres so that the fibres are parallel to the shock direction, a ramped rise for the traces was seen at lower velocities, whereas at higher velocities a precursor was seen. The matrix material at low velocities dominated the behaviour of the composite, with this dominance disappearing as the velocity was increased.

The shock response of carbon fibre composites has been investigated amongst others

by Millett *et al.* [16], Hazell *et al.* [17], Willows *et al.* [18] and Burrell *et al.* [19]. Some similar behaviour was noted for carbon fibre composites under shock loading as was seen with the glass fibre composites discussed above, with the shock loading again induced using the plate impact technique. The thickness again affected the rise time of the diagnostic method, with a thicker sample leading to a longer rise on the shock profile traces. Again orientation was found to be important with a precursor seen on the rise of the trace. Bordzilovsky *et al.* [20] investigated this in greater detail using an aramid fibre composite. It was found that the precursor became less pronounced as the angle with respect to the shock front was decreased. The effect of angle is important as with some applications it has been found that a 20° orientation provides the best compromise between ablation and strength [19].

1.1 Aims and Scope

The carbon fibre composite investigated here was a tape wrapped carbon fibre composite with phenolic resin known by the acronym TWCP. Due to the use of 20° composites in industry, it is important to understand the effect that angle has on the shock response of composites in general. For this reason four different orientations of TWCP were investigated, which were (with respect to the shock front) 0°, 25°, 45° and 90°. As the matrix material is important in the lower shock pressure regime response as discussed by Zaretsky *et al.* [15], the matrix material of the composite was also investigated independently. This was a phenolic resin known as Durite SC-1008. The aim in investigating both the resin and the composite was to obtain as great an understanding of the shock response as possible.

The shock response of the composite and resin were investigated using a single stage light gas gun, with manganin pressure gauges as the primary diagnostic. Longitudinal orientated manganin gauges were used to obtain the shock velocity as well as the pressure in the sample, while laterally orientated gauges provided data on the strength profile of

the material.

Chapter 2

Literature Review

2.1 Shock Waves

A shock wave forms when the velocity of a travelling wave becomes greater than the sound speed of the medium it is travelling through [21]. Once the shock wave has formed, this provides a discontinuity in material properties which include, but are not exclusive to, pressure, temperature, energy and density [22, Page 98]. When a shock wave interacts with an object many properties are altered including its structure (*e.g.* its shape or volume). This becomes problematic for three-dimensional objects which have complex shapes as the shock wave interaction within the object will also be complicated in nature. Consequently it becomes more difficult to understand what is occurring in extended three-dimensional objects. To get around this problem, experiments are devised that are one-dimensional in nature, for a finite amount of time. This allows the analysis of the shock wave interaction to be simplified, thereby facilitating understanding of how the materials themselves behave while under shock loading [23, Pages 4-5].

One-dimensional shock loading within a target results in inertial confinement, meaning that radial flow does not occur in the target centre. Consequently, under such loading conditions Equations 2.1 and 2.2 apply for isotropic materials (with the x direction representing the impact axis) [24]; *e.g.* a one-dimensional state of strain, but not stress, is

established.

$$\varepsilon_x \neq 0 \;\; \varepsilon_y = \varepsilon_z = 0 \tag{2.1}$$

$$\sigma_x \neq \sigma_y = \sigma_z \neq 0 \tag{2.2}$$

To fully understand the behaviour of shocked materials five key parameters are needed. These parameters are shock velocity U_S, particle velocity u_p, density ρ, pressure P and internal energy E. The particle velocity u_p refers to the velocity of the elements which are propagating the shock wave with velocity U_S in the medium. The particle velocity is the velocity of the continuum elements propagating the shock wave, whereas the shock velocity is a measure of how fast the shock wave is travelling through the medium in question. By definition the particle velocity is always slower than that of the shock front [25]. Figure 2.1 shows a simplified shock wave passing through a medium. In this figure the shock wave is moving from left to right. Everything behind the shock front (to the left) in the material is shocked, while everything ahead of it (to the right), is in the original material state. A subscript 0 on a parameter denotes an initial or unshocked state.

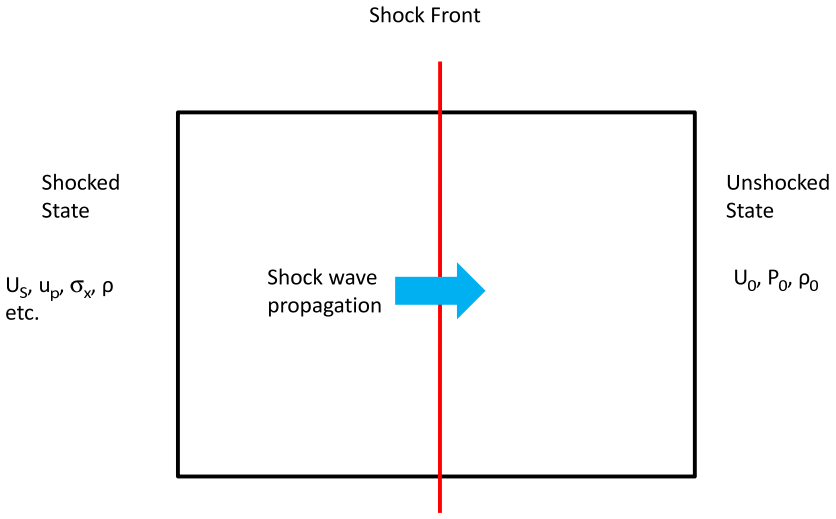

Figure 2.1: Representative diagram of a shock wave interacting with a material.

Only two shock parameters are needed to fully define the shock response of a material, as a set of conservation relations known as the Rankine-Hugoniot equations can be used to obtain the other parameters. The Rankine-Hugoniot equations [22, Pages 116-117] are based on the principles of conservation of energy, mass and linear momentum. The conservation equations can be used due to the system being closed or self contained. The derivations of the following equations were obtained from Reference [22, Pages 102-104].

In these Equations u_0 is the initial particle velocity which can be taken as 0 (if the material is unshocked), and σ is the compressive stress acting on the material. This compressive stress can be equal to pressure (P) if the material is in a hydrodynamic state, *e.g.*, liquid or if the magnitude of the stress greatly exceeds the shear strength of the material [23, Page 26].

The equation for the conservation of mass is shown in Equation 2.3. From the reference frame of the laboratory, before the shock enters the material it is travelling at a velocity of U_S-u_0 towards the material. After the shock wave enters the material, the material is compressed by the amount U_S-u_p. This also increases the density to ρ, to compensate for the decrease in volume. The leads to Equation 2.3 which represents the mass balance over the shock front in terms of cross sectional area.

$$\rho(U_S - u_p)dt = \rho_0(U_S - u_0)dt = m \tag{2.3}$$

Conservation of momentum requires the difference in momentum across the shock front to be equal to the impulse (the force required to change the momentum). Momentum is given by mass multiplied by the velocity, with impulse given by force multiplied by the change in time. Consequently, the difference in momentum is given by Equation 2.4 with impulse given by Equation 2.5. Equating impulse and change in momentum leads to Equation 2.6 which then simplifies to Equation 2.7 and finally Equation 2.8 if the initial particle velocity, u_0, is assumed equal to zero. Equation 2.8 is extremely useful and allows derivation of strengthless (hydrodynamic) pressure when the U_S-u_p state is known.

$$\Delta Momentum = \rho A(U_S - u_p)dtu_p - \rho_0 A(U_S - u_0)dtu_0 \tag{2.4}$$

$$Impulse = Fdt = (PA - P_0A)dt \tag{2.5}$$

$$A\rho(U_S - u_p)u_p dt - A\rho_0(U_S - u_0)u_0 dt = (P - P_0)Adt \tag{2.6}$$

$$\rho_0(U_S - u_0)(u_p - u_0) = P - P_0 \tag{2.7}$$

$$P - P_0 = \rho_0 U_S u_p \tag{2.8}$$

Finally, the conservation of energy equation is found by using the difference in work performed on the system either side of the shock front, as shown in Equation 2.9; where PA and P_0A are equal to the force, and $u_p dt$ and $u_0 dt$ relate to the distance over which the shock wave has compressed the material, acting behind and ahead of the shock front respectively.

$$\Delta W = (PA)(u_p dt) - (P_0 A)(u_0 dt) \tag{2.9}$$

To get the difference in total energy, which in this case is kinetic energy plus the internal energy, Equation 2.10 is used.

$$\Delta E = [\rho A(U_S - u_p)dt]u_p^2 + EA\rho(U_S - u_p)dt - \left(\frac{1}{2}[A(U_S - u_0)dt]u_0^2 + E_0 A\rho_0(U_S - u_0)dt\right) \tag{2.10}$$

By equating work done ΔW (Equation 2.9) and internal energy ΔE (Equation 2.10), and setting u_0 to zero as the system is initially unshocked, Equation 2.11 may ne obtained.

$$Pu_p = \frac{1}{2}\rho(U_S - u_p)u_p^2 - E_0\rho_0 U_S + E\rho(U_S - u_p) \tag{2.11}$$

This equation can then be simplified using the equations derived earlier leading to Equation 2.12.

$$E_1 - E_0 = \frac{1}{2}(P_1 + P_0)(V_0 - V) \tag{2.12}$$

When monitoring shock propagation the parameters measured are dependent on the diagnostic technique employed, with the variables investigated in this study being U_S and pressure (or σ_x if the material has strength). From these experimental values the Hugoniot relationship (the locus of available jump states) can be calculated. In essence, through individual experiments performed at different conditions the materials equation of state (the Hugoniot relationship) can be found. This is mainly represented in two planes, producing relationships known as the U_S-u_p, and the pressure-volume Hugoniot equations. In the U_S-u_p plane the equation tends to be linear in nature following Equation 2.13; however non-linear relationships do occur, and in such cases a second order quadratic equation, of the form shown in Equation 2.14, may be employed. Such non-linear behaviour has been seen in multiple polymers, for example PMMA [26], polyurethane replacement resin [27] and very many others (as seen by Cater and Marsh [28]). Such behaviour is discussed in much greater detail in Section 2.4. A generic trace for the U_S-u_p plane is shown in Figure 2.2. In this trace a linear Hugoniot can be fitted through the data with the equation $U_S = 2 + 1u_p$. Here the intercept c_0, which would be comparable to c_B for simple metals, is 2 mm μs^{-1}, with the value of S being 1 (S is unitless in nature).

$$U_S = c_0 + Su_p \tag{2.13}$$

$$U_S = c_0 + S_1 u_p + S_2 u_p^2 \tag{2.14}$$

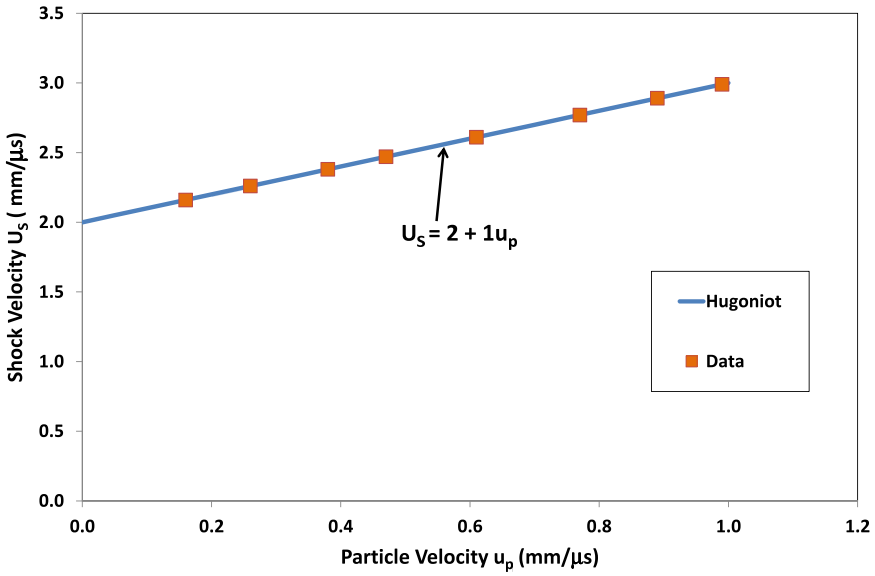

Figure 2.2: Generic Hugoniot in the U_S-u_p plane.

In the pressure-u_p plane, the hydrodynamic pressure P_H of a material is given by Equation 2.15, with Equation 2.16 used for the pressure-volume plane; where ρ_0 is the initial density and V and V_o being the volume at a given pressure and initial volume respectively. These equations come directly from the conservation of momentum (Equation 2.8) with P_0 taken as zero (*i.e.* going from a ground or unshocked state). The Hugoniot in the U_S-u_p plane is then used to calculate the value of P_H. Figure 2.3 shows the Hugoniot from Figure 2.2 translated into the pressure-volume plane, with a density of 2.8 g cm^{-3} assumed. However if a comparison is needed between multiple materials of differing densities, a unitless volume can be employed given by Equation 2.17 and as shown in Figure 2.4. This gives a ratio of the shocked (compressed) sample volume when compared to the initial volume and as such will always be less than 1.

$$P_H = \rho_0 U_S u_p \tag{2.15}$$

$$P_H = \rho_0 U_S^2 \left(1 - \frac{V}{V_0}\right) \tag{2.16}$$

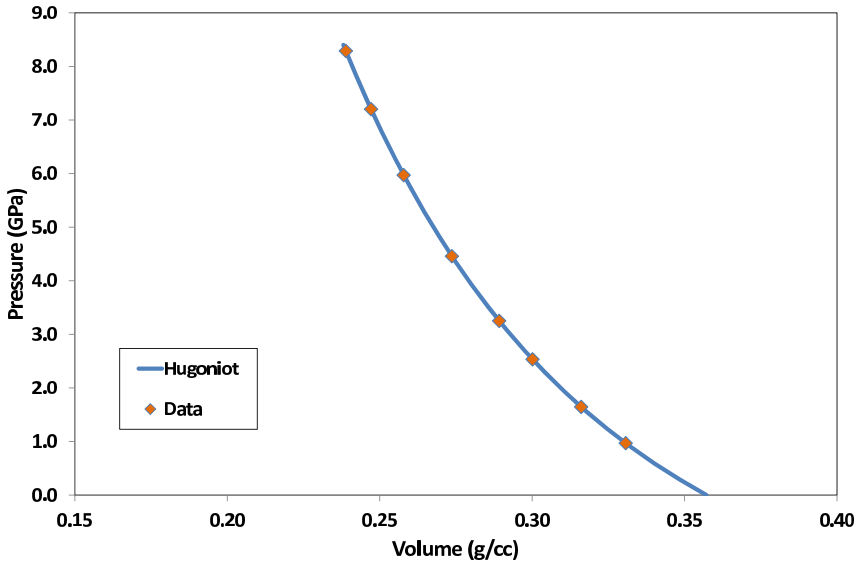

Figure 2.3: Generic Hugoniot in the pressure-volume plane.

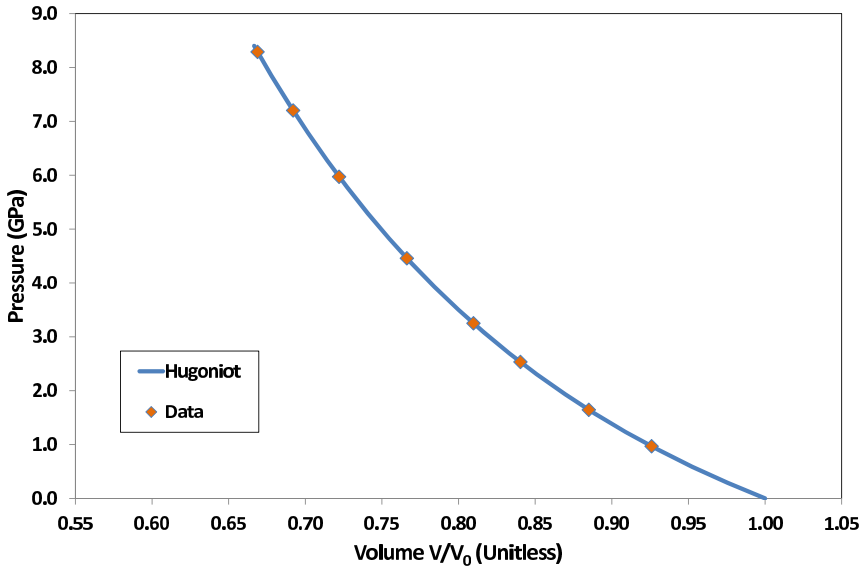

Figure 2.4: Generic Hugoniot in the pressure-unitless volume plane.

$$V_{Unitless} = \frac{Volume}{Initial\ Volume} \tag{2.17}$$

The value of u_p is found by using an impedance matching technique [22, Pages 110-114], which matches the shock state in the material of the flyer used to impart the

shock state to that of the sample material at a given impact velocity. The impedance matching technique is shown graphically in Figure 2.5. The impedance matching technique works by locating the intersect of the flyer plate material equation of state and that for the sample material being investigated for a given experimental setup. The conditions used for Figure 2.5 are a copper flyer impacting a phenolic resin Durite SC-1008 target at 800 m s^{-1}. The line for the flyer plate is inverted and offset by the impact velocity which in this case is 800 m s^{-1} (or 0.8 mm μs^{-1}). The sample material equation of state, used in this technique, is given by Equation 2.15. Using Figure 2.5 the pressure expected in the experiment may be directly read-off as 3.31 GPa, with a corresponding particle velocity value of 0.71 mm μs^{-1}. If a sample material is unknown as will often be the case, an analogous material is used for the impedance matching technique until the material is well defined. While it is possible, as shown in Figure 2.5, to solve such flyer plate impacts graphically, the impedance matching technique readily lends itself to solution via either the quadratic equation or as a least squares fitting approach. In this study the approach of least squared fit was used. The flyer plate materials used in this study were either aluminium or copper which are well defined in nature, *e.g.* Reference [29].

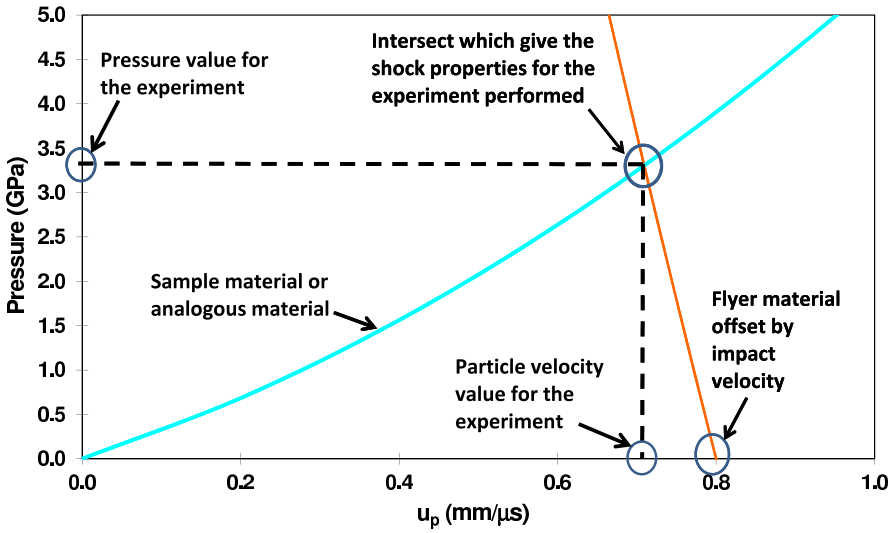

Figure 2.5: Graphical representation of the impedance matching technique.

Shock properties of the ground state depend on initial material properties such as density, along with initial elastic characteristics such as Young's modulus and Poisson's ratio. Such relevant elastic properties may be obtained using ultrasound equipment as explained in Section 3.4. For example the values of longitudinal (c_L) and shear (c_S) wave velocities can be obtained using ultrasonic measurement techniques. In addition, initial density can be easily measured using the appropriate equipment (for example a gas pycnometer explained in greater detail later in Section 3.3.1). From the sound speed measurements other elastic properties can be ascertained. These include bulk sound velocity c_B, impedance Z, shear modulus G, bulk modulus K and longitudinal modulus L. These values can then lead to Young's modulus and Poisson's ratio. The bulk sound velocity is a combination of c_L and c_S and for most materials has the approximate value of c_0, with c_B calculated using Equation 2.18.

$$c_B = \sqrt{c_L^2 - \frac{4}{3}c_S^2} \tag{2.18}$$

Another useful elastic property is the impedance (sometimes known as the acoustic impedance) of a material, which can be calculated using Equation 2.19. This property controls how materials interact while under shock loading especially when coupled together. For example a wave moving from a material of lower to higher impedance will be at least partially reflected as a compressive wave.

$$Z = \rho_0 c_B \tag{2.19}$$

The shear, bulk and longitudinal moduli can be calculated using Equations 2.20, 2.21 and 2.22 respectively. The bulk modulus is defined as the resistance of a material to a change in volume. Whereas the shear modulus is defined as the ratio of shear stress to shear strain, with such stresses arising when a force is applied at an angle. Finally, the longitudinal modulus represents the ratio of stress to strain when a force is applied longitudinally.

$$K = \rho_0 c_B^2 \tag{2.20}$$

$$G = \rho_0 c_S^2 \tag{2.21}$$

$$L = K + \frac{4}{3}G \tag{2.22}$$

To calculate Young's modulus Equation 2.23 is used. Young's modulus is a measure of the stiffness of the material, *e.g.* its resistance to applied force.

$$E = \frac{9KG}{3K+G} \tag{2.23}$$

Another useful elastic property which can be ascertained from the measured ultrasonic values is Poisson's ratio v. This is the ratio of lateral movement to sample compression when the material is compressed in one direction. The values tend to be between 0 and 0.5 where a value of v=0.5 corresponds to an incompressible medium (a fluid). Poisson's ratio is required when calculating the lateral stress under shock in a given material using lateral gauges [30]. Poisson's ratio is calculated using Equation 2.24.

$$v = \frac{3K-L}{3K+L} \tag{2.24}$$

For a material under plastic strain Equation 2.25 holds true [31], where Y is the yield strength of the material. This will only hold true if the yield criteria is Tresca or von Mises [32]. The Tresca yield criteria assumes that yielding will occur when the maximum shear strength is $0.5\sigma_{yield}$ as shown in Equation 2.26 [33, Page 52]. Whereas, the von Mises yield criteria states that the change in volume will lead to a distortion or shear [34, Pages 341-342], which leads to Equation 2.27 [33, Page 53-54]. Usefully both of these strength models can be applied to simulations of systems under shock in hydrocodes.

$$\sigma_x - \sigma_y = Y \tag{2.25}$$

$$\tau_{max} = \frac{1}{2}(\sigma_{max} - \sigma_{min}) = \frac{1}{2}\sigma_{yield} \tag{2.26}$$

$$\sigma_{yield}^2 = \left[(\sigma_x - \sigma_y)^2 + (\sigma_y - \sigma_z)^2 + (\sigma_z - \sigma_x)^2\right] \tag{2.27}$$

In homogenous materials $\sigma_y = \sigma_z$ which is also equal to σ_x if the material is behaving hydrodynamically (*e.g.*with little to no strength). Equation 2.28 relates mean, longitudinal and lateral stresses in a homogeneous three-dimensional system, which in turn leads to Equation 2.29 which can also be written as Equation 2.30.

$$\bar{\sigma} = \frac{1}{3}(\sigma_x + 2\sigma_y) \tag{2.28}$$

$$\sigma_x = \bar{\sigma} + \frac{2}{3}Y \tag{2.29}$$

$$\sigma_x = P_H + \frac{4}{3}\tau \tag{2.30}$$

Under dynamic loading the transition between elastic and plastic deformation is known as the Hugoniot elastic limit (HEL). Below the HEL materials behave elastically and above this point deformation is plastic in nature. One approach to determine the HEL involves measuring τ via Equation 2.26 and by noting any deviation from the elastic prediction given by Equation 2.31. This approach is shown in Figure 2.6 where the elastic and plastic data can be seen. By equating the equations for the elastic prediction (found using Equation 2.31 with a Poisson's ratio of 0.3 here) and the plastic data, the Hugoniot elastic limit can be calculated. In this case the HEL is 2.5 GPa.

$$2\tau = \frac{1-2\nu}{1-\nu}\sigma_x \tag{2.31}$$

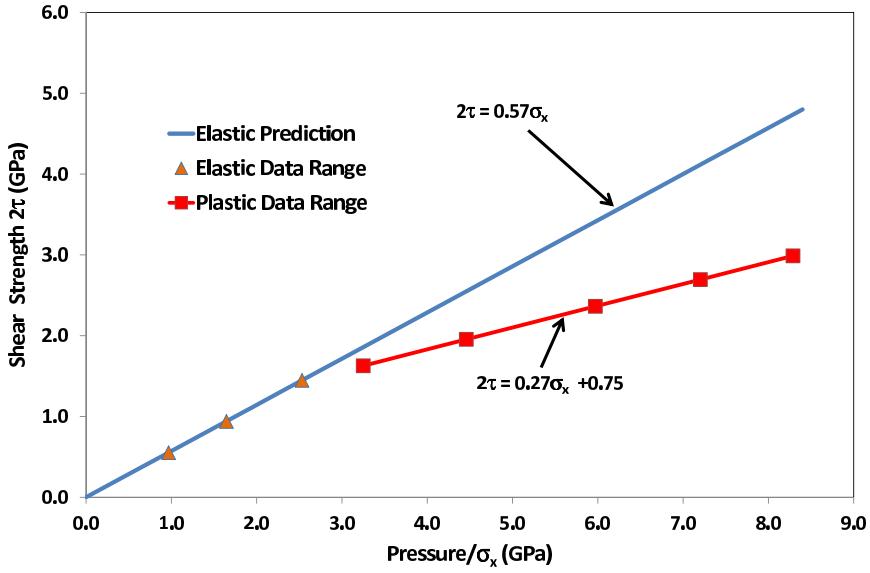

Figure 2.6: Generic figure for shear behaviour.

Hugoniot elastic limits also occasionally show up in shock traces; however in polymers the system tends to be overdriven, swamping this signal, necessitating alternative approaches to their derivation as discussed here.

2.2 Experimental Techniques

Many methods can be used for studying high rate deformation and shock response in materials. Field *et al.* [35] reviewed the experimental techniques used for high rate deformation and shock studies of materials. In terms of strain rate regime the methods reviewed are (from lowest strain rate to highest) dropweights, split Hopkinson pressure bar, Taylor impact and then shock loading. A dropweight uses gravity to accelerate a weight onto the sample material. With the split Hopkinson pressure bar (SHPB), a sample is placed between two bars and is deformed either by compression, torsion or tension. The sample is dynamically loaded by striking the input bar, or loading one of the bars

statically and then releasing it. A strain gauge is placed on each of the bars to monitor the input, reflected and transmitted signal. From these signals the dynamic behaviour of the material can be ascertained. Split Hopkinson pressure bars typically allow access to strain rates of up to 10^4 s^{-1}. Above the SHPB in terms of strain rate is the Taylor impact technique. This approach involves firing a cylinder of the sample into a large rigid target. This causes dynamic deformations at the impact face with a final shape that is dependent on the material properties. Due to this, material properties must be ascertained from macroscopic measurements of inhomogeneous deformation which is a disadvantage [36, Page 949]. In terms of the strain-rates of interest in this study, shock based loading is applicable.

2.2.1 Shock Wave Induction Methods

Multiple methods exists for inducing planar shock waves into targets. These include, but are not limited to; contact detonation of explosives, the plate impact technique and laser ablation [23, Page 4]. All of these methods can induce a one-dimensional shock into a given target material. A one-dimensional shock wave is desired due to its relative simplicity when compared to two and three-dimensional shock waves. This makes it possible to understand the effect the shock wave has on the target material to a greater extent, without the added complexity of geometric effects.

Plate Impact Technique

The plate impact technique accelerates a flat and parallel plate (known as a flyer plate) of material at a sample (which is also flat and parallel) to induce a shock wave into the target. The pressure generated in the sample is dependent on the material used and the velocity the sample is impacted at. Flyer plates can be accelerated using a variety of means, usually compressed gas or gun powder [23, Page 80]. Plate impact experiments are typically conducted using a gas gun of either single stage (as used in this project) or two stage variety. A more in-depth description of the plate impact technique is given in

Chapter 3.1.

Explosives

Explosives can be used in a variety of ways to induce a shock wave [37]. Explosives can be placed onto a sample to induce a shock wave directly in to the sample; this method is known as the contact explosives method. To ensure a 1D shock front an explosive lens can be employed. This allows uniform detonation of the main charge [23, Page 89]. To get to a higher pressure using explosives a flyer plate can be accelerated by the explosive. The flyer plate method is similar to the plate impact technique, except that a high explosive is used to accelerate the flyer plate. This leads to higher induced pressure than the contact explosives method [37, Page 11]. Figure 2.7 shows the mousetrap technique, with the figure edited from Reference [38, Pages 358-359]. The sheet explosive detonates accelerating the glass plate into the main charge. The angle between the glass plate and the main charge is orientated so that the glass impacts the main charge in a planar manner. This sets off the main charge launching the attached flyer plate downwards into the sample. Variations of this method can be implemented, to allow for different set ups/conditions.

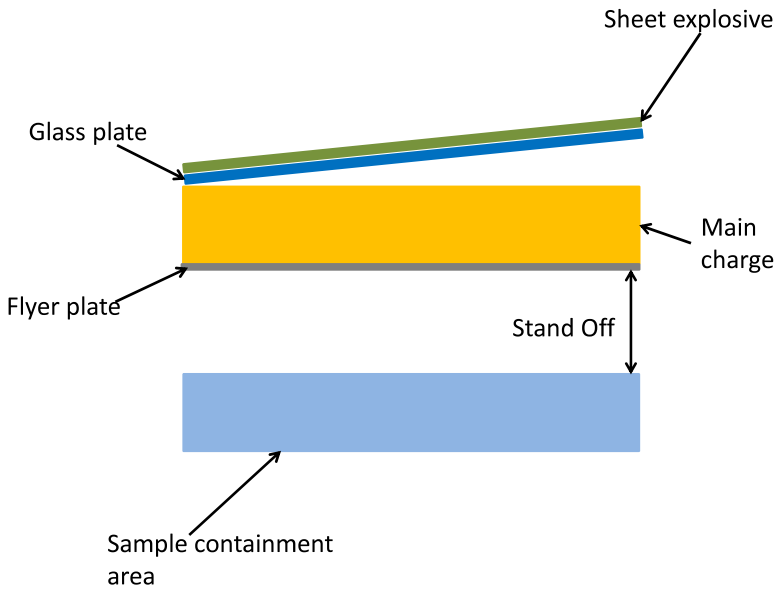

Figure 2.7: Diagram of the mousetrap technique.

Laser Ablation

Lasers can generate higher pressures than can be seen with plate impact or explosives [39]. By generating temperatures in the kilo-electron volt regime, surface ablation can lead to plasma formation and thermal pressures in the TPa range [40, Pages 319-320]. By using a pulse in the nanosecond range, the laser will heat a few microns of the surface of a target. Consequently by using a short duration high intensity laser pulse (*e.g.* pulse widths of less than a few nanoseconds and powers above 10^9 W cm^{-2}) a plasma can be generated on the surface of a sample. Rapid expansion of this plasma then drives a shock wave through the sample [41]. This can be done directly on to the sample or by confining it with a medium which is ablated which slows the expansion of plasma causing a higher pressure and pulse duration. Another method is to accelerate a flyer plate using laser ablation. Luo *et al.* explain this technique in Reference [42]. Typically at the laser facility used by Luo the laser spot size can vary between 50 μm and 50 mm. The usual spot size they used was between 1.5 and 5 mm. To launch a flyer plate the laser is focused on a multilayer through a transparent substrate. The multilayer target absorbs the laser

energy causing the generation of plasma leading to the acceleration of the flyer. Yang *et al.* [43] employed target elements of 900 μm^2 which were part of a larger target to perform multiple experiments in quick succession, generating pressures of up to 5 GPa.

2.3 Diagnostic Techniques

There are many diagnostic techniques in the field of shock physics including laser-based interferometric techniques such as VISAR and Het-V, stress gauges, flash X-ray and proton radiography. Each has its own positive and negative attributes.

2.3.1 Lasers

Lasers have a high temporal resolution making them an ideal choice for a diagnostic technique. Both VISAR (Velocity Interferometer System for Any Reflector) and Het-V (Heterodyne Velocimetry) use a laser to monitor the rear surface of a sample to ascertain the velocity the surface is travelling at. VISAR works by splitting the light into multiple beams (usually two) and ascertaining the frequency shift between the original laser beam and the reflected light from the sample [44]. Het-V works by combining two wavelengths, a reference wave and a different frequency wavelength. This leads to a beat frequency, which will be altered by the shock wave (when it reaches the surface the Het-V laser is focused on). This combination allows for a greater temporal resolution [44]. Each diagnostic has its own benefits, for example VISAR works at extreme velocities where as Het-V does not. However Het-V is a slightly more robust diagnostic technique and continues to work when the reflector comes apart whereas VISAR will cease to function. Another advantage is Het-V requires little to no alignment and is easy to use and build, using off the shelf telecommunications components.

2.3.2 Gauges

Gauges can be divided into many different types, *e.g.* electromagnetic gauges, piezoelectric gauges and piezoresistive gauges among others.

Particle velocity (PV) gauges are a type of electromagnetic gauges, which consist a series of wire elements typically embedded perpendicular to the impact axis in a target orientated at a defined angle within an applied magnetic field.The propagating shock picks up the embedded wire elements at the particle velocity, u_p; knowledge of gauge separation then allows for direct measurement of U_S. As the wire elements move this induces a current in the wires which leads to a value for u_p via Faraday's law of induction [45, Pages 58-59]. Due to this the gauges themselves do not need direct power.

Piezoelectric gauges generate a current while under stress, proportional to the loading. This is useful as no external power supply will be required. Some materials used for piezoelectric gauges are quartz, lithium niobate and a few polymers [22, Page 282].

Piezoresistive materials alter their resistance when a pressure is exerted onto them. Common materials used in these gauges are manganin, carbon and ytterbium [22, Page 280]. For the lower pressure regime carbon and ytterbium are more suited due to their linear resistance change. Carbon can be used up to 2 GPa, while ytterbium can be used up to 4 GPa. Manganin is better over a larger range of pressures and such gauges have been taken up to a pressure of 100 GPa [22, Pages 280]. Manganin is also useful due to the relative temperature insensitivity of its change in resistance under load [46]. Unlike electromagnetic and piezoelectric gauges, piezoresistive gauges do need a direct power supply. The power supply can only be activated a short time before the gauge is needed, as the gauges are by necessity thin and will burn out through resistive heating if the power supply is left on too long. Manganin gauges, such as the ones used in this project, directly measure σ_x, with U_S easily implied. The particle velocity u_p can then be found using the impedance matching technique outlined in Section 2.1. Typically experiments involve placing a gauge on both the front and rear of the sample and monitoring the resistance change across each gauge, which will provide a time dependent response as the shock

propagates. Knowledge of the shock arrival and the gauge separation gives the value of U_S; further details of this approach are given in Section 3.2.

2.4 Composites

A composite consists of a material made with two or more distinct components of differing qualities/properties [1, Pages 1-3]. These multiple components can lead to behaviour which is heterogenous (random configuration of components) or anisotropic (components ordered in particular directions) in nature. Some materials behave heterogeneously when viewed microscopically, but can be taken to be homogenous macroscopically, for example polymer bonded explosives [2, 47].

Composites cover a wide range of materials from natural to man made. Examples of natural composites are wood and bone. Man made composites include concrete and fibre based composites, with man made composites used in a variety of products including fishing rods, baseball bats and body armor. Composites tend to have two constituents with the continuous one referred to as the matrix material and the reinforcing material referred to as the reinforcing or reinforcement phase [1, Page 3-4]. With composites the addition the reinforcing phase is generally designed to improve the properties of the matrix material. In most applications the reinforcement tends to have a higher strength but is more brittle when compared to the matrix material, *e.g.* carbon fibres in a carbon fibre reinforced composite.

2.4.1 Elastic Properties of Composites

In light of their anisotropic nature, knowledge of stress-strain tensors is critical in composites systems. With anisotropic materials the direction in which a force is applied can greatly affect the material properties. This results in highly anisotropic stress and strain tensors which are based on a fourth order tensor following Equation 2.32, where C_{ijkl} is the elasticity tensor [48, Page 32]. However the stress and strain tenors are

Stress	Strain
$\sigma_{11} = \sigma_{xx} = \sigma_1$	$\varepsilon_{11}=\varepsilon_{xx} =\varepsilon_1$
$\sigma_{22} = \sigma_{yy} = \sigma_2$	$\varepsilon_{22}=\varepsilon_{yy} =\varepsilon_2$
$\sigma_{33} = \sigma_{zz} = \sigma_3$	$\varepsilon_{33}=\varepsilon_{zz} =\varepsilon_3$
$\sigma_{23} = \sigma_{yz} = \sigma_4$	$\varepsilon_{23}=\varepsilon_{yz} =\varepsilon_4$
$\sigma_{31} = \sigma_{zx} = \sigma_5$	$\varepsilon_{31}=\varepsilon_{zx} =\varepsilon_5$
$\sigma_{12} = \sigma_{xy} = \sigma_6$	$\varepsilon_{12}=\varepsilon_{xy} =\varepsilon_6$

Table 2.1: Shorthand notation used for the stress and strain tensors.

symmetric meaning $\sigma_{ij} = \sigma_{ji}$ and $\varepsilon_{kl} = \varepsilon_{lk}$. The elasticity tensor is shown in Equation 2.33, however by using Voigt's contracted notation, this can be reduced as shown in Table 2.1 [49, 50], with the reduced elasticity tensor shown in Equation 2.34.

$$\sigma_{ij} = C_{ijkl}\varepsilon_{kl} \tag{2.32}$$

$$C_{ijkl} = \begin{bmatrix} C_{1111} & C_{1122} & C_{1133} & 0 & 0 & 0 \\ C_{1122} & C_{2222} & C_{2233} & 0 & 0 & 0 \\ C_{1133} & C_{2233} & C_{3333} & 0 & 0 & 0 \\ 0 & 0 & 0 & C_{2323} & 0 & 0 \\ 0 & 0 & 0 & 0 & C_{1313} & 0 \\ 0 & 0 & 0 & 0 & 0 & C_{1212} \end{bmatrix} \tag{2.33}$$

$$C_{ij} = \begin{bmatrix} C_{11} & C_{12} & C_{13} & 0 & 0 & 0 \\ C_{21} & C_{22} & C_{23} & 0 & 0 & 0 \\ C_{31} & C_{32} & C_{33} & 0 & 0 & 0 \\ 0 & 0 & 0 & C_{44} & 0 & 0 \\ 0 & 0 & 0 & 0 & C_{55} & 0 \\ 0 & 0 & 0 & 0 & 0 & C_{66} \end{bmatrix} = \frac{1}{\Delta} \begin{bmatrix} \frac{1-\nu_{23}\nu_{32}}{E_2E_3} & \frac{\nu_{21}+\nu_{23}\nu_{31}}{E_2E_3} & \frac{\nu_{31}+\nu_{21}\nu_{32}}{E_2E_3} & 0 & 0 & 0 \\ \frac{\nu_{12}+\nu_{32}\nu_{13}}{E_1E_3} & \frac{1-\nu_{13}\nu_{31}}{E_1E_3} & \frac{\nu_{32}+\nu_{12}\nu_{31}}{E_1E_3} & 0 & 0 & 0 \\ \frac{\nu_{13}+\nu_{12}\nu_{23}}{E_1E_2} & \frac{\nu_{23}+\nu_{13}\nu_{21}}{E_1E_2} & \frac{1-\nu_{12}\nu_{21}}{E_1E_2} & 0 & 0 & 0 \\ 0 & 0 & 0 & G_{23}\Delta & 0 & 0 \\ 0 & 0 & 0 & 0 & G_{31}\Delta & 0 \\ 0 & 0 & 0 & 0 & 0 & G_{12}\Delta \end{bmatrix} \tag{2.34}$$

Where Δ = (1-$\nu_{12}\nu_{21}$-$\nu_{23}\nu_{32}$-$\nu_{31}\nu_{13}$-2$\nu_{21}\nu_{32}\nu_{13}$)/($E_1E_2E_3$), ν_{ij} is Poisson's ratio and

G_{ij} is shear modulus.

For the stain relationship with orthotropic materials Equation 2.35 can be employed. The Voigt notation compliance tensor (B_{ijkl}) is shown in Equation 2.36.

$$\varepsilon_{ij} = C^{-1}_{ijkl}\sigma_{kl} = B_{ijkl}\sigma_{kl} \tag{2.35}$$

$$B_{ij} = \begin{bmatrix} B_{11} & B_{12} & B_{13} & 0 & 0 & 0 \\ B_{21} & B_{22} & B_{23} & 0 & 0 & 0 \\ B_{31} & B_{32} & B_{33} & 0 & 0 & 0 \\ 0 & 0 & 0 & B_{44} & 0 & 0 \\ 0 & 0 & 0 & 0 & B_{55} & 0 \\ 0 & 0 & 0 & 0 & 0 & B_{66} \end{bmatrix} = \begin{bmatrix} \frac{1}{E_1} & -\frac{\nu_{21}}{E_2} & -\frac{\nu_{31}}{E_3} & 0 & 0 & 0 \\ -\frac{\nu_{12}}{E_1} & \frac{1}{E_2} & -\frac{\nu_{32}}{E_3} & 0 & 0 & 0 \\ -\frac{\nu_{13}}{E_1} & -\frac{\nu_{23}}{E_2} & \frac{1}{E_3} & 0 & 0 & 0 \\ 0 & 0 & 0 & \frac{1}{G_{23}} & 0 & 0 \\ 0 & 0 & 0 & 0 & \frac{1}{G_{31}} & 0 \\ 0 & 0 & 0 & 0 & 0 & \frac{1}{G_{12}} \end{bmatrix} \tag{2.36}$$

All of these properties can be changed depending on the ratio of fibres to matrix. This can be expressed as a volume fraction (V) or weight fraction (W), as shown in Equations 2.37 and 2.38 where the subscript α refers to either the fibre or matrix and c refers to the composite as a whole.

$$V_\alpha = \frac{v_\alpha}{v_c} \tag{2.37}$$

$$W_\alpha = \frac{w_\alpha}{w_c} \tag{2.38}$$

The distribution of stresses in such systems is a function of the volume fractions. As such if an external stress (σ_A) is applied Equation 2.39 is used where f is the volume fraction of the reinforcement (fibres), and where $\bar{\sigma}_m$ and $\bar{\sigma}_f$ are the stress in the matrix and fibre respectively [51, Page 7].

$$\sigma_A = f\bar{\sigma}_m + (1-f)\bar{\sigma}_f \tag{2.39}$$

This approach is known as the rule of mixtures and is a common way of assessing the properties of a composite. If the constituents are known then the final properties of the composite can calculated to a reasonable accuracy [52, Pages 81-83].

2.4.2 High Strain Rate Behaviour of Composites

Richardson and Wisheart [53] provided a concise review of composite response in the low impact regime (below 10 m s^{-1}). Due to the brittle nature of most composites they can only absorb deformation elastically and through damage mechanisms. They identified four main modes of failure, which were matrix cracking, delamination, fibre failure and penetration. Matrix damage is the first type of failure associated with transverse low velocity impact, and takes the form of cracking. This cracking occurs due to the differing properties of the fibre and matrix. Delamination is a crack that runs along the resin interlayers. Liu [54] explained that delamination was caused by a mismatch between adjacent fibre layers, due to the differing fibre orientations. Fibre failure happens due to localised concentration of stress and in particular high bending stresses. Fibre failure is a precursor to penetration damage. Penetration is a macroscopic mode of failure occurring when the fibres fail, which allows the impactor to pass through the sample. Next in the review Richardson and Wisheart looked at the role of constituents and the interface between them. Fibres provide the composite with most of its strength, with carbon having the highest strength and stiffness values, but having the disadvantage of being the most brittle element of the system. The matrix transfers the load to the fibres, both protecting the fibres from damage as well as aligning and stabalising the fibres. The interface between the fibres and matrix is extremely important. To help the matrix bond to the carbon fibres, the fibres are treated with an oxidant, which improves the cohesion between the fibres and matrix. While this low impact response is outside of the range investigated here, some of these issues will also occur while under shock loading.

The response of the composite in the low impact regime was further investigated by David-West *et al.* [55] who examined the energy absorption and bending stiffness of a

carbon fibre reinforced polymer laminate with ply orientations of $[0/90]_{6s}$ and $[0/45/90]_{4s}$. This was achieved by using a 30 kg impactor falling from a height of 0.04 m under gravity, which imparted an impact energy of 12 J, with these conditions consistent throughout the experiments. The resultant force-displacement and force-time graphs showed the same force magnitude between the different ply orientations. Differences in the stress waves were noticed between the ply orientations. Sectioning the impacted samples more damage was seen on the $[0/45/90]_{4s}$ ply orientations than in the $[0/90]_{6s}$ case; this was thought to be due to the inclusion of the 45° laminae. However the $[0/45/90]_{4s}$ material was more resistant to bending than the $[0/90]_{6s}$ laminate.

Increasing the impact regime Griffiths and Martin used a split Hopkinson pressure bar to investigate the dynamic behaviour of a carbon fibre composite [56]. To induce a pulse into the composite a rifle round was fired into the input bar. This imparted a 200 Nm^{-2} peak stress with a 35-40 μs pulse. Different volume fractions and orientations were investigated. It was found that the initial modulus increased with volume fraction. The secondary modulus was an order of magnitude lower than the initial modulus, and remained constant with volume fraction.

At higher strain-rates still, in the shock regime Millett *et al.* [3] investigated a simple isotropic composite. This composite was a epoxy resin filled with alumina particles with average particle size of 0.5 μm. Two versions of this composite were investigated, namely half nominally and fully loaded arrangements (exact percentages were not given in the paper). Tests were conducted using the plate impact technique in the velocity range of 190-670 m s^{-1}, with manganin gauges used to monitor shock transit and evolution. It was found that under the same impact conditions the stress in the fully loaded sample was much greater than that in the half loaded sample. This was also greater than what would be seen in the epoxy resin alone. This was not an unexpected result as the increased ratio of alumina particles led to a higher density in the investigated sample. These results also led to different Hugoniots in the U_S-u_p plane, with that for the fully loaded composite offset by a consistent amount from the half loaded sample response. However both samples,

like the epoxy resin, possessed linear equations of state in the regime investigated. This contrasts with other work where non-linear behaviour has been observed in multiple polymers like PMMA, PRR and phenolic resina [26, 27, 28]. Ultrasonic measurements showed that as the percentage of alumina particles increased the sample behaved more like a metal. It should be noted however that only 4 experiments were performed on each type of composite leading to reactively large potential errors; this may explain why any underlying non-linear behaviour was not observed.

Dyneema® is an interesting composite. The reinforcement and matrix are made of the same material, polyethylene, with the reinforcement provided by polyethylene spun into fibres. While initially the properties of polyethylene are the same, when the fibres are produced they have different properties to the matrix. In a short conference contribution Chapman *et al.* [57] investigated the shock response of Dyneema® via a series of plate impact experiments. In addition to standard Hugoniot experiments, off-Hugoniot data was obtained using shock reverberation techniques. The off-Hugoniot data fell below the principle Hugoniot.

A more indepth investigation into the shock propagation of Dyneema® was carried out by Hazell *et al.* [58]. In this investigation the fibres were orientated parallel to the direction of travel. Due to this orientation the observed c_L value was higher as the fibres acted as wave guides. An elastic precursor was noted in most of the recorded gauge traces, which remained constant in terms of velocity, with a velocity at the elastic sound speed, c_L. This is similar to the precursors seen in a glass fibre composite investigated by Millett *et al.* [14], carbon fibre composites investigated by Millet *et al.* [16] and Hazell *et al.* [17] and an aramid fibre composite investigated by Bordzilovsky *et al.* [20]; although it should be noted that while the orientations associated with the Bordzilovsky *et al.* study do not match this Dyneema® study, the principle is comparable in nature. A non-linear Hugoniot was found which is unsurprising due to the polymer constituents of Dyneema®, which matched well with the one obtained by Chapman *et al.* [57]. It was also found that at higher u_p values, the fibre reinforcement disappeared. This disappearance of fibres was

attributed to shock melting of the fibres, with the melting temperature occurring between 144 and 152°C. The corresponding value of u_p (*ca.* 0.78 mm μs^{-1}) also coincided with the disappearance of the elastic precursor.

Holmes and Tsou [59] investigated an aluminum unidirectional fibre composite set in an epoxy resin, at different fibre fractions. The aluminum fibres were 3.18 mm in diameter, with the fibre densities being 25, 40 and 60%. This composite is similar in nature to the one studied by Millett *et al.* in Reference [3], due to the use of epoxy resin as a matrix material; except instead of ceramic particulates investigated by Millett *et al.*, Holmes and Tsou used metallic fibres. The system was shock loaded by using explosives with a plane wave lens to ensure one-dimensionality of the resultant shock wave. By using two target thicknesses (9.53 and 25.4 mm) it was possible to evaluate whether the shock wave was steady in nature. Both the shock velocities were comparable for the different thicknesses meaning the shock wave was steady. The authors found good agrement with the experimental results and the expected results (calculated using an adiabatic model) with any offset lying within the experimental error.

In a short communication, Tsai *et al.* investigated the effect that a shock wave had on a glass fibre composite [11]. The glass fibre composite investigated was a S2 woven glass fibre in a polyester matrix. Using a single stage gas gun along with polyvinylidene fluoride (PVDF) gauges spaced apart by varying amounts, the shock profile was observed at different thicknesses. As the thickness increased the peak pressure recorded by the gauge reduced, with the rise time increasing. This is a demonstration of the attenuation that can effect the shock wave in such composite samples. A VISAR system was also used to investigate the shock wave profile in four different thicknesses of targets. These thicknesses were 2.94, 6.88, 12.37 and 20.2 mm. Interestingly no decrease in pressure was noted but the rise times did become slightly slower; these results were mirrored when Dandekar *et al.* investigated the same composite [12]. The previously observed decrease in pressure may be due to the arrangement of PVDF gauges in the first experiment (three gauges in one target) where the interlayers may be partially causing the attenuation seen.

Further, the thin flyer plate used would also have meant that release waves from the flyer plate would have caught up and interacted with the main shock front relatively rapidly. This behaviour shows the importance of keeping the experimental set up simple and assessing the geometries associated with sample size as well as the flyer plate.

Oved *et al.* [60] investigated a layered composite structure of copper and PMMA using both experiments and computational models. Using a powder gas gun and manganin gauges they investigated the shock response of this layered composite. Each boundary was orientated parallel to the shock front. The number of layers, along with the thickness of each layer in the composite was varied for different tests. The experiments led to a complex wave interaction causing oscillations in the shock profile, linked to the periodic nature of the composite layers. The main purpose of these experiments was to test the computational model, which was found to be able to simulate this complex shock profile. The main difference between the simulation and the model was the fact that in one otherwise identical model and experiment set, a difference in stress was seen. By altering the pressure equation in the computational model this discrepancy was greatly reduced leading to closer agreement between the computer model and experimental results in all cases. Consequently from this the authors were able to use the model to gain a greater insight into the shock interaction of the layered composite.

Further work on multilayered composites was performed by Zhuang *et al.* [61]. Zhuang *et al.* investigated multiple layered composites using a powder gun to accelerate a sabot to between 400 and 2000 m s^{-1} to achieve stresses of up to 10 GPa. To monitor the shock profile, both manganin gauges and VISAR were used. The composites were polycarbonate with aluminium, steel or glass, with the thicknesses being 0.37 or 0.74 mm for the polycarbonate, 0.2 or 0.55 mm for the glass, 0.37 mm for the aluminium and 0.19 or 0.37 mm for the steel. They found that a periodic layered structure can support a steady shock wave, with the rise time decreasing as the impact velocity was increased. They also found that a greater impedance mismatch between the constituents led to a larger dispersion of the shock wave.

Dandekar *et al.* [12] investigated the shock response of a glass fibre composite using a gas gun along with VISAR to investigate the shock profile. The glass fibre composite was also investigated by Tsai *et al.* [11]. The shock stresses reached in these experiments were between 4 and 20 GPa. The glass fibres were woven with a polyester resin matrix with the volume fraction of the fibres being 68%. Using shock reverberation experiments the Hugoniot elastic limit was found to be between 1.3 and 3.1 GPa, with the most likely value being 1.3 GPa; however the authors concluded that more experiments were needed to narrow this value down. Interestingly they found that the shock response lay between the shock Hugoniot's of glass and the matrix material. This was in agrement with the rule of mixtures approach discussed earlier in this chapter.

The effect on fibre weave orientation was investigated by Millett *et al.* using the plate impact technique on a glass fibre epoxy composite [14]. The investigated properties were fibre orientation and sample thickness (either 3.8 or 9.8 mm). The fibre weave orientation investigated was through fibre, with the fibre parallel to the direction of travel. The sample thickness had no effect on the rise time seen by the manganin gauges, contrary to the effect seen by Tsai *et al.* [11] and Dandekar *et al.* [12]. Differences were noted however in the release seen in the sample, with the thicker sample experiencing spallation whereas the thinner sample did not, demonstrating the importance of duration for spall to occur. For the through thickness orientation a linear Hugoniot was obtained, which matched up well with the data gathered from Dandekar *et al.* [12] on a similar glass composite. When the composite was shocked in the fibre direction, the low velocity experimental traces had a ramped nature. At higher velocities the experiments showed a precursor as has been seen in other composite materials, such as Dyneema® [58], and carbon fibre composites [16, 17] when subjected to shock in the same fibre orientation.

In similar work again looking at the effect of weave orientation on shock response, Millett *et al.* used the plate impact technique [16] on a carbon fibre epoxy composite. The orientations investigated were 0° and 90° with the notation here referring to the orientation between the weave and direction of travel, opposite to the notion used in this thesis.

The 90° orientation was also referred to as the through fibre axis. The velocity range investigated was between 200 and 1125 m s^{-1} leading to a maximum stress of about 7 GPa. A PMMA offset was used for extra protection for the rear gauge to allow for a longer rear gauge trace; *e.g.* the rear gauge was encapsulated by *ca.* 1.5 mm PMMA and the main PMMA backing. Oscillations were seen at the top of the front gauge and were attributed to the shock wave interaction between the fibre and matrix material. The gauge traces for the 90° lay up behaved as if the sample was a monolithic material. In the 0° orientation a ramped region was observed in some of the higher velocities traces as seen in other materials [17, 58], before a rapid rise time as seen with most materials. The start of this ramp at the foot of the trace corresponded to a U_S value of about 7 mm μs^{-1}. It was proposed that this corresponded to an elastic wave propagating down the fibres. Both the Hugoniots in the U_S-u_p planes were found to be linear in nature. Furthermore, it was demonstrated that the Hugoniots were different for each orientation at lower pressures before subsequently converging at the higher end. This was an interesting result, suggesting that under shock loading, composite systems have a point at which orientation becomes unimportant, which has been observed by others [18].

Hazell *et al.* investigated the effect of thickness on the shock response of a carbon fibre composite [17]. For this study the fibres were orientated to be perpendicular to the shock front, and impacted using a single stage gas gun between 643 and 826 m s^{-1}. For protection of the rear gauge a PMMA offset was used in the same manner as used by Millett *et al.* in Reference [16]. The thicknesses of CFRP used were 1.52, 3.00, 6.05 and 9.06 mm. Along with the investigation into thickness effect a standard U_S-u_p Hugoniot was obtained. It was found that as thickness increased the ramped portion of the gauge trace became more pronounced, which resulted in a slower rise time, however the shock wave was steady. If this behaviour is applicable to all carbon fibre composites then thicker targets can be used which are easier to employ, though the downside is a slower rise time. The authors attributed the ramped portion to a elastic high velocity wave which being transmitted along the fibres before the “main shock”. These effects was also seen in the

glass fibre composite investigated by Tsai *et al.* [11] as well as a similar carbon fibre composite investigated by Millett *et al.* [16]. Further, it matches with the behaviour seen in the highly aligned Dyneema® by Hazell *et al.* [58]. However, the ramped portion in the glass fibre composite investigated by Tsai *et al.* [11] was less extreme than the one seen in this work however, and that in the study carried out by Millett *et al.* [16]. This suggests that the constituents of the composite (where fibre orientation is comparable) are important, leading to a potential difference in the shock profile.

Further work focused on investigating the effect that the angle of the weave has on the shock wave was carried out by Bordzilovsky *et al.* [20]. The composite investigated was a aramid fibre with an epoxy resin matrix. They conducted experiments involving the same shot with the only difference being the angle of the fibre weave. The angles investigated were 5°, 15°, 45° and 90°, where the angle is measured against the direction the shock wave is travelling. They used manganin gauges to record the stress profile of the composite and used TNT to accelerate the copper flyer plate into the target. With the angle set at 5° and 15° they saw an elastic precursor travelling at a velocity of approximately 6 mm μs^{-1}. This precursor was smeared in to a plastic precursor at an angle of 45°. Finally this precursor disappeared at 90° leading to the usual rapid rise associated with manganin gauges. The stress of the composite was greatest at 5° before dropping off until it increased again at 90°. However whether this behaviour continues at other velocities is unknown due to only one velocity being investigated. Hugoniot elastic limits were found from the precursor waves in the shock profiles. At an angle of 5° the HEL was 0.2 GPa, at 15° 0.15 GPa and at 45° the HEL was 0.5 GPa. This change in the HEL would be expected for the TWCP samples that were investigated here for the orientations of 25° and 45°, with the HEL for the 25° material here expected to have the lowest HEL of all the orientations.

The matrix material can have an effect on the shock propagation of a composite. Zaretsky *et al.* [15] studied the shock response of a glass fibre composite. The authors used plate impact experiments in the velocity regime of 60 to 300 m s^{-1} along with

VISAR to investigate the shock profile. Both the epoxy resin used as a matrix material along with the glass fibre composite were investigated. It was found that at low velocity impacts the behaviour of the composite was dominated by the glass epoxy resin matrix. By increasing the velocity the shock interactions between the interlayers became more important. They also found that the spall strength measured in the composite was lower than that measured in the epoxy resin alone, suggesting that at lower pressures the matrix dominates, due to matrix cracking being the first failure mode (possibly leading to delamination) as was discussed by Richardson and Wisheart [53]. This gives further justification for the study on the shock response of the matrix material of the TWCP, namely the phenolic resin Durite SC-1008.

Multiple diagnostic techniques were used by Willows *et al.* to investigate the shock response of a carbon fibre composite using the plate impact technique [18]. Using VISAR and manganin stress gauges the shock profile of both ring up and ring down experiments were found. They also concluded, with the help of a computational model that fibre orientation is unimportant above a u_p value of 1000 m s^{-1}, backing the results seen by Millett *et al.* [16] for their carbon fibre composite.

Dandekar *et al.* investigated both the elastic parameters and the delamination strength in a glass fibre reinforced composite [13]. The composite was a glass fibre weave with a polyester matrix material with the weight fraction of the matrix being about 32%. Ultrasonic transducers were used to measure the elastic constants. By using longitudinal and shear wave velocities the nine elastic constants could be ascertained. To measure the delamination strength a single stage gas gun was used with VISAR to view the propagation of the shock wave. These experiments were performed in the elastic range of the composite along with altering the angle of the impactor and sample which would lead to extra induced shear strain. It was found that delamination would only occur above a value of 0.07 GPa and by altering the angle of the impact, the delamination strength could be decreased, due to the extra induced shear strain resulting from the angle. The decrease seen here is comparable in nature to the decrease in the HEL seen by Bordzilovsky *et al.*

[20].

At the highest strain rate, Wicklein *et al.* [62] tested a hypervelocity model of CFRP, with aluminium honeycomb support, while comparing it to experimental results. ANSYS Autodyn® was the model used, with the CFRP material data obtained from the literature. The CFRP was modeled as a homogenous orthotropic material not a laminate. The elastic-plastic behaviour was defined by multiple equations with the parameters found from material testing. The experiments performed for model validation were plate impact experiments and hypervelocity experiments. The planar plate impact tests investigated spallation, inverse impact and multishock behaviour between velocities of 170-1070 m s^{-1}. The hypervelocity experiments were performed with ball bearings with diameters between 0.8-4 mm at angles of incident up to 60° between velocities of 3 and 6.5 km s^{-1}. It was found that the computational model gave good agreement with the experimental results.

Computation Modeling of Composites

As outlined previously, some of the authors whose work has been described have used experiments to validate the computational models. Other authors use data from the literature as a basis of their model validation approach. This has advantages as some features may not be present in some materials (*i.e.* the ramped nature seen in carbon fibre composites that was not present in the majority of glass fibre composites), but disadvantages as not all of the traces will be given in a study, leading to a requirement to make assumptions and generalisations on the authors part.

Due to the anisotropic nature of composite materials creating computational models can be problematic. This means that for these models, experiments have to be used for validation. One set of experiments that have been used for validation of computational model were performed by Millett *et al.* [16]. These experiments have been used to validate either in part or full the following models by Vignjevic *et al.* [63, 49] and Lukyanov [64].

Vignjevic *et al.* in a short conference proceeding modeled a composite using DYNA3D [63]. Two approaches for the modeling of the composite were used. The two approaches relate to separate decomposition tensors. The first decomposition tensor is the stress tensor due to strain. The second decomposition tensor is based on the deviatoric stress tensor. The first decomposition tensor (decomposition 1) agreed better with the experimental results for both the front and rear gauges, than the second decomposition tensor (decomposition 2).

A more in-depth study by Vignjevic *et al.* followed on from Reference [63], to model shock waves in orthotropic elastic materials [49]. As before two decomposition tensors were used which while again being compared to experiments were also compared to a constitutive model by Anderson *et al.* [65]. The stress decomposition tensors involved in Reference [63] were updated and coupled to the EOS. The model was tested for both the through thickness (fibres parallel to the shock front) and longitudinal (fibres perpendicular to the shock front) direction. For the through thickness model decomposition 1 shows good agreement between the model and experiments for both gauges. Decomposition 2 overestimates the stress experienced by the composite. The model employing the technique of Anderson *et al.* also overestimated the stress in the composite. For the longitudinal orientation only decomposition 1 was used due to the good agreement given in the through thickness direction; with only the rear gauge being modeled due to the experimental results. Good agreement was seen between the model and experiments. Differences, however were noted on the rise of the traces for both the model and experiment, where the model showed no precursor as was seen on the experimental traces. This highlights the subtleties of composites that can be lost in the model, where the system has to be simplified to create said model.

Lukyanov [64] used an anisotropic equation of state to investigate the shock behaviour of a carbon fibre composite. The data used for validation of the model was the carbon fibre composite investigated by Millett *et al.* [16]. Using a decomposition tensor similar to the one used by Vignjevic *et al.* [63, 49] the anisotropic equation of state was built up. It

is noted that if the shock velocity decreases as pressure increases then the shock front would break into two or more waves, or at the very least a smeared shock front. This decrease was noted with the 0° material (shock front perpendicular to the fibre direction) in Reference [16]. Due to this behaviour, it was expected that a two wave structure would be required to describe this experimental data. This behaviour was not seen in the through fibre orientation, and as such a linear Hugoniot could be fitted through the data. As the shock velocity was increased convergence was noted between the two orientations (the 0° and through thickness directions). By using the two-wave structure the low and high pressure regime gave good agreement between the model and experimental data.

Phenolic Resin Based Composites

As discussed above there is a substantial amount of work looking at the shock response of composites. Less work has been carried out on phenolic resin based composite systems of interest here. In one such study Burrell *et al.* [19] used a single stage gas gun to induce u_p values into a TWCP sample of between 0.2 and 0.9 mm μs^{-1}, with the shock profile measured using manganin stress gauges. The carbon fibre weave was at a 20° angle to the impact face. As mentioned previously, the reason for the 20° orientation was that this angle provides the best compromise between ablation response and strength. The data was compared to previous data for TWCP [66] and also, other data sets for the shock response of similar material at different angles (angles of 0° and 90°) investigated by Millett *et al.* [16]. They found that the Hugoniot equation the U_S-u_p plane with the form shown in Equation 2.13 was $U_S = 3.74 + 0.57u_p$. This held good agrement with the old data with the same weave angle. This result was compared to the data gathered by Millett *et al.* [16], where they investigated the effect of fibre orientation on the shock response of a carbon fibre composite, and concluded that when the fibre weave was parallel to the shock front the composite behaved as if it was a monolithic material; whereas the other orientation (fibres orientated perpendicular to the shock front) displayed complex behaviour. It was found by comparing the different carbon fire composites in the U_S-u_p

plane that the TWCP had a slightly higher gradient, suggesting that the TWCP is less compressive when compared to the carbon fibre composite investigated by Millett *et al.* [16]. This would likely be due to a transference of force over a larger area. Also no elastic precursor was seen, whereas such phenomena have been seen in multiple carbon fibre composites by Millett *et al.* [16] and Hazell *et al.* [17], as well as an aramid fibre composite investigated by Bordzilovsky *et al.* [20]. Bordzilovsky *et al.* found that shocks propagating through lay ups with lower angles had less of a precursor which may explain why no elastic precursor is seen here.

2.4.3 Summary of Composites at High Strain Rate

In summary anisotropic materials can have complex shock wave interactions dependent on the direction the force is applied. This can lead to elastic precursors if the shock front is perpendicular to the fibres as seen by Millett *et al.* [14, 16], Hazell *et al.* [17] and Bordzilovsky *et al.* [20]. As Bordzilovsky *et al.* also showed, the smaller the angle of the fibres compared to the shock front the weaker the elastic precursor becomes until it is not seen. Millett *et al.* [16] showed that if the fibre weave is orientated parallel to the shock front then the material will behave monolithically. It would also be expected that the thicker the composite sample the longer the rise time will become as seen by Hazell *et al.* [17] and Tsai *et al.* [11]. The complex wave interactions also led to the potential for oscillations to be seen due to the layered structure of the composite, *e.g.* as observed by Oved *et al.* [60] and Millett *et al.* [16]. Zaretsky *et al.* [15] found that at lower stresses the polymer matrix dominated the shock behaviour of the material, which was mirrored by the review performed by Richardson and Wisheart [53]. By increasing the stresses induced in the composites the interactions between the fibres and matrix material become more important.

2.5 Polymers and Other Materials

As shown by Zaretsky [15] the matrix material can affect the shock properties of the composite; due to this it is important to understand how polymers behave while under shock loading. Shock interaction with polymers is also important for other reasons due to their use as a binder for explosives [2, 47] among other applications. Polymers are also used in other aspects of high strain rate research for example PMMA is used as a backing material for shock experiments and also as a window material for laser based diagnostics [67]. Due to this it is becoming important to understand the shock response of as many polymers as possible, however due to the shear number of polymers available this is difficult to accomplish. This therefore leads to polymers that are well defined *e.g.* polymethylmethacrylate (PMMA) [26, 28], and to materials that are undefined or with limited data available.

Barker and Hollenbach investigated three materials that are used as window materials for interferometry [26]. These materials were PMMA, fused silica and sapphire. As fused silica and sapphire are not used here, these materials will not be discussed in excessive detail. To investigate these materials a gas gun (the type is not given in this paper) was used to induce a shock wave into the requisite sample. The sample and the window were comprised of the same material, in order to reduce the reflection that would be caused by any interlayers. To investigate the shock response a VISAR system was used. PMMA had been investigated multiple times before but a scatter was present in the data meaning it could not be used usefully as a window material. It was believed that this scatter was caused by manufacturing techniques, and to alleviate this issue a particular brand of PMMA was used. It was envisaged that while this would not help get rid of the scatter in the literature, that it would provide reproducible results with limited scatter. A non-linear equation of state was found in the U_S-u_p plane with no equation given (one can be found from the data). With respect to the data from the literature some of the data agreed with the new results while most of the data did not. It was also seen in a stress-strain curve that the elastic-plastic transition occurred at 0.7 to 0.8 GPa.

Carter and Marsh [28] studied 20 polymers and commented upon their general behaviour. One detail they found common to their collected polymer data was a discrepancy between the U_S-u_p curve and the ultrasound measurements taken at zero pressure, primarily seen as a difference between the values of c_0 and c_B. This was thought to be due to the forces between adjacent polymer chains being orders of magnitude lower than the forces along the backbone of the polymer, meaning the initial compression was 2D in nature before becoming 3D for the linear part of the Hugoniot. It was also found that a phase change occurred in the polymers investigated in the 20-30 GPa range and this was thought to be due to new bonds being formed after the carbon-carbon covalent bonds were broken. One of the polymers investigated was a phenolic resin Durite HR 300-Borden. The Hugoniot in the U_S-u_p plane was found to be $U_S = 2.98 + 1.39u_p$ between the u_p range of 0.6 and 2.6 mm μs^{-1}.

In another useful study, Millett and Bourne [68] investigated the shock response of three simple polymers whose only difference was the addition of a more complex side group. These polymers were polyethylene, polypropylene and polystyrene. The densities of these three polymers are comparable in nature with values between 0.90 and 1.03 g cm^{-3}. They found a linear U_S-u_p relationship in each case over the investigated range. While the values of c_0 and S were different the relationships in the σ_x-u_p plane were similar over the investigated range.

In comparable work, Munson and May [69] investigated the epoxy resin Epon 828 with three different hardeners to see any potential difference. By using the different hardeners a variation in the level of crosslinking was produced, along with a structural difference. They found that up to 2 GPa all three hardeners compressed in a similar manner in the P-V plane, with the data in the U_S-u_p plane also being comparable in nature.

Some polymers are used as the matrix layer in carbon fibre applications e.g. epoxy resins and phenolic resins. Many different types of epoxy resin have been investigated. One such epoxy resin used as a matrix material is RTM-6 (an aerospace grade epoxy

resin) which was investigated by Hazell *et al.* [70] and Appleby-Thomas *et al.* [71]. Hazell *et al.* found that the dynamic shock behaviour of RTM-6 was similar to other epoxy resins. They also found a deviation of the hydrodynamic pressure above 4 GPa. Appleby-Thomas *et al.* investigated among other properties the lateral stress behaviour of RTM-6 using embedded lateral stress gauges. The Hugoniot elastic limit and dynamic yield strength for RTM-6 was found to be comparable to other polymers for example PMMA and other epoxy resins.

A variety of other atypical systems have also been investigated at high strain rates. In the same way that there are natural and man made composites, there are natural and man made polymers. One such natural polymer is rendered porcine fat [72]. Porcine fat is made up of a backbone of glycerol with fatty acid side chains. Wilgeroth *et al.* used a single stage light gas gun to induce a shock wave into the fat with the shock response monitored by longitudinal and laterally orientated manganin pressure gauges. A linear Hugoniot was obtained, with the caveat that at very low u_p (less than 0.1 mm μs^{-1}) values non-linear behaviour could be assumed, primarily seen as a difference between c_0 and c_B, as had been seen in multiple polymers by Carter and Marsh [28]. When the data was viewed in the pressure planes (both pressure-volume and pressure-u_p) strengthening was noted taking the form of deviation from the Hugoniot. As with Appleby-Thomas *et al.* [71] lateral gauges were used. However no shear strength or HEL values were given, although it was noted that shear strength was independent of pressure with a small increase in shear strength noted from the resultant traces.

The porcine fat [72] was compared to the tissue simulants ballistics soap and gelatin by Appleby-Thomas *et al.* [73]. Again a single stage gas gun was used to impart the shock wave, with the response being monitored by manganin pressure gauges in both the longitudinal and lateral orientation. In the U_S-u_p plane a linear Hugoniot behaviour was noted. In the pressure-volume plane deviation was seen at the higher pressures investigated for the ballistics soap and porcine fat, whereas gelatin behaved hydrodynamically over the investigated range. The deviation from the hydrostat for the

porcine fat and ballistics soap was attributed to the polymer like nature of these materials, with the side groups helping to resist compression (similar to steric hinderance [74, Page 822]). Laterally orientated manganin pressure gauges were used to investigate the strength of the materials. Gradients were seen on the lateral traces implying a strengthening behind the shock.

To recap, for polymers non-linear behaviour has been noted in multiple materials, primarily in the difference between c_B and c_0. Scatter was noted in PMMA and thought to be due to manufacturing differences between different companies, a factor which may affect other polymers.

2.6 Strength Measurements of Materials

Many methods can be used for measuring the strength in a material. Vogler and Chhabildas investigated the strength behaviour of materials at high pressures using shock-reshock and shock-release techniques (the self consistent method), but usefully compared the different methods that can be used [75]. One method that is used in this study is the embedded lateral gauge (manganin in our case). These work on the principle of a change in resistance which is proportional to the shock stress, with the gauge orientated perpendicular to the direction of travel. When compared to the longitudinal stress for a corresponding shot the shear stress can be measured. Commercial lateral gauges however, only work up to a pressure of 25 GPa, due to the increased likelihood of breakdown of the backing/insulations material at this point; which is not an issue for the work conducted here.

Pressure-shear is another method of ascertaining the strength profile while under shock loading. With this technique both a longitudinal and transverse wave is generated within the same material at the same time which can then be used to ascertain the strength of the material. There are a variety pressure-shear experiments, some of which will be described here [76]. The first technique is the oblique plate impact method [77, 78].

This method uses an angled impactor and target (the angle for both is the same so that the impact is planar) to generate longitudinal and lateral waves within the material. The material strength is attributed to the difference between the longitudinal and bulk response. This method is limited by the target glue bond strength (about 20 GPa or 1000 m s^{-1}). The second experimental pressure-shear technique involves inducing a shock wave into a y-cut quartz buffer to simultaneously load the sample in both compression and shear [79]. By using a single VISAR beam which is split into two on the rear of the sample both the longitudinal velocity and transverse velocity can be obtained at the same time, leading to the pressure-shear loading of the material. This technique has a shear limit of 0.35 GPa that can be transmitted across the epoxy interface. The final variation of the pressure-shear technique that will be discussed here involves the use of an anvil [80, 81]. Within this setup a thin sample (*e.g.* 25 μm) is placed between a material such as tungsten carbide. This means that the wave induced into the sample is elastic in nature; and from the known impact velocity and transverse velocity from the rear of the anvil plate the stress, shear strains and strains rates can be calculated.

Harris and Winter by use of hydrocodes investigated the lateral stress in shock tantalum samples [82]. This model was compared to the data gathered by Gray *et al.* [83]. For the encapsulation layer a strengthless PMMA model was used. They also investigated whether the encapsulation had an effect on the lateral stress within the model by removing the encapsulation layer - with the resultant equilibrium stress in the simulation referred to as the far field stress. Encapsulation was found at lower pressures to make very little difference, as the pressure was increased the far field stress became much higher than the stress seen in the "encapsulation". These far field stress profiles did not match up to the experimental traces in either shape or stress achieved. When compared to the stress in the simulations of the encapsulated layer the model agreed well with the experimental traces. This suggests that the lateral stress seen in this encapsulation layer is not the lateral stress tantalum would see, but in fact a combined response of the tantalum and encapsulation layer leading to the observed lateral stress. Using this assumption it is possible to back

out the strength model for tantalum. This difference will matter less in polymers due to the close impedance match between the material and the encapsulated gauge package, usually meaning that the sample and gauge can be taken as one.

In further work on the encapsulation of lateral gauges Appleby-Thomas *et al.* investigated the effect that encapsulation had on the behaviour of multiple polymers [84]. One of the primary methods of investigating the encapsulation layer was to use a technique for the coupling of the two half samples of glued-joint and dry-joint. The glued-joint is the standard approach where the two halves are joined using a glue (epoxy) interlayer which the lateral gauge is suspended in. The dry-joint contained no glue interlayer for the gauge with the two halves joined on the outside edge of the target. Polymers were used so that the lateral stress seen by the gauge would be the same as the one in the sample, which may not be the case with some metals as seen by Harris and Winter [82]. The polymers investigated by the glued and dry-joint techniques were RTM-6 and polystyrene. Negative gradients were noted behind the shock on the lateral traces that were the same in all tests for a given material, but different in magnitude for RTM-6 and polystyrene for near identical impact conditions. It was suggested this decrease in stress was caused by one of two reasons, 1) a increase in material strength, or 2) dispersion of the shock front in the encapsulation layer leading to formation of a Mach stem. Overall as in each case both the glued and dry-joint had the same gradient and stress profile it was concluded that, at least for these polymers, encapsulation leads to no difference in the lateral stress profile. Differences were noted however on the initial rise with an overshoot seen on the dry-joint targets which was not seen/was damped out on the glued-joint samples. This phenomena was attributed to the nature of the glue joint; it was postulated that the glue interlayer acted as a cushioning area damping the response due to the applied force acting on a larger area. To determine the cause of this overshoot and gradient behind the shock a biological polymer, porcine fat previously investigated by Wilgeroth *et al.* [72] was used. As this material could be cast it was supposed that there should be no interlayer between the gauge and the sample. Similar results were seen

for the porcine fat compared to the polymers polystyrene and RTM-6. From this it was assumed that the gradient was caused by a material response.

Again using the glued and dry-joint Eliot *et al.* investigated the lateral gauge response of polycarbonate via experimental and computational methods [85]. To investigate the lateral response a single stage 50 mm diameter light gas gun was employed. Four experiments in total were performed at the same impact conditions, with the difference being how the two halves of the sample were joined together. Two targets were joined using the glued-joint, while the other two were joined using the dry-joint technique. With the experimental lateral traces a gradient was noted behind the shock front which was the same regardless of the interlayer. This gradient was different but comparable to other polymers, from which it would be reasonable to assume that the gradient is a material effect. Also as the gradients of the two joining techniques were the same it can be infered that the glue interlayer does not effect the lateral trace; at least behind the shock in a polymer, backing up the conclusions of Appleby-Thomas *et al.* in Reference [84]. As in Reference [84], an overshoot was also seen on the dry-joint lateral traces. The dry and glues-joints were modeled in a two-dimensional eulerian hydrocode with a mesh size of 12 μm which can be refined to 0.75 μm. These models showed the collapse of the dry-joint led to a non-linear front. No gradient was seen behind the shock but this may be due to the material model used in the simulation not being sufficiently complex.

The overshoots seen in the dry-joint traces of References [84] and [85] have also been seen in some metals [86], and even in cast polymers (*e.g.* porcine fat) [72, 84]. Due to this it would be reasonable to assume that the overshoot is caused by an impedance mismatch leading to Mach stem formation in either the interlayer, or the sample.

Using the self consistent method Lipkin and Asay [87] investigated the release and reshock behaviour of a 6061-T6 aluminium. Four experiments were performed all at the same initial impact pressure (2 GPa), with two different thicknesses of aluminum samples (6.3 and 12.6 mm). The shape and features of the traces were the same for both thicknesses (if thickness was accounted for within the shock traces). Through the use

of constitutive modeling good agreement was seen in the release for the aluminium and the initial recompression, though further investigation was needed in to the mechanism involved.

Following on from the work of Lipkin and Asay [31, 87], Huang and Asay investigated the strength of three aluminium alloys (based on 6061) with different grain sizes and two pure aluminium again with differing grain sizes, using the self consistent method [88]. To achieve the shock wave a 100 mm light gas gun and a 30 mm powder gun were employed, with a VISAR system to monitor the shock profile. The initial impact pressures reached were between 4 and 23 GPa. The recompression was independent of grain size and quasielastic in nature, and thought to be due to the shear stress being less than the yield strength. The inclusion of impurities and well as grain size does seem to alter ambient yield strength, but not the material strength.

2.7 Summary

Overall there is a lot of work on the shock response of different types of composite *e.g.* glass fibre, carbon fibre among others. There is less work concerned with the effect that orientation has on the shock profile, with the main investigations concerned with the fibres parallel and perpendicular to the shock front. In particular there is a paucity of data on the shock response of TWCP (one unpublished study [19]) and on strength measurements of carbon fibre composites (none on carbon fibre could be found by the author). For this reason this investigation will be based on obtaining an equation of state for a TWCP at differing orientation, as well as investigating the strength behaviour of these orientations. As well as investigating the response of the TWCP the matrix material will also be interrogated due to the low shock behaviour being dominated by the matrix material [15, 53].

Chapter 3

Experimental Method

3.1 Plate Impact Technique

One-dimensional shock waves were introduced into the sample material in these experiments using the plate impact technique. For all shots a single stage gas gun was used, in which compressed gas was employed to accelerate a flyer plate into a target to impart a shock. The single stage gas gun employed for these experiments has a 50 mm bore, with a 5 m barrel and is situated at the Defence Academy of the UK at the Shrivenham Campus of Cranfield University. The design and construction of this gun is explained in detail in Reference [89]. A simplified diagram is shown in Figure 3.1. Particular points to note include the breach where compressed gas used to accelerate the sabot to the desired velocities is held. The barrel extension contains the method of measuring the velocity of the sabot. This involves using a set of conductive pins which when impacted are shorted sequentially. This allows calculation of the velocity as the distances between the pins are known.

To accelerate the sabot two methods have been employed to control gas release. The original technique employed a pair of "bursting discs", with the second one involving the use of a fast acting valve. The bursting disc method relied on using two calibrated disc that failed at specific pressures. The basic setup is shown in Figure 3.2. The

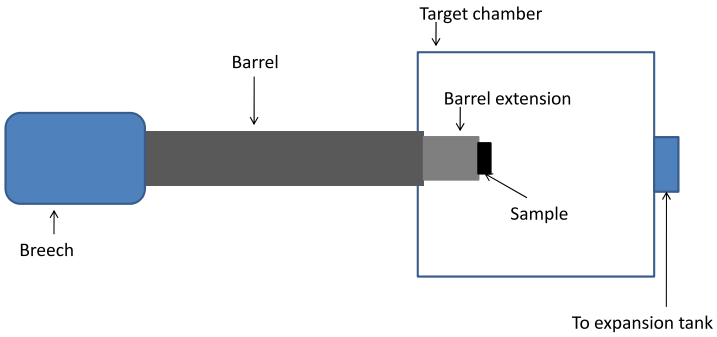

Figure 3.1: Simplified diagram of the Cranfield University single stage gas gun.

pressure established between the pair of bursting discs is called the holding pressure. This pressure was used to stop the breach pressure from prematurely causing the bursting discs to fail. For a firing, the breach and separator were filled at the same time to different pressures. For example if the breech pressure was required to be 300 bar the holding pressure used was 150 bar; with the bursting discs calibrated such that they would burst at an intermediate pressure. When the required pressures were reached the holding pressure was evacuated using a solenoid resulting in successive failure of both discs. The gas released then forced the sabot to accelerate down the barrel. Importantly an expansion tank on the rear of the gun allowed the pressurised gas to expand meaning that the gun itself (excluding the breech) was not a pressure vessel.

The fast acting valve works by using a piston, with a simplified setup shown in Figure 3.3. In operation the piston is initially held forward using a higher pressure region, with gas introduced via the inlet valve. This higher pressure is approximately 10 bar higher than the lower “filling” pressure. To fire the gun, the higher pressure region is evacuated, (using a solenoid via the outlet pipe); the lower pressure region now dominates forcing

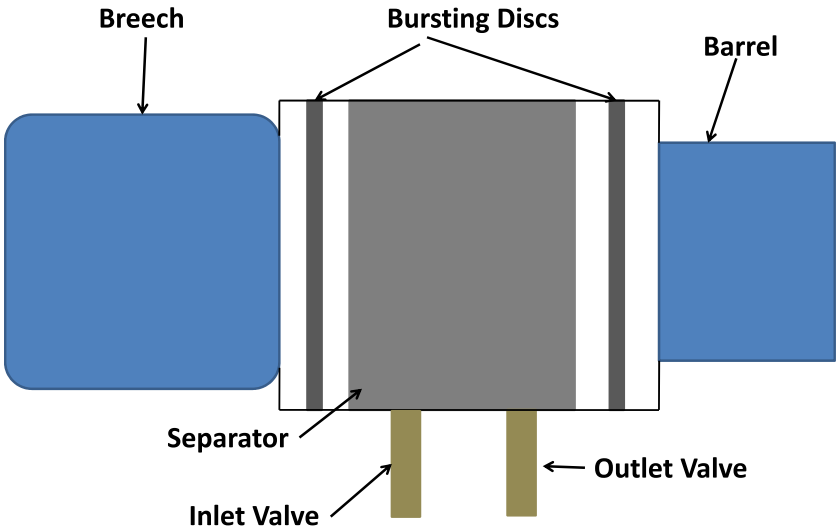

Figure 3.2: Simplified diagram of the bursting disc arrangement.

the piston back and allowing the gas to accelerate the sabot down the barrel.

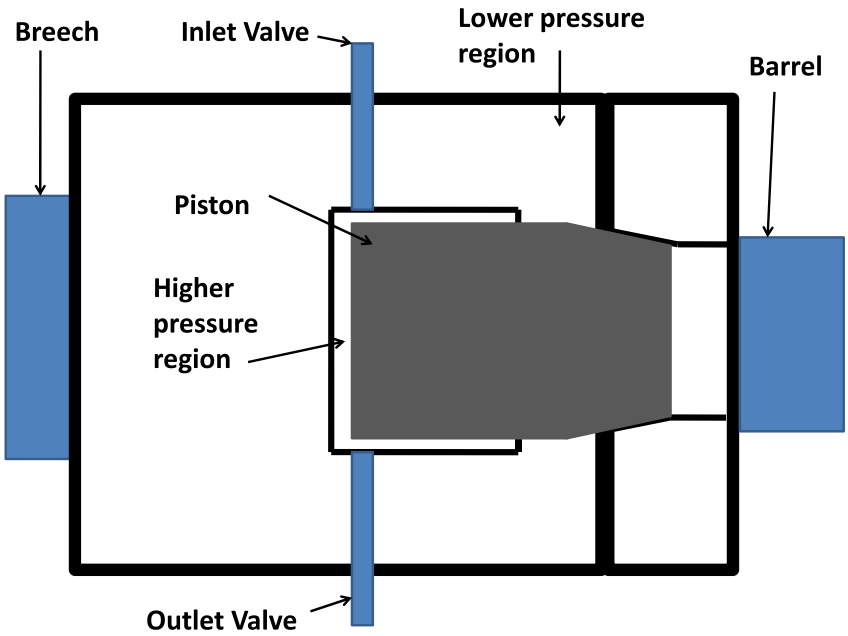

Figure 3.3: Simplified diagram of the fast acting valve.

Simplified diagrams of typical experimental sample set ups are shown in Figure 3.4, where a) is the longitudinal set up and b) is the lateral setup. Mylar® layers are introduced

between gauges to provide protection/insulation. The thickness of the Mylar® changes depending on the sample material. The thicker the Mylar® the more protection the gauge receives which can be useful if the sample has a fibreous nature. For example, Hazell *et al.* [17] and Millett *et al.* [16] observed a lower gauge response due to failure on the front gauge compared to the rear which had extra protection. For some of the experiments where the fibres in the TWCP samples were perpendicular to the shock front (90°), a PMMA offset was inserted between the sample and the rear gauge as shown in Figure 3.5. This technique was also used by Millett *et al.* [16] and Hazell *et al.* [17] to further enhance protection to the rear gauge compared to Mylar® alone. Further, in some of the later shots both lateral and longitudinal gauges were combined as shown in Figure 3.6, which has been done previously by Appleby-Thomas *et al.* [90].

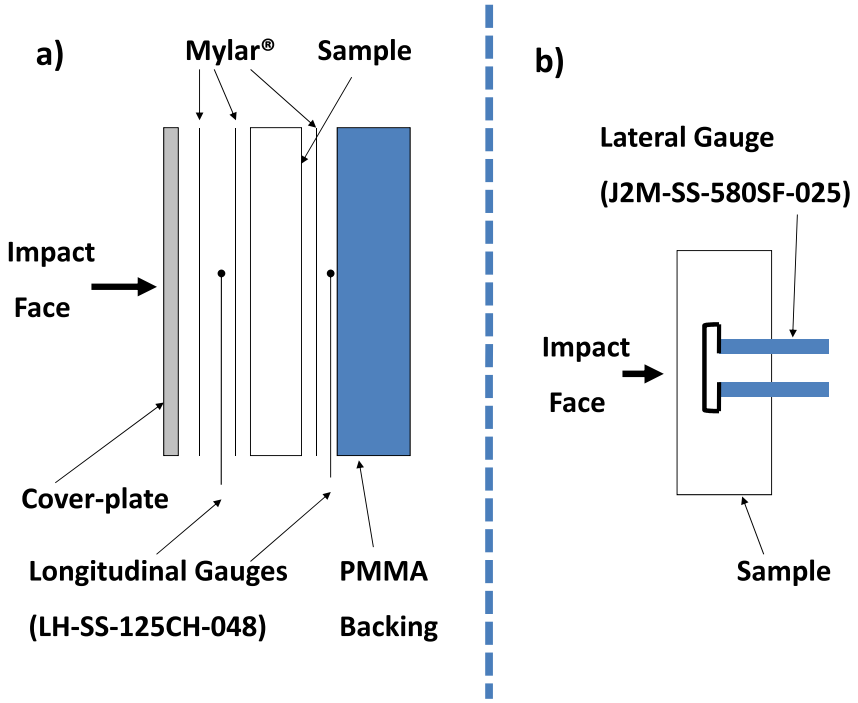

Figure 3.4: Simplified experiential setup for a) longitudinal and b) lateral samples.

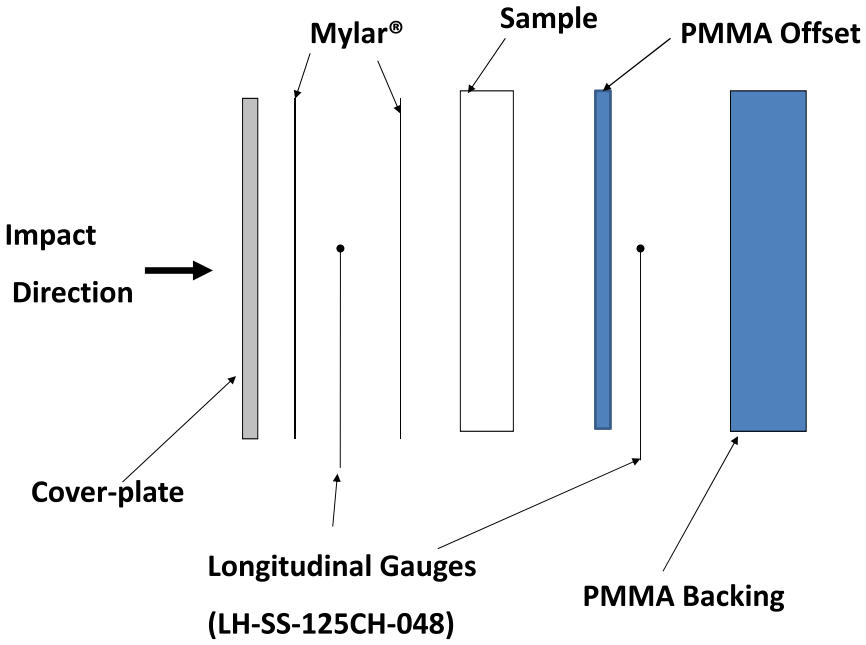

Figure 3.5: Simplified experimental setup for the longitudinal samples where the fibres in the TWCP were orientated perpendicular to the shock front with an extra PMMA protection layer.

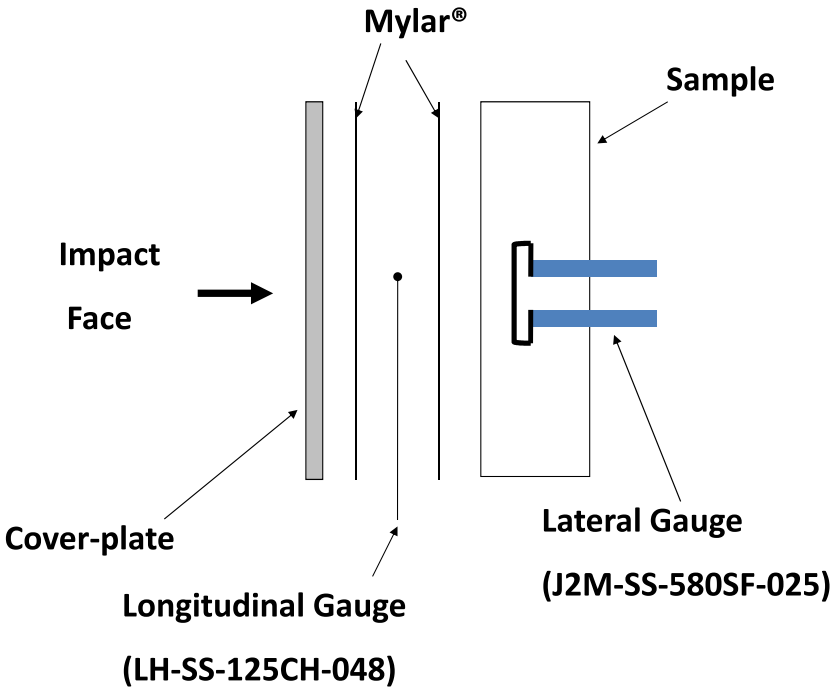

Figure 3.6: Simplified experimental setup for combined longitudinal and lateral samples.

3.2 Manganin stress gauges

The diagnostic's employed in this work were manganin stress gauges manufactured by Vishay Precision Group - Micro-Measurements. The gauges were of type LM-SS-125CH-048 for longitudinal experimental setups and J2M-SS-580SF-025 for lateral experimental setups. Manganin is an alloy of 84% copper, 4% nickel and 12% manganese [91], with the gauge element having a nominal resistance of 48 Ω for the LM-SS-125CH-048 (longitudinal) and 25 Ω for the J2M-SS-580SF-025 (lateral) type arrangements [92]. Manganin is used due to its relatively constant resistance over a range of temperatures, along with a high and near constant piezoresistance [46].

The two types of gauges used are shown in Figure 3.7 and 3.8 for the longitudinal lateral orientations respectively. For the longitudinal orientation the manganin is arranged in a grid pattern, with dimensions 3.18 by 4.45 mm. The gauge has a glass fibre reinforced epoxy phenolic backing for partial protection of the gauge as well as insulation on this protected side. Brass shim of thickness 50 μm is used as gauge legs for the longitudinally orientated gauges and attached to the tags shown in Figure 3.7 using an indium based solder, to connect the gauge to the equipment used. Indium solder is used due to it's low melting point which minimises the chance of damage during the assembly.

The lateral orientated manganin gauge is shown in Figure 3.8. The lateral gauge is 14.73 mm long with an height of 0.2 mm. As this is less clear in the photograph a diagram of the gauge has also been produced for clarity. The lateral gauge is encapsulated with a polyimide film making the gauge fully insulated.

Both the longitudinal and lateral gauges are attached to the equipment discussed latter in Section 3.3 via use of co-axial cabling employing BNC connectors. The manganin gauges are attached to a wheatstone bridge as shown in Figure 3.10.

By knowing the distance between the gauges (which is the thickness of the sample plus the thicknesses of the Mylar® sheets used in the gauge package) shock velocity can be calculated by using Equation 3.1.

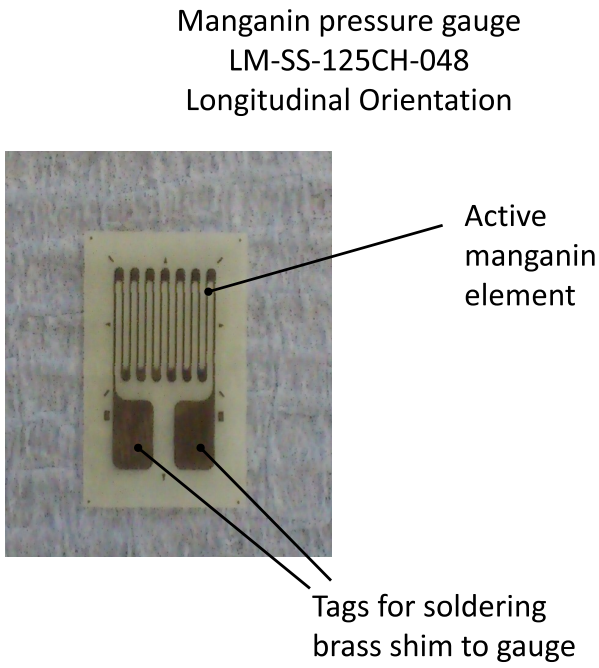

Figure 3.7: Annotated picture of a manganin pressure gauge for the longitudinal orientation.

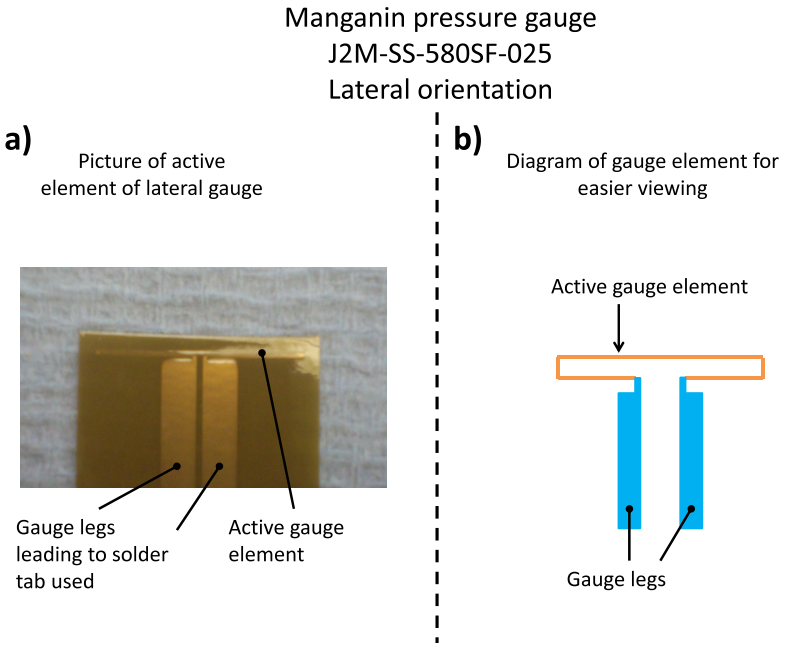

Figure 3.8: Annotated picture and diagram of a manganin pressure gauge for the lateral orientation.

$$Velocity = \frac{Distance}{Time} \tag{3.1}$$

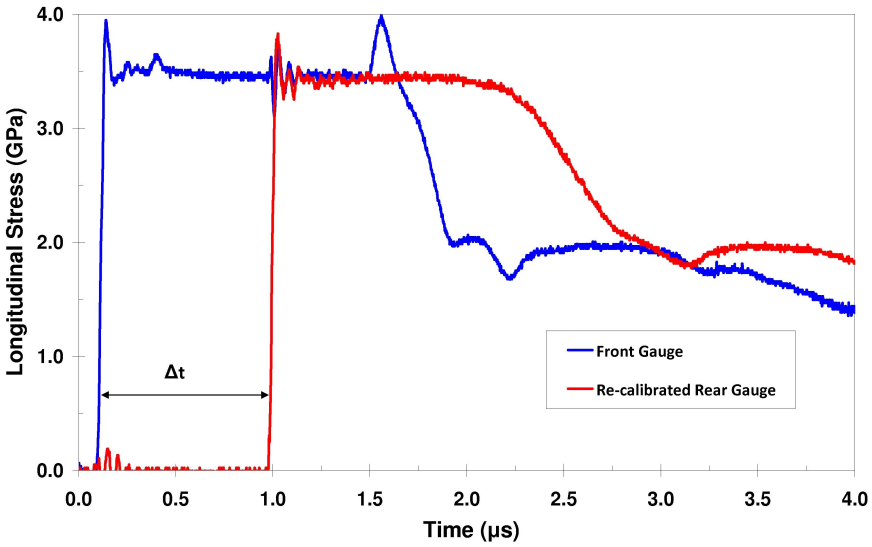

Figure 3.9: Processed longitudinal gauge traces.

The orientation and geometry of the gauges will effect the interpretation of the gauge results. The difference between longitudinal and lateral gauges is that one is configured one-dimensionally (longitudinal gauge) and one is in a two-dimensional configuration (lateral gauge) [93]. For a gauge in the one-dimensional configuration the strain and stress tensors are shown in Equations 3.2 and 3.3.

$$\bar{\varepsilon}_{1D} = \begin{pmatrix} \varepsilon_x & 0 & 0 \\ 0 & 0 & 0 \\ 0 & 0 & 0 \end{pmatrix} \tag{3.2}$$

$$\bar{\sigma}_{1D} = \begin{pmatrix} \sigma_x & 0 & 0 \\ 0 & \sigma_y & 0 \\ 0 & 0 & \sigma_y \end{pmatrix} \tag{3.3}$$

The two-dimensional configuration the strain and stress tensors are shown in Equations 3.4 and 3.5.

$$\bar{\varepsilon}_{2D} = \begin{pmatrix} \varepsilon_x & 0 & 0 \\ 0 & \varepsilon_x & 0 \\ 0 & 0 & 0 \end{pmatrix} \tag{3.4}$$

$$\bar{\sigma}_{2D} = \begin{pmatrix} \sigma_x & 0 & 0 \\ 0 & \sigma_x & 0 \\ 0 & 0 & \sigma_z \end{pmatrix} \tag{3.5}$$

3.2.1 Longitudinal Gauge Interpretation

The one-dimensional stress tensor which is used with the longitudinal gauge is given by Equation 3.6. Where Y_g is the yield strength of the manganin gauge. This leads to Equation 3.7 as shown in Reference [94].

$$\sigma_{ij} = \begin{pmatrix} \sigma_x & 0 & 0 \\ 0 & \sigma_x - Y_g & 0 \\ 0 & 0 & \sigma_x - Y_g \end{pmatrix} \tag{3.6}$$

$$P_{Hydrodynamic} = \sigma_x - \frac{2}{3} Y_g \tag{3.7}$$

For interpretation of the longitudinally orientated manganin pressure gauges two equations are used. When the gauge is in the elastic regime Equation 3.8 is employed instead. Above the elastic regime the gauge responds plastically with Equation 3.9 used. This transition between the elastic and plastic regime is the yield strength of the Manganin gauge. The coefficients used in these Equations are shown in Table 3.1 and were experimentally derived elsewhere (see Reference [46]). The value of ΔR is given by the change in voltage caused by the pressure exerted on the gauge. The value of R_0 is approximately 48.0 Ω and is found before the experiment using a multimeter.

$$P = \frac{1}{m_0} \left(\frac{\Delta R}{R_0} \right) \tag{3.8}$$

$$P = m_1 + m_2\left(\frac{\Delta R}{R_0}\right) + m_3\left(\frac{\Delta R}{R_0}\right)^2 + m_4\left(\frac{\Delta R}{R_0}\right)^3 + m_5\left(\frac{\Delta R}{R_0}\right)^4 \tag{3.9}$$

Coefficient Name	Coefficient Value
m_0	0.0195
m_1	0.572
m_2	29.59
m_3	95.20
m_4	-312.74
m_5	331.77

Table 3.1: Coefficients used for calibration in longitudinal manganin stress gauges.

To gain the ΔR value Equation 3.10 is used. This equation requires calibration of the gauge or gauges depending on how many are used. Gauge are calibrated by placing a known resistance across the gauge and measuring the voltage. This effectively simulates the passage of a shock wave on the gauge, thereby changing its resistance. This approach allows the voltage change in the gauge to converted in to a change in resistance allowing the co-efficients in Equation 3.10 to be derived.

$$Theoretical\Delta R = aV^2 + bV + c \tag{3.10}$$

The coefficients a and b are calculated by using the method of least squared fit, as shown in Table 3.2. This is where the values a and b are altered to give the lowest possible value for $\sum$Difference^2 as shown in Table 3.2. The Difference is found by taking the known resistance and then subtracting the theoretical resistance. This is then squared to get the value of Difference^2. This is then summed to get the value of ΣDifference^2. The theoretical resistance values are the ones altered to gain the lowest ΣDifference^2 by changing the coefficients a and b shown in Equation 3.10. The coefficient c, is set to a value of 0, as at a voltage of zero there is no resistance within the circuit. In this case the values of a and b are 1.187 and 8.320 respectively.

From this calibration data we can go from the change in voltage which results when a gauge is loaded, to the associated change in resistance in the gauge, and finally to the

Δ R (Ω)	**Voltage (V)**	**Theoretical ΔR (Ω)**	**Difference (Ω)**	**Difference^2 (Ω)**
Known ΔR	Measured Voltage	Value calculated from Equation 3.10	ΔR - Theoretical ΔR	Difference^2
0.220	0.0301	0.251510511	-0.032	9.9291×10^{-4}
0.696	0.0833	0.701305216	-0.005	2.8117×10^{-5}
1.466	0.1687	1.437391008	0.029	8.1847×10^{-4}
2.200	0.2470	2.127501514	0.072	5.2560×10^{-3}
4.710	0.5180	4.62840119	0.082	6.6584×10^{-3}
9.960	1.0400	9.937129752	0.023	5.2305×10^{-4}
14.650	1.460	14.67828243	-0.02828243	7.9990×10^{-4}
20.0	1.900	20.09449631	-0.094496305	8.9296×10^{-03}
30.0	2.620	29.94906377	0.050936229	2.5945×10^{-03}
			$\sum$	2.6601×10^{-2}

Table 3.2: Gauge calibration method.

pressure exerted on the gauge. To calculate the value for $\frac{\Delta R}{R_0}$ Equation 3.11 is used. This is a rearrangement of Equation 3.10 with the values of a, b and c gained through the experiment divided by the initial gauge resistance R_0. It is this ratio of $\frac{\Delta R}{R_0}$ that is used in Equations 3.8 and 3.9.

$$\frac{\Delta R}{R_0} = \frac{aV^2 + bV + c}{R_0} \tag{3.11}$$

After the stress is calculated for each gauge, the rear gauge needs to be impendence matched to obtain the stress in the sample as opposed to the stress in the backing. This is done by applying Equation 3.12 [71] to the stress measured in the rear gauge, where Z is the acoustic impedance of the material or backing given by Equation 3.13.

$$\sigma_{Sample} = \frac{1}{2}\frac{Z_{Sample} + Z_{Backing}}{Z_{Backing}}\sigma_{Rear\,gauge} \tag{3.12}$$

$$Z = \rho_0 U_S \tag{3.13}$$

3.2.2 Lateral Gauge Interpretation

The two-dimensional stress tensor which is used with the lateral gauge is given by Equation 3.14. Where Y_g is the yield strength of the manganin gauge. From this it leads to Equation 3.15.

$$\sigma_{i,j} = \begin{pmatrix} \sigma_y + Y_g & 0 & 0 \\ 0 & \sigma_y & 0 \\ 0 & 0 & \sigma_y \end{pmatrix} \tag{3.14}$$

$$P_{Hydrodynamic} = \sigma_y + \frac{1}{3} Y_g \tag{3.15}$$

For lateral gauges a different analysis is used, which is based on the change in volumetric strain ε_v that the gauge experiences. As with the longitudinal gauge the lateral gauge response has both plastic and elastic elements. The lateral gauge has a lower resistance (25 Ω) with a 22 Ω resistor placed in series to increase the total resistance of the gauge package to $\sim$ 48 Ω for use with the pulsed power supply employed in the laboratory. The gauges are calibrated in the same manner as longitudinal ones (using Equation 3.10 along with table 3.2). From this multiple equations are used to calculate the lateral stress exerted on the manganin gauge by the sample. Due to the number of equations Table 3.3 has been created to show all the terms used in the calculation of lateral stress.

To calculate volumetric strain Equation 3.16 is employed. Equation 3.16 is the response of the manganin gauge in its plastic range which is Δ_{pl}, with the coefficient values obtained by Rosenberg *et al.* [95].

$$\Delta_{pl} = \frac{\Delta R}{R_0} = 9.89\varepsilon_v^2 + 3.45\varepsilon_v + 5.17 \times 10^{-4} \tag{3.16}$$

Equation 3.16 is rearranged into Equation 3.17, which can be solved via the quadratic equation (Equation 3.18). This leads to Equation 3.19 where the positive root of the

Term	Description
Y_g	The yield strength of the manganin gauge
P	The hydrodynamic pressure of the manganin gauge
ε_v	Volumetric strain of the gauge
a,b and c	Quadratic coefficients of manganin gauge found from calibration
ΔR	Change in resistance of the manganin gauge
R_0	Resistance of the lateral gauge
σ_y	Lateral stress
Δ_{el}	The manganin gauge response in the elastic region
M_g	Longitudinal modulus of the manganin gauge which is 174 GPa or 1740 kbar
β	A constant of the material and gauge
G_g	The Lamé constant of the gauge which is 43.5 GPa of 435 kbar
M_m	Longitudinal modulus of the sample material
ν_m	Poisson's ratio of the sample

Table 3.3: Terms used in the equations for calculation of lateral stress.

quadratic equation is used.

$$0 = 9.89\varepsilon_v^2 + 3.45\varepsilon_v + 5.17 \times 10^{-4} - \Delta_{pl} \tag{3.17}$$

$$x = \frac{-b \pm \sqrt{b^2 - 4ac}}{2a} \tag{3.18}$$

$$\varepsilon_v = -3.45 + \frac{\sqrt{11.9025 - 39.56(5.17 \times 10^{-4} - \Delta_{pl})}}{19.78} \tag{3.19}$$

Following calculations of the volumetric strain, the hydrodynamic pressure exerted on the manganin gauge can be calculated using Equation 3.20; with the pressure in kilobars (10 kbar = 1 GPa). The values of 4120 and 1160 were determined by Barsis *et al.* [91], and are based on the pressure response of manganin.

$$P = 4120\varepsilon_v^2 + 1160\varepsilon_v \tag{3.20}$$

The yield strength exerted on the gauge is given by Equation 3.24 where the coefficient values are calculated from the Equations used by Rosenberg and Brar in [30].

$$Y_g = 0.14995P + 6.5542 \tag{3.21}$$

To calculate σ_y the value of Δ at the elastic-plastic boundary is required (known as "critical" delta Δ_c). If the value of $\frac{\Delta R}{R_0}$ is less than the value of Δ_c then Equation 3.22 is used to calculate σ_y, otherwise Equation 3.23 is used.

$$\sigma_y = \frac{\Delta R}{R_0}\frac{M_g}{3.45\beta} \tag{3.22}$$

$$\sigma_y = P - \frac{1}{3}Y_g \tag{3.23}$$

To calculate the critical delta for use in σ_y manipulation of multiple equations is required. First Equation 3.20 is substituted into Equation 3.21 leading to Equation 3.24.

$$Y_g = 0.14995(4120\varepsilon_v^2 + 1160\varepsilon_v) + 6.554 \tag{3.24}$$

Next Equation 3.23 is substituted into Equation 3.25 leading to Equation 3.26.

$$\Delta_{el} = \frac{3.45}{M_g}\beta\sigma_y \tag{3.25}$$

$$\Delta_{el} = \frac{3.45}{M_g}\beta\left(P - \frac{1}{3}Y_g\right) \tag{3.26}$$

Next, substituting for Y_g from Equation 3.24 into Equation 3.26 gives,

$$\Delta_{el} = \frac{3.45}{M_g}\beta(4120\varepsilon_v^2 + 1160\varepsilon_v - \frac{1}{3}(0.14995(4120\varepsilon_v^2 + 1160\varepsilon_v) + 6.554) \tag{3.27}$$

Collating the like terms leads to Equation 3.28.

$$\Delta_{el} = \frac{3.45}{M_g}\beta((41201 - \frac{1}{3}0.14995)\varepsilon_v^2 + 1160(1 - \frac{1}{3}0.14995)\varepsilon - \frac{1}{3}6.554) \tag{3.28}$$

Which simplifies to,

$$\Delta_{el} = \frac{3.45}{M_g}\beta(3914.07\varepsilon_v^2 + 1102.02\varepsilon - 2.18) \tag{3.29}$$

Note: For ease of viewing the decimal places of the following equations have been reduced to 2 decimal places, but for actual calculations the full figure was used.

At the elastic-plastic boundary of the manganin, the lateral elastic stress is equal to the lateral plastic stress. This means $\Delta_{el} = \Delta_{pl} = \Delta_c$ and therefore equating Equations 3.16 and 3.29 gives,

$$9.89\varepsilon_v^2 + 3.45\varepsilon_v + 5.17 \times 10^{-4} = \frac{3.45}{M_g}\beta(3914.07\varepsilon_v^2 + 1102.02\varepsilon - 2.18) \tag{3.30}$$

Rearranging and simplifying this result leads to Equation 3.31.

$$\left(9.89 - \frac{13503.54}{M_g}\beta\right)\varepsilon_v^2 + \left(3.45 - \frac{3801.97}{M_g}\beta\right)\varepsilon_v + 5.17 \times 10^{-4} + \frac{7.54}{M_g}\beta = 0 \tag{3.31}$$

The value of β can be calculated by Equation 3.32, where G_g is a constant of the gauge and M_m and v_m are given by Equations 3.33 and 3.34 respectively; where ρ_0 is the density of the sample material, c_L is the longitudinal wave speed and c_S is the shear wave speed. Both c_L and c_S are properties of the material that can be found by using ultrasonic techniques explained in greater detail in Section 3.4.

$$\beta = 1 + \left(\frac{2G_g}{M_m}\right)\left(\frac{1 - v_m}{v_m}\right) \tag{3.32}$$

$$M_m = \rho_0 c_L^2 \quad (\times 10\ for\ kilobar) \tag{3.33}$$

$$v_m = \frac{c_L^2 - 2c_S^2}{2c_L^2 - c_S^2} \tag{3.34}$$

The quadratic equation (Equation 3.18) can be used, with the constants a_ε, b_ε and c_ε shown in Equations 3.35, 3.36 and 3.37, to solve Equation 3.31.

$$a_\varepsilon = 9.89 - \frac{13503.54}{M_g}\beta \tag{3.35}$$

$$b_\varepsilon = 3.45 - \frac{3801.97}{M_g}\beta \tag{3.36}$$

$$c_\varepsilon = 5.17 \times 10^{-4} + \frac{7.54}{M_g}\beta \tag{3.37}$$

As mentioned, from the roots calculated, the positive value (obtained from the negative root of the quadratic equation), is used in Equation 3.38 (where R_+ is the positive value given by the negative root from the quadratic equation) which gives the value of Δ_c. From this the values of σ_y can be calculated over the whole elastic-plastic range of the manganin gauges.

$$\Delta_c = 9.89R_+^2 + 3.45R_+ + 5.17 \times 10^{-4} \tag{3.38}$$

However Rosenberg *et al.* have shown that an alteration is needed for this technique due to the above calibration being based on foil gauges [96]. This difference in geometry (foil compared to wire elements) was noted as a difference in the change in resistances when the wire gauges were compared to the foil gauges. The wire gauges, as used here, had a lower change in resistance until an approximate $\frac{\Delta R}{R}$ of 0.13, where the resistance change is the same and the above calibration method can be used. Below this value of $\frac{\Delta R}{R}$

the $\frac{1}{3}$ Y_g used in Equation 3.23 can be omitted to account for the difference in geometry.

3.3 Equipment Used

Table 3.4 shows the equipment used with the manganin gauges, along with an overview of its application.

Equipment	Purpose
Farnell E320/2	Power supply for velocity pins
Dynasen CC2-50/0.050-300	Power supply for gauges
Tektronix TDS 5140	Oscilloscope to collect gauge data
Tektronix TDS 460A	Oscilloscope to calculate the velocity of flyer at impact

Table 3.4: Experimental equipment used.

The Dynasen pulsed power supply is used to power the gauges during the shots. Figure 3.10 shows the electrical schematic obtained from the Dynasen power supply instruction manual [97]. The pulsed power supply works in a similar manner to a wheatstone bridge where one of the resistors is the gauge used in the experiments. The power supply is activated by trigger pins with the Dynasen supplying a 10 V pulse over a few microseconds. This then supplies the power to the gauges for a set amount of time just before impact, so that the gauges do not burn out due to resistive heating before the experiment is completed. The voltage supplied to the gauges is 5 V.

To record the data from the gauges a 5 GS/s Tektronix TDS 5140 oscilloscope was used, typically operating at 1.25 GS/s. The oscilloscope records data every 1.5982 nanoseconds, measuring a corresponding voltage at every time interval. This voltage was then converted to a pressure using the calibration technique mentioned in Chapter 3.2.

For velocity measurements a Tektronix TDS 460A oscilloscope was used. This oscilloscope was connected to each pair of conductive pins used for velocity measurement. As each pair of pins were shorted a pulse was seen, and due to the distance between sequential pins being known (12 mm) the velocity could be ascertained.

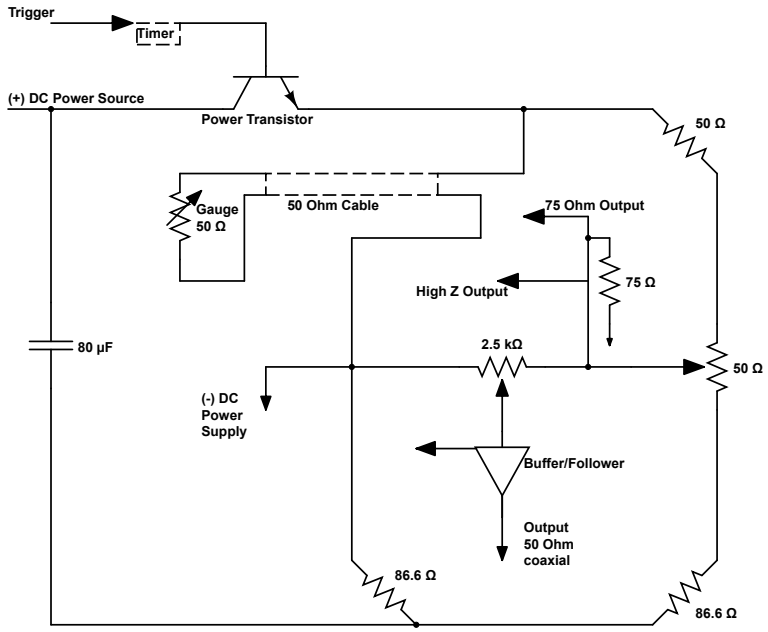

Figure 3.10: Configuration of manganin gauges with respect to the Dynasen power supply.

3.3.1 Density Measurements

A micrometric AccuPyc® 1330 gas pycnometer was used to measure the density of the samples. The gas pycnometer works by measuring the volume the sample takes up in its target chamber. By putting the sample in, the amount of gas used will be less and the volume can be calculated from the difference between the amounts of gas used. By measuring the mass of the sample, Equation 3.39 can then be used to calculate the density. Multiple measurement were taken of the samples to ensure an accurate value.

$$Density = \frac{Mass}{Volume} \tag{3.39}$$

The gas pycnometer works better with rigid samples, as softer materials can deform as the gas is pumped in. This will decrease the volume of the sample leading to a higher density measurement.

3.3.2 Optical Microscopy

An Olympus BX60 optical microscope was used, with images captured using a QImaging MicroPublisher 3.3 RTV colour camera. The optical microscope was used in brightfield mode (where the light is reflected off the surface of the sample at right angles). To analyse the images the software program Image-J was used. Using this program the dimensions of the images were ascertained, as were sample volume fractions. Both approaches are explained in greater detail in Section 4.3.2.

3.4 Ultrasonic Measurements

Ultrasonic measurements were used to determine most of the unshocked material properties, by finding values of c_L and c_S. The ultrasound is produced in a transducer, with a diagram of a ultrasonic transducer shown in Figure 3.11 (modified from Reference [98]). The active element is made of a piezoelectric or ferroelectric material which converts electrical signal into a ultrasound wave. A backing material is placed behind the active element and chosen to control the behaviour of the ultrasonic pulse. The wear plate is used to protect the active element from the sample being measured (along with any interlayers that may be used to provide a better signal transmission). Different transducers (longitudinal and shear) are used to ascertain different properties of the materials. If needed a coupling material can be used which is usually water or a more viscous material (*e.g.* treacle). This is particularly helpful for shear measurements, providing a transmission medium for the ultrasonic wave so that attenuation does not occur between the transducer and sample. As well as alleviating the attenuation the medium provides a physical coupling to the sample. To help with attenuation within a sample different frequencies can be used. A higher frequency (lower wavelength) will penetrate the sample less but has a higher spatial resolution. If a lower frequency (higher wavelength) is used then the ultrasonic wave will penetrate the sample more but the resolution will be lower. For polymers and lower density materials, a lower frequency

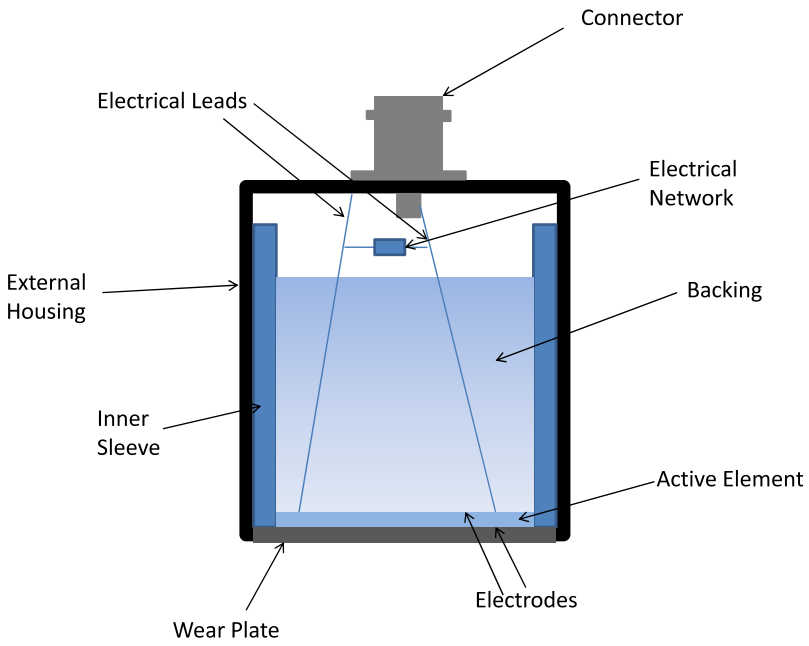

Figure 3.11: Ultrasonic transducer.

is used as polymers tend to be highly attenuating. To find the ultrasonic values, repeating patterns are looked for in the ultrasound signal displayed on an oscilloscope. It is best to take this time value over multiple reflections, if possible, to help reduce the error within the system. By knowing the thickness of the sample the ultrasonic wave speeds can be ascertained. Two methods can be used to obtain ultrasonic measurements, pulse-echo and transmission-receive. Pulse-echo uses one transducer which acts and both the pulse sender and the pulse receiver. This means the ultrasonic pulse has travelled to the rear of the sample, reflected off the rear and travelled back to the transducer. Any repeating patterns will have travelled twice the thickness of the sample, and this will need to be taken into account when calculating the ultrasonic speed values. The transmit-receive method involves using two transducers, one to transmit the signal and one to receive the signal, one on either side of the sample. By minimising the transit path this gives the greatest chance of capturing a clean signal, especially for highly attenuating materials.

Figure 3.12 shows a longitudinal ultrasonic measurement trace for a 50 mm diameter copper rod of thickness 10 mm. A Panametrics Videoscan 1 MHz transducer was used

in the pulse-echo configuration to obtain the ultrasound measurement for this figure. Multiple reflections were used to reduce the error within the system, with the number of reflected pulses used in this calculation being 8 in total. Using this time value as well as the known thickness of the sample, a longitudinal wave velocity of 4.77±0.02 mm μs^{-1} was obtained which agrees with the quoted value of 4.76 mm μs^{-1} given by Carter in Reference [29, Page 57].

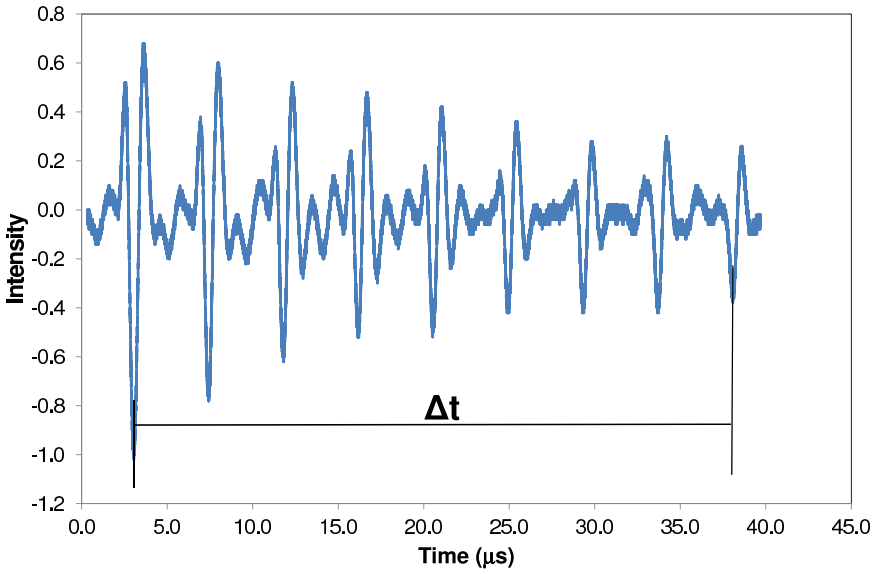

Figure 3.12: Longitudinal ultrasound trace for the 50 mm diameter copper rod.

This result leads to a maximum error on the transducer values of ±0.02 mm μs^{-1} for c_L. Comparable errors were noted in the traces for c_S; and consequently an error of ±0.03 mm μs^{-1} was assumed for the values of c_B which were calculated using Equation 2.18.

Chapter 4

Results and Discussion

4.1 Error Analysis

All equipment and methodologies will have an error associated with them. By understanding these errors, validation can be given to the experimental data gathered. The types of errors that are encountered fall into two categories. These are, experimental errors and systematic errors. Experimental errors are issues such as the thickness of a sample caused by physical properties or techniques used, compared to systematic errors which are introduced via equipment such as the vernier caliper used to measure the thickness of the sample. The errors induced by the technique will contribute to the total error. The main error will come from relative alignment of the sample with respect to the surface of the flyer plate.

All components are machined and so will have an associated error in terms of the final dimensional precision. All machined components have a $\pm$ 10 μm error associated with them. Over a sample width of 60 mm this leads to a maximum error of 0.17 milliRadians. This figure is found by using the trigonometric formulae given in Equation 4.1, rearranged to give the corresponding angle Equation 4.2. The value used for the opposite is 10 μm, with the value of adjacent being 60 mm. To account for the flyer plate the opposite value is doubled to 20 μm, this gives a maximum error of 0.4 milliRadians. Other errors occur

from gluing the components together along with attaching the sample to the target ring and placing this onto the barrel extension. The error associated with this will be with respect to the sabot and target ring, and not the relationship between the sample and flyer. With this current method a maximum error of 2 milliradians was noted in Reference [99], but the error tends to be around 0.3 milliradians.

$$tan\theta = \frac{Opposite}{Adjacent} \tag{4.1}$$

$$\theta = tan^{-1}\left(\frac{Opposite}{Adjacent}\right) \tag{4.2}$$

The measured parameters that will be affected by the misalignment will be U_S, u_p and the stress measured in the sample. The larger the misalignment the greater the rise time of the manganin gauges. Due to this fact it is much easier and more useful to use the rise time of manganin gauges to calculate the errors for U_S and u_p. The value for the stress will be reduced by misalignment, but for this change to be notable the rise time would need to be so slow that the traces would be unusable. For this reason the error in stress is not equated to the rise time of the manganin gauges. Manganin gauges have a finite rise time, with the fastest rise time possible being of the order of 40 ns due to the thickness of the gauge package. Figure 4.1 shows the position for the minimum and maximum rise time for both the front and rear gauges for a typical experimental pair of gauge traces. The rise time for the front gauge is 72 ns with the rear gauge rise time being 61 ns. The gauge failure has been removed from the front gauge and most of the rear trace has been removed for ease of viewing. Figure 4.2 shows the front gauge enlarged for clarity. For the lowest error, the minimum time value is taken, which is defined as the point when the stress increases above a base value greater than the background noise. For the maximum error associated with the rise time, the value taken is when the stress plateaus. From these maximum and minimum values the errors for U_S can be found. By taking the minimum time on the front gauge and the maximum time on the rear gauge the lowest possible

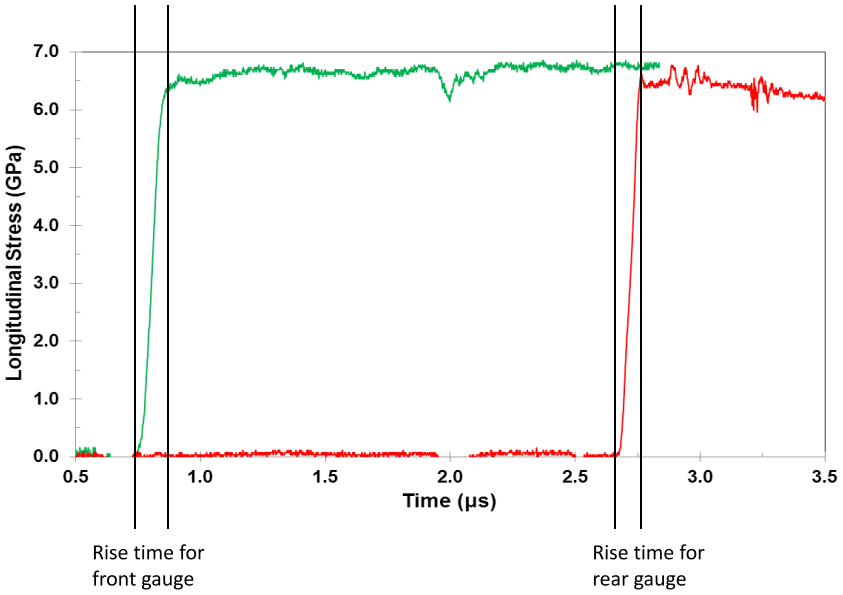

Figure 4.1: Error associated with the rise time of manganin gauges.

value of U_S will be gained. In conjunction the highest value of U_S, the maximum time on the front gauge is taken as well with respect to the minimum time on the rear gauge, and vice-versa for the lowest value of U_S.

From the errors found for U_S the associated errors of u_p can be found by using the impedance matching technique. This will also lead to a minimum and maximum value of u_p. Both of these errors are then used on the Hugoniot in the U_S-u_p plane to ascertain the quality of data. The other Hugoniot plane used in this project is the pressure-volume plane. For the error in stress the difference in stress between the front and rear gauge is taken. Calculations of volume is based upon the errors of U_S and u_p. Consequently to calculate the associated errors for the full range of potential values for the volume, are derived using Equations 4.3 and 4.4.

$$Volume^{MAX} = V_0 \left(\frac{U_S^{MAX} - u_p^{MAX}}{U_S^{MAX}} \right) \tag{4.3}$$

$$Volume^{MIN} = V_0 \left(\frac{U_S^{MIN} - u_p^{MIN}}{U_S^{MIN}} \right) \tag{4.4}$$

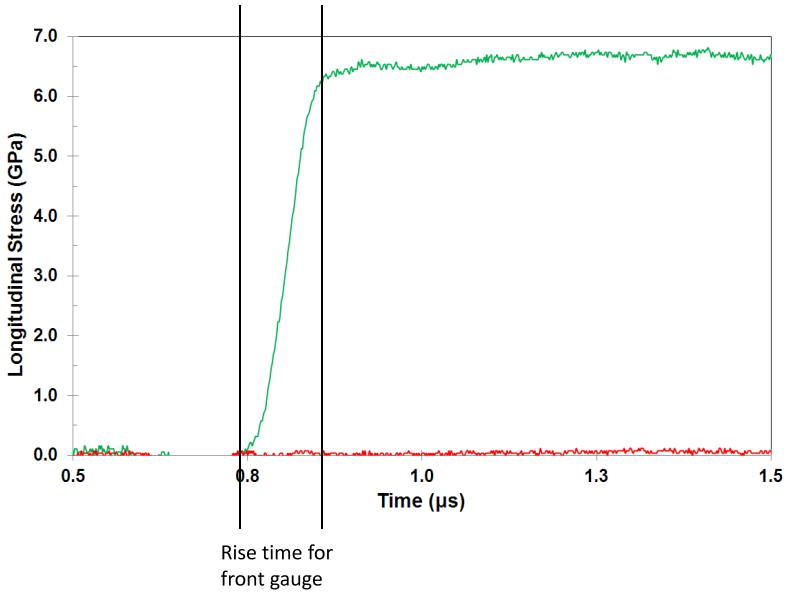

Figure 4.2: Enlarged view of the front gauge with associated error.

Equations 4.3 and 4.4 are extremely sensitive to changes in U_S and u_p, which when lateral and longitudinal gauges are combined could lead to a larger error in the volume plane.

The error in density was minimised due to the repetition in the measurements, with multiple samples employed. For each material the density measurements were taken not only by the manufacturer Lockheed-Martin, but also using a pycnometer. Each use of the gas pycnometer yields 5 results and these tests were repeated at least twice giving a minimum of 10 density measurements. As these results were consistent no further measurements were taken. The error found from the average value was $\pm$ 0.004 g cm^{-3} which it was felt was small enough to disregard in subsequent calculations involving density.

The velocity errors are primarily due to the acceleration the sabot is experiencing as it exits the barrel. The measuring system employed either shorting graphite or brass pins. The highest accuracy was obtained by the graphite pins. This was due to the brass pins not being completely straight which led to a greater error. However over the 36 mm measurement distance this error was minimised. The overall error on the velocity with

the system employed here is $\pm$ 0.5% [100].

All equipment used has a natural error in the reported accuracy however this error is negligible when compared to the error associated with the sample, and consequently such precise error analysis was largely neglected in this study.

4.2 Phenolic Resin Durite SC-1008

As discussed by Zaretsky *et al.* [15] the matrix material will dominate the behaviour of the composites at low impact velocities. Due to this the matrix material of the composite was investigated independently first. The matrix material used in the investigated composite TWCP is the phenolic resin Durite SC-1008. Obtained material properties are shown in Table 4.1, with density calculated using the gas pycnometer as explained in Section 3.3. The values of c_L and c_S were measured using ultrasonic transducers as detailed in Chapter 3.4, with the other elastic constants found using these values of c_L and c_S using the equations from Section 2.1.

The initial traces obtained using the experimental set up of two longitudinally orientated manganin pressure gauges as seen in Figure 3.4a, are shown in Figure 4.3. As can be seen these traces are extremely noisy in nature. Despite this noise it is possible, though difficult, to use these traces to obtain values of U_S, σ_x and u_p. An in-depth investigation found the cause of this noise to be due to the small size of the samples (the sample size was less than 30 mm). This led to multiple problems during the manufacture of the target. Some of the issues encountered during the target preparation were bending at the edge of the coverplate leading to misalignment, delamination between components, and off center alignment of the sample, leading to the gauges seeing the

ρ_0 g cm^{-3}	c_L mm μs^{-1}	c_S mm μs^{-1}	c_B mm μs^{-1}	ν	G GPa
1.18	2.67 $\pm$ 0.02	1.38 $\pm$ 0.02	2.14 $\pm$ 0.03	0.36	2.24

Table 4.1: Key elastic material properties of Durite SC-1008.

reflection/release from the edge of the sample sooner. To counteract the small size of the sample a containment ring was constructed, which is shown in Figure 4.4. The hole in the center of the containment ring was larger than the diameter of the phenolic resin samples. The phenolic resin sample was then held in place using an epoxy resin. This could then be machined to the required tolerances needed. A typical resultant target is shown in Figure 4.5, where the width was 60 mm. By using this technique no more noise was seen in the traces, and a cleaner trace can be seen in Figure 4.6, which is comparable in nature to the noisy trace seen in Figure 4.3.

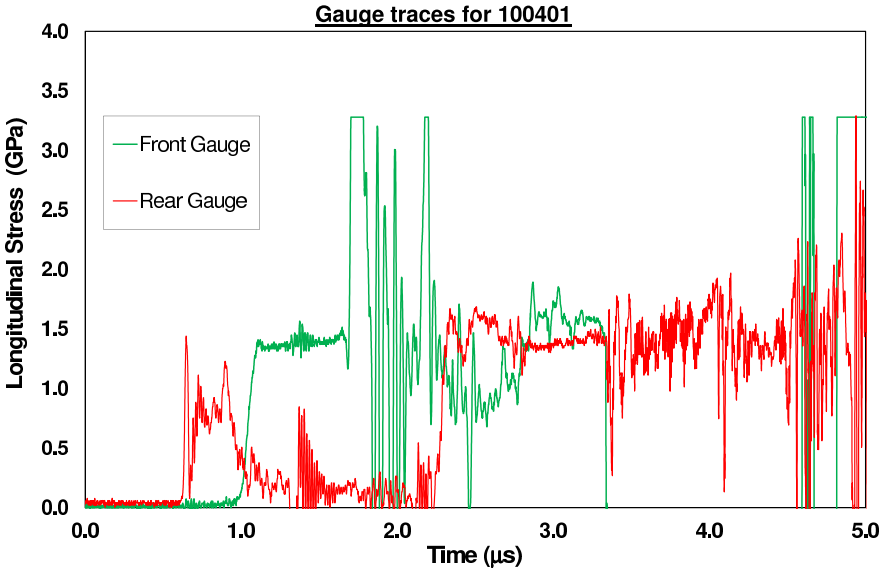

Figure 4.3: Initial Durite SC-1008 gauge traces for a 10 mm Al flyer travelling at 485 m s^{-1}.

Using this containment method the rest of the experiments were performed. The data for the longitudinally orientated gauges is shown in Table 4.2.

Using this data the Hugoniot in the U_S-u_p and pressure-volume plane was found. Figure 4.7 shows the Hugoniot in the U_S-u_p plane, with Figure 4.9 showing the Hugoniot in the pressure-volume plane. Using Figure 4.7 the obtained Hugoniot equation of state was found and is given in Equation 4.5. It is interesting to note that the data obtained before the confinement method matches up well with the confinement method data. The main difference comes from the larger errors on the data points when compared to the

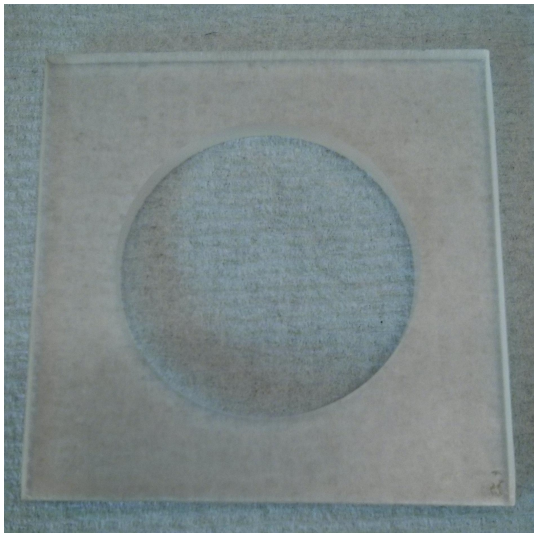

Figure 4.4: PMMA containment ring used for noise reduction.

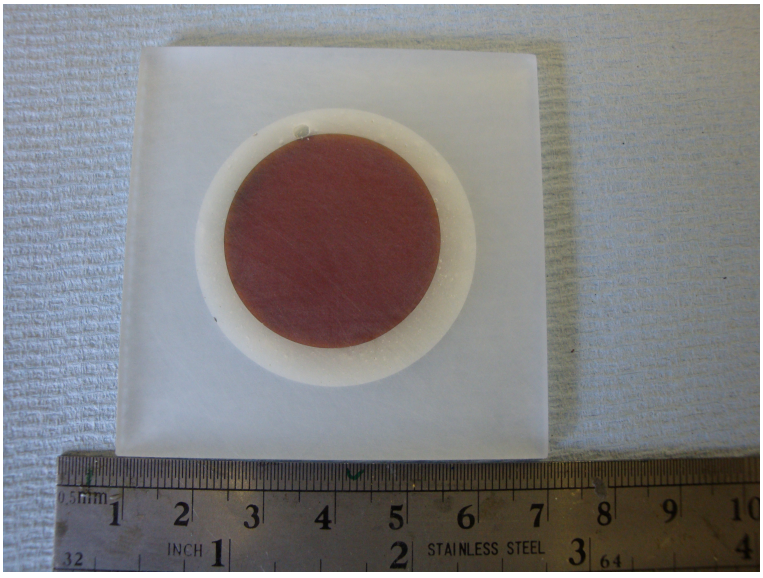

Figure 4.5: Sample completed with PMMA containment ring.

confinement method, but this validates the confinement ring data as seen in Table 4.2.

$$U_S = 2.14 + 3.79u_p - 1.68u_p^2 \tag{4.5}$$

The Hugoniot for the phenolic resin Durite SC-1008 is non-linear in nature with the intercept c_0 matching up with the value for c_B, which was obtained using the ultrasonic methods. This low particle velocity, non-linear Hugoniot behaviour has been seen in

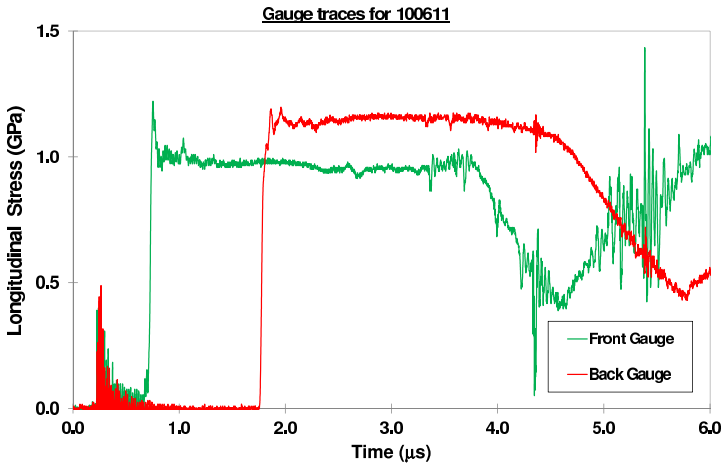

Figure 4.6: Clean gauge traces obtained using the containment method for a 10 mm Al flyer travelling at 350 m s^{-1}.

Experiment Number	Velocity m s^{-1}	Flyer Thickness/ Material mm	U_S mm μs^{-1}	u_p mm μs^{-1}	v cm^3 g^{-1}	σ_x /P GPa	Confinement Method
100615	80	10 Al	2.32	0.06	0.83	0.12	Yes
100303	200	10 Al	2.69	0.16	0.80	0.51	No
100611	350	10 Al	3.19	0.27	0.78	0.97	Yes
100401	485	10 Al	3.11	0.38	0.75	1.39	No
100423	600	10 Cu	3.77	0.53	0.73	2.31	No
100310A	810	10 Al	3.87	0.62	0.71	2.90	No
100622	960	5 Al	3.88	0.73	0.69	3.46	Yes
100618	970	5 Cu	4.26	0.85	0.68	4.65	Yes

Table 4.2: Experimental results obtained using longitudinal gauges for Durite SC-1008.

other polymeric materials, such as PMMA [26], polyurethane replacement resin [27] and various epoxy resins [28]. Carter and Marsh [28] attribute this behaviour to the difference in the strength of forces between the backbone chain and the inter chain bonds. The inter chain forces are weaker than the covalent forces of the polymer backbone chain. This means that on shock-loading, initial compression occurs at the weaker inter chain bonds. After this initial compression the backbone behaviour then dominates. It is these weaker inter chain forces that lead to the non-linear shock behaviour, before the backbone forces come into play leading to the linear response in higher u_p elements of the U_S-u_p Hugoniot.

Also included on Figure 4.7 is the low particle velocity data collected by Carter and

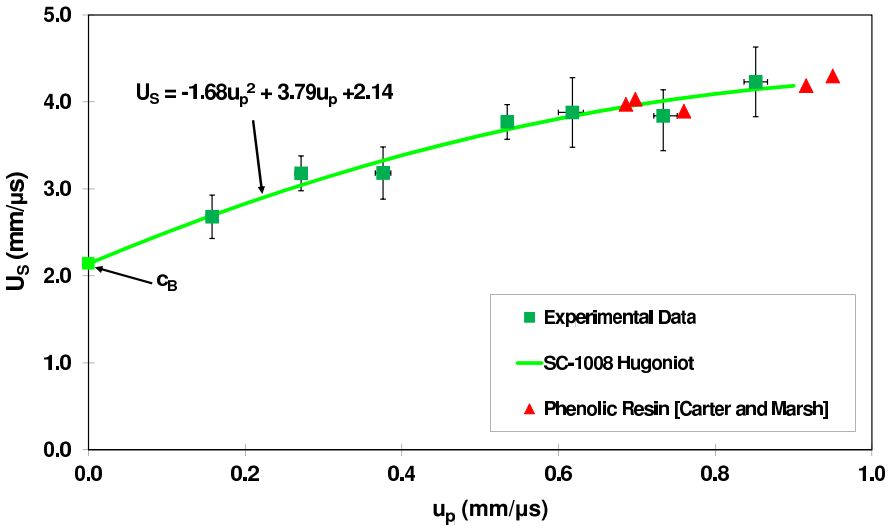

Figure 4.7: Hugoniot for Durite SC-1008 in the U_S-u_p plane.

Marsh for the phenolic resin Durite HR-300 Borden [28]. The Hugoniot equation of state for Durite HR-300 Borden was found to be $U_S = 2.98 + 1.39u_p$. This low particle velocity data agrees well with the higher particle velocity derived in this study. This may suggest that both these phenolic resins have very similar compositions leading to similar shock profiles as seen in the epoxy resin investigated by Munson and May [69] where the difference was a change in the hardener. If this is the case then for the lower shock response (below 20 GPa where a change in the Hugoniot was noted by Carter and Marsh) a two tiered response should be seen. For the low end below a u_p of 0.6 mm μs^{-1} the non-linear shock Hugoniot found here is appropriate. Above this value the linear shock Hugoniot found by Carter and Marsh may need to be used. This concept is shown more clearly in Figure 4.8. With their data Carter and Marsh noted a discrepancy between their values of c_0 and c_B which are 2.44 and 2.98 mm μs^{-1} respectively. Looking at the values of c_B along with the density of the sample (Durite HR-300 Borden has a density of 1.4 g cm^{-3}) it is reasonable to assume that the composition of both phenolic resins are different. This then means that the fact that both resin data sets match is more than likely coincidental, especially as there is no data for the Durite SC-1008 resin above the u_p value of 1 mm μs^{-1}, and for Durite HR-300 Borden below a u_p value of 0.7 mm μs^{-1}.

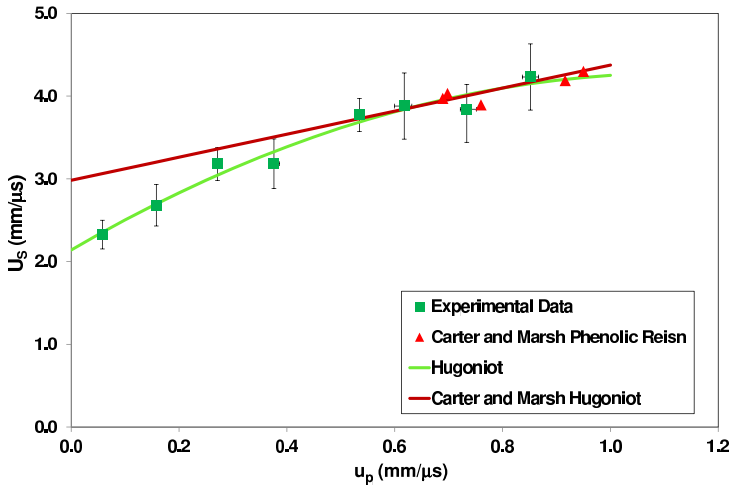

Figure 4.8: Hugoniot data for the phenolic resin Durite SC-1008.

The Hugoniot for the pressure-volume plane is shown in Figure 4.9. A unitless volume is used to allow for direct comparison between different materials. All of the experimental data with the exception of the highest value lies on the hydrostat, and is more than likely due to the non-linear nature of the Hugoniot. This implies that, initially at least, the SC-1008 possesses no strength while under shock loading. However, above 4 GPa deviation is seen from the hydrostat implying the material is starting to strengthen behind the shock front. This behaviour is similar to other polymeric materials including polycarbonate [100], polypropylene [68], polystyrene [68] and RTM-6 [70]. Further, the compressibility of the SC-1008 is greater than the phenolic resin investigated by Carter and Marsh. A linear Hugoniot was obtained with the equation $U_S = 2.36 + 2.27u_p$. By using this Hugoniot in the pressure-volume plane, it is clear to see the deviation seen with the non-linear equation has disappeared. This would add support to the higher particle velocity experimental data being linear in nature in the U_S-u_p plane. It is interesting to note that if a linear Hugoniot is used in the U_S-u_p plane the data agrees reasonably if the errors bars are included in the analysis. For the non-linear materials of PMMA [26] and polyurethane replacement resin [27] no pressure-volume graphs were included in the papers so these can not be used for comparrisions in the pressure-volume plane against other materials. Presumably these would also show deviation at higher u_p due to the

nature of the non-linear quadratic equation.

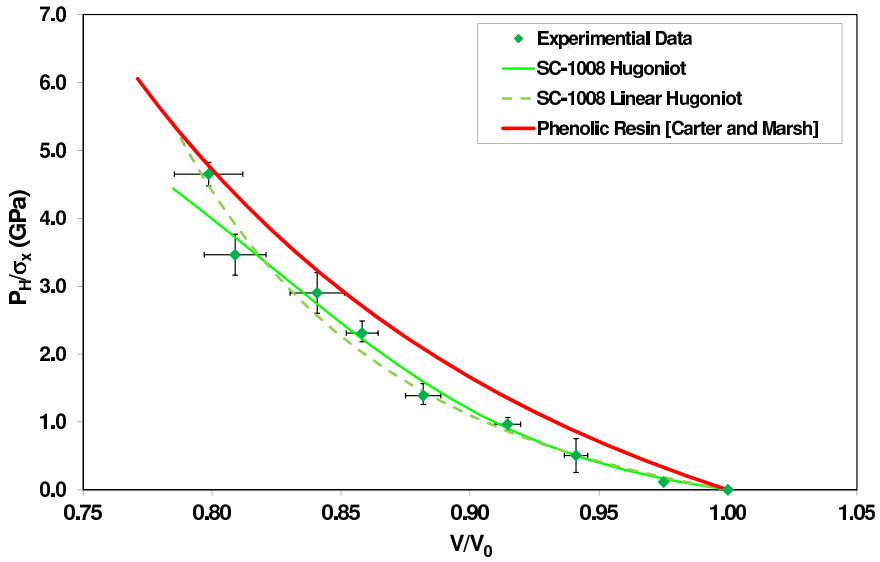

Figure 4.9: Hugoniot for Durite SC-1008 in the pressure-volume plane.

4.2.1 Strength behaviour of Durite SC-1008

Using manganin pressure gauges in the lateral orientation as shown in Figure 3.4b, Table 4.3 was obtained. Due to the impact conditions being known the value of u_p is found using the impedance matching technique. From this the value of U_S is found by using the known Hugoniot equation of state given by Equation 4.5, with the value of σ_x/P_H found using the hydrodynamic equation (given by Equation 2.15). Figure 4.10 shows all of the lateral traces for the shots detailed in Table 4.3 plotted together with an altered time base. Four main points can be seen with the lateral gauge traces shown in Figure 4.10, which is annotated to draw attention to each point. The first point to note is the rapid rise time of the gauge. This rise time decreases as the shock velocity increases.

An overshoot is present on the higher pressure traces which has been seen in other materials such a polymers using the dry-joint technique [84, 85] and metals [82, 83], and is thought to be due to a slight impedance mismatch leading to a Mach stem effect in the gauge package. The pressure then stabalises to a plateau due to the lateral stress exerted

Experiment Number	Velocity m s^{-1}	Flyer Thickness/ Material mm	U_S mm μs^{-1}	u_p mm μs^{-1}	v cm^3 g^{-1}	σ_x /P GPa	σ_y GPa	Yield Strength GPa
100709A	145	10 Al	2.67	0.12	0.81	0.36	0.25	0.11
100708B	320	10 Al	3.01	0.26	0.78	0.93	0.74	0.19
100706B	500	10 Al	3.38	0.40	0.75	1.59	1.30	0.29
100715	670	10 Cu	3.80	0.60	0.71	2.69	2.32	0.37
100713	865	10 Cu	4.05	0.76	0.69	3.65	3.00	0.65

Table 4.3: Experimental results obtained using lateral gauges for Durite SC-1008.

on the material. Finally a reloading effect can be seen which is due to the geometry of the sample and the containment ring method. As discussed previously, the yield strength 2τ may be calculated via Equation 2.25 for the experimental data and Equation 2.31 for the elastic prediction. By comparing the yield strength of the material to an elastic prediction given by Equation 2.31 the Hugoniot elastic limit can be ascertained. This is shown graphically in Figure 4.11. From this the Hugoniot elastic limit was found to be 0.36±0.10 GPa. The lowest data point is elastic in nature and taken as the Hugoniot elastic limit. The relatively large error bars arise from the noise present within the trace due to the low impact conditions as can be seen in Figure 4.10.

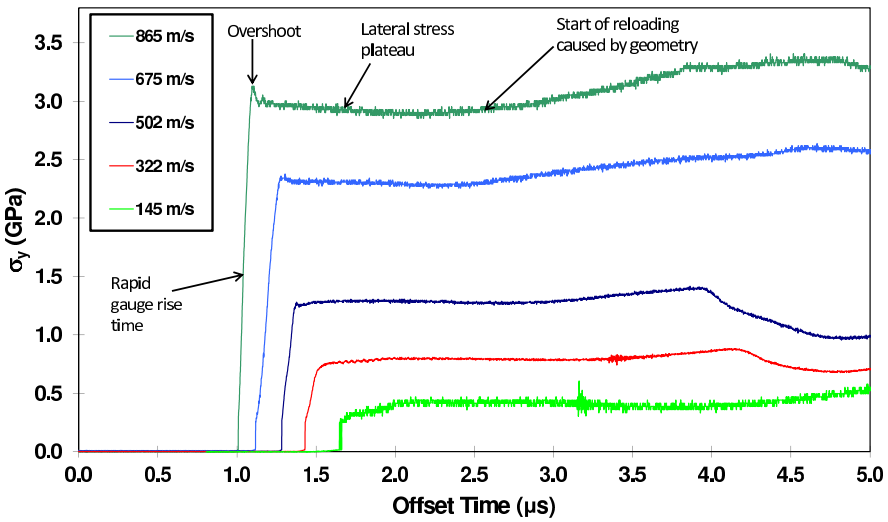

Figure 4.10: All experimentally measured lateral stress traces for Durite SC-1008.

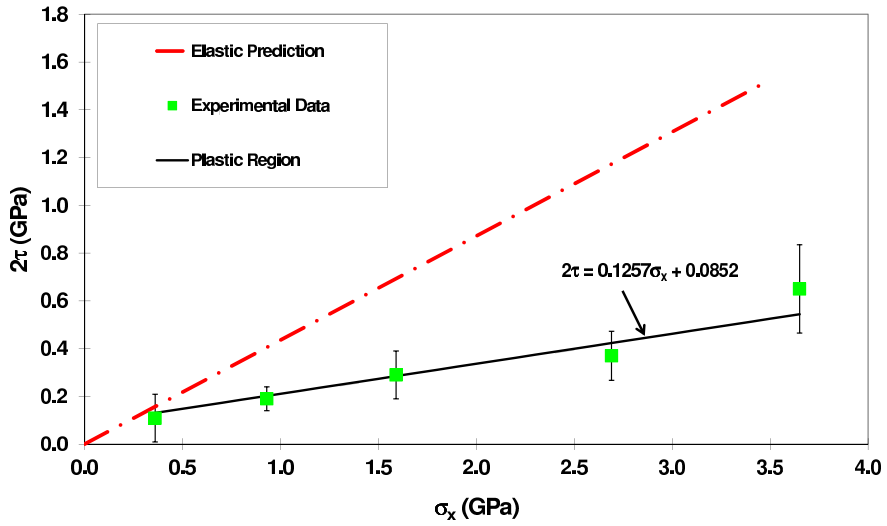

Figure 4.11: Shear strength of Durite SC-1008.

4.2.2 Summary

A non-linear shock Hugoniot was found for the matrix material, with the equation U_S 2.14 + 3.79u_p - 1.68u_p^2. This non-linear Hugoniot behaviour agrees with other polymeric materials. No deviation was seen in the pressure-volume plane until the higher pressure investigated here, again similar to other polymers investigated under shock loading. This deviation however disappeared when a linear Hugoniot was used in the pressure-volume plane. A Hugoniot elastic limit was found, with the value being 0.36±0.10 GPa, comparable in nature to other polymeric materials.

4.3 Carbon Fibre Composite

The key elastic properties of the TWCP are shown in Table 4.4 for all the different weave angles investigated in this project, along with the elastic properties of the 20° TWCP investigated by Burrell *et al.* [19]. The ultrasound data for the 20° TWCP only included the values of ρ_0, c_L and c_S, with the other values calculated by the standard equations given in Section 2.1. As the densities of all the TWCP samples are the same it can be reasonably assumed that samples all have the same volume fraction. This means that any

Cloth Angle Degrees	ρ_0 g cm^{-3}	c_L mm μs^{-1}	c_S mm μs^{-1}	c_B mm μs^{-1}	ν	G GPa
0	1.46	3.61 $\pm$ 0.02	2.00 $\pm$ 0.02	2.78 $\pm$ 0.03	0.28	5.96
20 [19]	1.48$\pm$0.01	3.63$\pm$0.03	0.99$\pm$0.03	3.45$\pm$0.04	0.46	1.45
25	1.46	3.55 $\pm$ 0.02	1.00 $\pm$ 0.02	3.36 $\pm$ 0.03	0.46	1.46
45	1.46	3.47 $\pm$ 0.02	1.04 $\pm$ 0.02	3.26 $\pm$ 0.03	0.45	1.57
90	1.46	4.20 $\pm$ 0.02	2.01 $\pm$ 0.02	3.50 $\pm$ 0.03	0.35	5.90

Table 4.4: Key elastic material properties of TWCP.

difference seen in the shock response is due to the angle of the weave. The ultrasound measurements show some similarities between the orientations. As it can be seen the c_L values are broadly similar for the weave orientations of 0°, 25° and 45°. In comparison the 90° has a higher c_L value presumably due to the orientation of the fibre weave allowing the bulk elastic wave value to be increased as was seen in Dyneema® [58]. The c_S sound speeds for the 0° and 90° have approximately the same values. Further, the c_S values for the 20°, 25° and 45° layups are half that of the 0° and 90°. It seems reasonable to assume this is caused by the angle of the weave smearing the shear wave leading to a lower value of c_S. This also leads to a higher value of Poisson's ratio which should affect the lateral stresses of the material in these orientations. It is interesting to note that for the the weave angles 25° and 45° the values of c_B and c_L converge due to the low value of c_S. This should result in very little elastic behaviour in the composite especially in terms of a precursor at these angles in the TWCP material. A precursor was seen in the off-angle composite investigated by Bordzilovsky *et al.* [20].

4.3.1 Elastic Constants

Due to the importance of the angle with respect to the shock front, and the precursor due to the propagation of the elastic wave in the fibres, it is important to understand the elastic constants of the material. Due to the anisotropic nature of the composite material, anisotropic elastic values were obtained. From the ultrasound values the elastic constants shown in Equation 2.34 can be ascertained using the methods mentioned by

Propagation direction	Particle motion direction	Corresponding angle and ultrasound mode	Nomenclature	Value mm μs^{-1}
[100]	[100]	90° c_L	V_1	4.20
[100]	[010]	90° c_S	V_2	2.01
[100]	[001]	90° c_S	V_3	2.01
[010]	[100]	90° c_L	V_4	4.20
[010]	[010]	90° c_S	V_5	2.01
[010]	[001]	90° c_S	V_6	2.01
[001]	[100]	0° c_L	V_7	3.61
[001]	[010]	0° c_S	V_8	2.00
[001]	[001]	0° c_S	V_9	2.00
[110]	[110]	90° c_L	V_{10}	4.20
[110]	[$\bar{1}$10]	90° c_S	V_{11}	2.01
[110]	[001]	90° c_S	V_{12}	2.01
[101]	[110]	45° c_L	V_{13}	3.47
[101]	[$\bar{1}$01]	45° c_S	V_{14}	1.04
[101]	[010]	45° c_S	V_{15}	1.04
[011]	[011]	45° c_L	V_{16}	3.47
[011]	[0$\bar{1}$1]	45° c_S	V_{17}	1.04
[011]	[100]	45° c_S	V_{18}	1.04

Table 4.5: Ultrasound measurements used for calculation of elastic constants.

Dandekar *et al.* [13]. Table 4.5 shows the corresponding propagation direction, particle motion direction, nomenclature, corresponding angle and ultrasound wave speed in the orientation in question; this table has been adapted in part from [13]. For the elastic constants the z direction has been taken so that the layers are perpendicular to it.

To find the elastic constants Equation 4.6 is used. Table 4.6 shows the relationship between the nomenclature and the elastic constants.

$$C = \rho V^2 \tag{4.6}$$

Using the equations shown in Table 4.6 along with Equation 4.7, the elastic constants of the carbon fibre composite can be found. These values can be seen in Table 4.7. This leads to a elasticity tensor shown in Equation 4.8 where $C_{ij} = C_{ji}$, and due to the symmetry of the material $C_{13} = C_{23}$.

Nomenclature	Elastic stiffness constants (ρV^2)
V_1	C_{11}
V_2	C_{66}
V_3	C_{55}
V_4	C_{22}
V_5	C_{66}
V_6	C_{44}
V_7	C_{33}
V_8	C_{55}
V_9	C_{44}
V_{10}	$0.5C_{66}+0.25(C_{11}+C_{22}+0.5[(C_{12}+C_{66})^2+0.25(C_{22}-C_{11})^2]^{1/2})$
V_{11}	$0.5C_{66}+0.25(C_{11}+C_{22}-0.5[(C_{12}+C_{66})^2+0.25(C_{22}-C_{11})^2]^{1/2})$
V_{12}	$0.5(C_{55}+C_{44})$
V_{13}	$0.5C_{55}+0.25(C_{11}+C_{33}+0.5[(C_{13}+C_{55})^2+0.25(C_{11}-C_{33})^2]^{1/2})$
V_{14}	$0.5C_{55}+0.25(C_{11}+C_{33}+0.5[(C_{13}+C_{55})^2+0.25(C_{11}-C_{33})^2]^{1/2})$
V_{15}	$0.5(C_{66}+C_{44})$
V_{16}	$0.5C_{44}+0.25(C_{22}+C_{33}+0.5[(C_{23}+C_{44})^2+0.25(C_{22}-C_{33})^2]^{1/2})$
V_{17}	$0.5C_{44}+0.25(C_{22}+C_{33}+0.5[(C_{23}+C_{44})^2+0.25(C_{22}-C_{33})^2]^{1/2})$
V_{18}	$0.5(C_{66}+C_{55})$

Table 4.6: Relationship between the nomenclature and elastic constants.

$$C = \rho V^2 \tag{4.7}$$

Elastic constants	Values (GPa)
C_{11}	25.75
C_{33}	19.03
C_{44}	5.90
C_{66}	5.90
C_{12}	16.24
C_{13}	18.15

Table 4.7: The values of the elastic constants.

$$C_{ij} = \begin{bmatrix} 25.75 & 16.24 & 18.15 & 0 & 0 & 0 \\ 16.24 & 25.74 & 18.15 & 0 & 0 & 0 \\ 18.15 & 18.15 & 19.03 & 0 & 0 & 0 \\ 0 & 0 & 0 & 5.90 & 0 & 0 \\ 0 & 0 & 0 & 0 & 5.90 & 0 \\ 0 & 0 & 0 & 0 & 0 & 5.90 \end{bmatrix} \tag{4.8}$$

Looking at the elastic tensor matrix shown in Equation 4.8, two distinct regions can be seen. The top left made up of 9 elements, are all comparable in nature with the difference being less than 10 GPa. This may mean very little difference between the different orientations, however whether this applies to the shock regime is unknown. The bottom right corner has the same value, due to the value of c_S being comparable for both the 0° and 90° lay ups on which these values are based. Again whether this is reflected in the high rate experiments is unclear.

4.3.2 Optical Microscopy of TWCP

Micrographs of the carbon fibre composite are shown in Table 4.8. For the micrographs the TWCP samples were sectioned and then potted using an epoxy resin; with the surfaces then polished back using various cloths to a 1 μm finish. An optical microscope was used in brightfield mode (where the light is reflected off the surface of the sample at right angles). In Table 4.8 a) and b) are from the 0° orientation with c) and d) being 45° and 90° lay ups respectively. In this figure the over and under nature of the weave can be seen. The thickness of the fibre bundles are between 150 to 300 μm thick. This puts the weave thickness of each cloth layer to be between 300 to 600 μm. Figure b) in Table 4.8 shows individual fibres at a higher magnification. From this it is possible to find that the fibre thickness is between 6 and 8 μm. A micrograph of the 45° lay up is shown in Figure c) and looks mostly the same as the 0° orientation except that it looks more smeared, which is expected due to the angle. Figure d) shows a 90° weave orientation and again looks

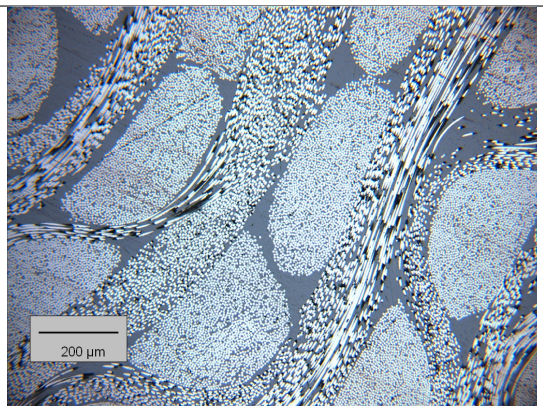

a) 0° orientation of TWCP

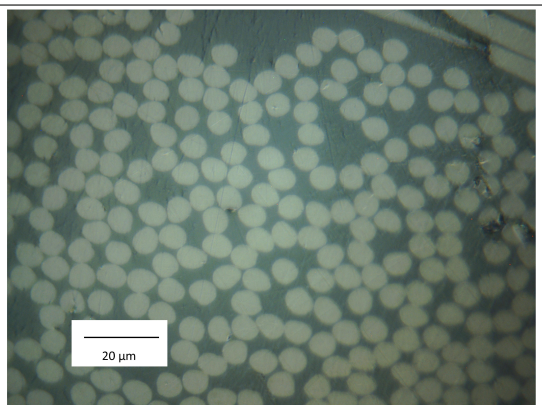

b) TWCP 0° at higher Magnification

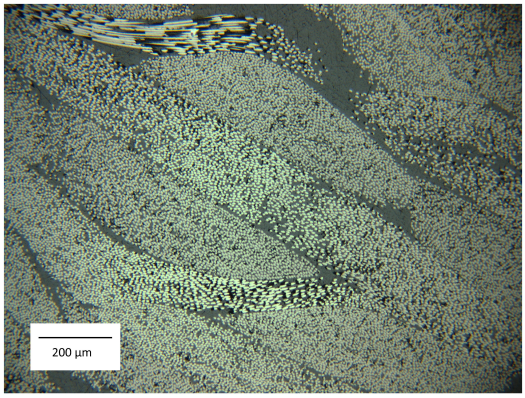

c) 45° orientation of TWCP

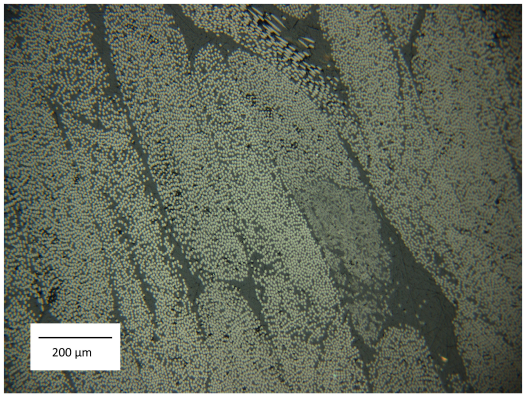

d) 90° orientations of TWCP

Table 4.8: Optical micrographs of TWCP.

broadly similar to the 0° orientation.

By using the optical micrographs the volume fraction of the TWCP can be calculated. As the density is the same for all orientations, it would be reasonable to assume that the volume fraction would be the same regardless of orientation. This was done by turning the image in to a binary image (fibres in black resin in white) using the software Image-J and measuring the ratios. This was done over multiple magnifications and weave orientations giving a volume fraction for the fibres of 54±4%. Using this and the known densities of the matrix material (Durite SC-1008) and the composite as a whole a density for the fibres can be found, which is 1.70 g cm^{-3}. It should also be noted that, for the different orientations of TWCP, the volume fraction remains constant in the micrographs within the associated error.

4.4 Shock Response of TWCP

For the results of the TWCP, the lateral gauge data for all orientations has been separated into their own section for easier comparison and discussion.

4.4.1 0° Lay up

The 0° weave orientation TWCP material was initially investigated. The reason for starting with this orientation was that Millett *et al.* [16] found that this weave orientation behaves as if it is monolithic in nature. Using the experimental set up for longitudinally orientated manganin pressure gauges shown in Figure 3.4a the experimental data was obtained and is shown in Table 4.9. A typical experimental trace pair is shown in Figure 4.12. In this figure the rise time of the gauges are on the order of 60 ns with this slight increase compared to previous data being due to the use of thicker Mylar® (50 μm compared to 25μm). On the plateau oscillations can be seen thought to be due to the thickness of the weave with this behaviour explained in greater detail in Section 4.4.2.

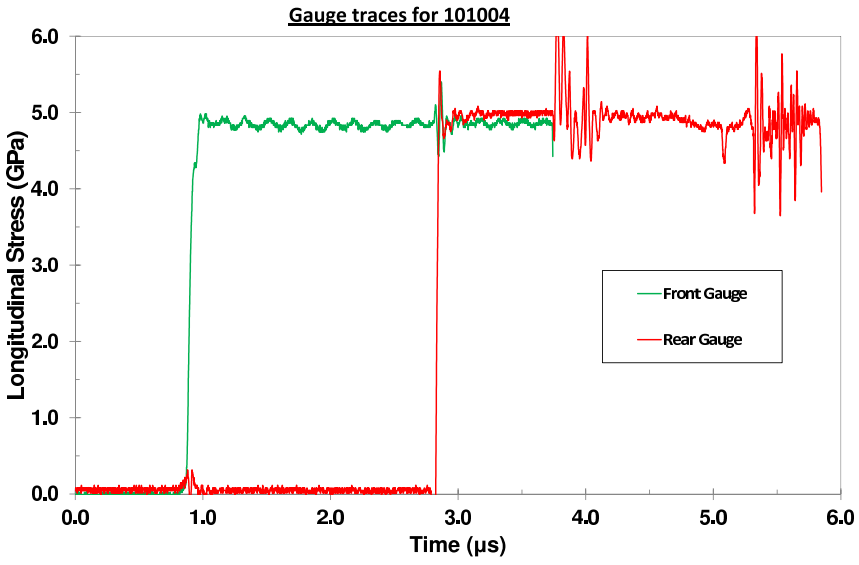

Figure 4.12: Experimental traces for shot 101004 for a 10 mm copper projectile impacting at 869 m s^{-1}.

Figure 4.13 is the Hugoniot in the U_S-u_p plane, which also includes the Hugoniot for

Experiment Number	Velocity m s^{-1}	Flyer Thickness/ Material mm	U_S mm μs^{-1}	u_p mm μs^{-1}	Volume cm^3 g^{-1}	σ_x GPa
101126	197	10 Al	3.78	0.14	0.66	0.76
101207	350	10 Al	3.81	0.25	0.64	1.38
100730A	500	10 Al	3.42	0.37	0.61	2.00
110111A	530	10 Cu	4.02	0.46	0.61	2.58
101013	679	10 Cu	4.00	0.59	0.58	3.58
101004	869	10 Cu	4.13	0.75	0.56	4.85
110111B	1000	5 Cu	4.21	0.86	0.54	6.68

Table 4.9: Longitudinal experimental results for the TWCP in the 0° orientation.

the phenolic resin Durite SC-1008. As it can be seen there is an anomalous point which is circled. This point corresponds with the matrix material, which may be coincidental in nature. The experiment that leads to this point was given the experimental code 100730A, and is shown in Figure 4.14. The trace is extremely noisy in nature, with the initial rise time of each gauge disguised by a high frequency oscillation. For this reason it has been decided that the data point will be removed, leading to the Hugoniot show in Figure 4.15.

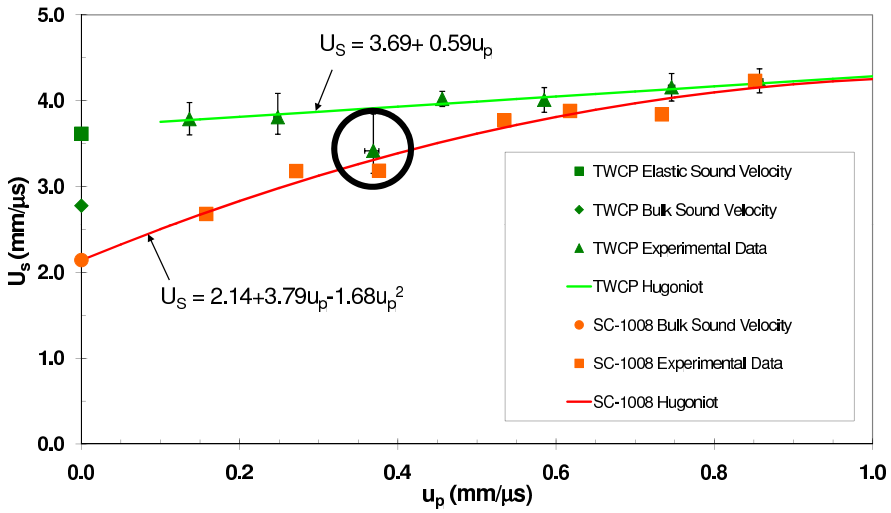

Figure 4.13: Hugoniot in the U_S-u_p plane for TWCP with the 0° lay up with an anomalous data point circled.

Figure 4.15 shows the Hugoniot in the U_S-u_p plane with the anomalous point removed. From this data set the Hugoniot in the U_S-u_p plane was found, taking the form shown in

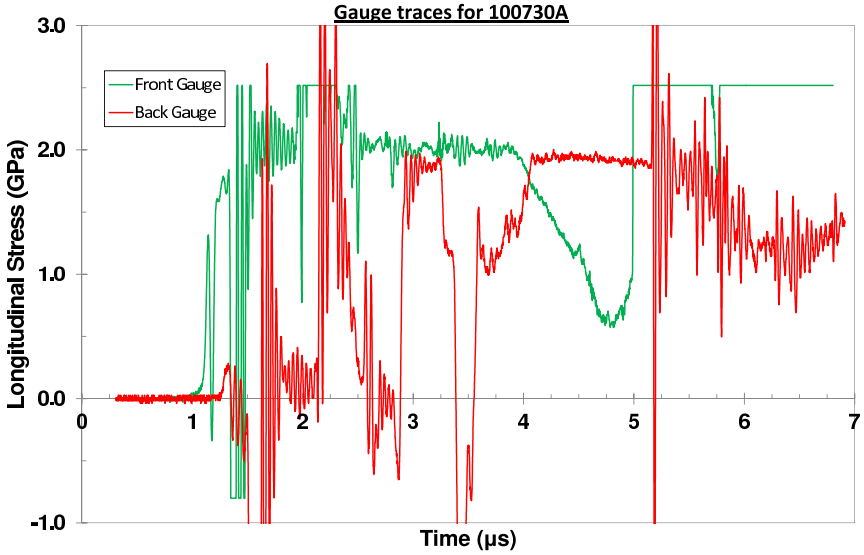

Figure 4.14: Experimental traces for experiment 100730A (see Table 4.9).

Equation 4.9. The value of c_0 matches up more closely with the c_L value, and not the c_B value from Table 4.4, which is the behaviour seen in many materials. As the value of c_0 is above that of c_L no elastic behaviour is seen in any of the traces. Above a particle velocity (u_p) value of about 0.8 mm μs^{-1} convergence between the matrix material Durite SC-1008 and the TWCP orientated at 0° is seen. However as no data exists above $u_p \sim 0.9$ mm μs^{-1} it is unclear whether this behaviour carries on at the higher particle velocities. Also included on Figure 4.15 is the Hugoniot found by Millett *et al.* [16] for a carbon fibre composite with an epoxy resin matrix. The Hugoniot for the carbon fibre epoxy composite investigated by Millett *et al.* sits below the Hugoniot found for the TWCP in the 0° weave orientation. The Hugoniot found by Millett *et al.* seems to be converging with the 0° TWCP response at a u_p of above 1 mm μs^{-1}. However due to neither data set going above a u_p value of 1 mm μs^{-1} this postulated behaviour can not be confirmed. It should also be noted that due to the constituents of the composite investigated by Millett *et al.* [16] being different to those of the composite considered here, no direct comparisons can be made.

$$U_S = 3.69 + 0.59u_p \tag{4.9}$$

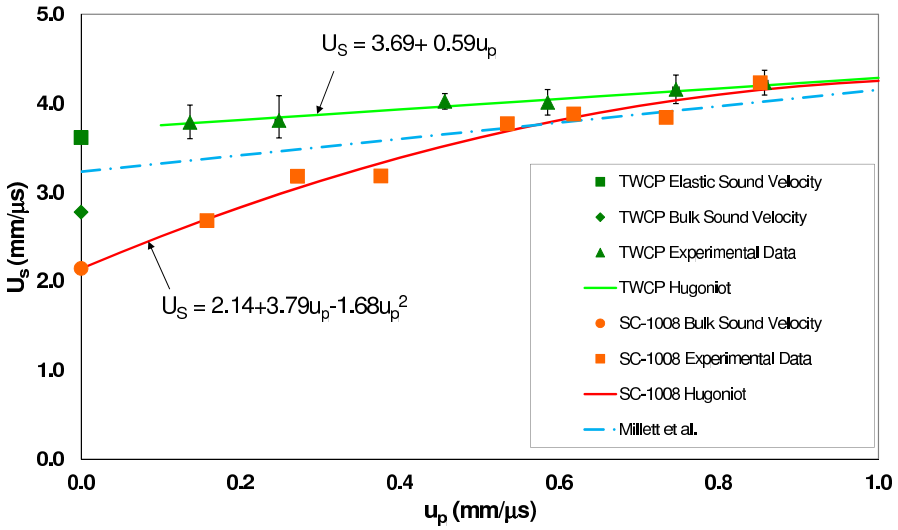

Figure 4.15: Hugoniot in the U_S-u_p plane for TWCP with the 0° lay up.

Plotting the Hugoniot in the pressure-volume plane leads to Figure 4.16; also included on this figure is the Hugoniot for the phenolic resin Durite SC-1008 as well as that for the carbon fibre epoxy composite investigated by Millett *et al.* [16]. Deviation from the Hugoniot is seen for σ_x values above 5 GPa; such behaviour has been seen in multiple materials, especially polymers such as RTM-6 [70, 71], polycarbonate [100] and the phenolic resin investigated here (Durite SC-1008). This deviation shows a strengthening effect within the shock behaviour of the material. The Hugoniot seen for the TWCP composite material in the 0° orientation is less compressible than the one seen for both the phenolic resin Durite SC-1008 and the carbon fibre composite investigated by Millett *et alii*. It is unsurprising that the TWCP composite is less compressible than the matrix material due to the fibre acting as reinforcement, increasing its overall strength. Interestingly, it seems to suggest that the Hugoniots will merge, in line with the behaviour seen in the Hugoniot in the U_S-u_p plane. Again it should be noted that the composites being compared are different, consequently not too much emphasis should be placed on these comparisons.

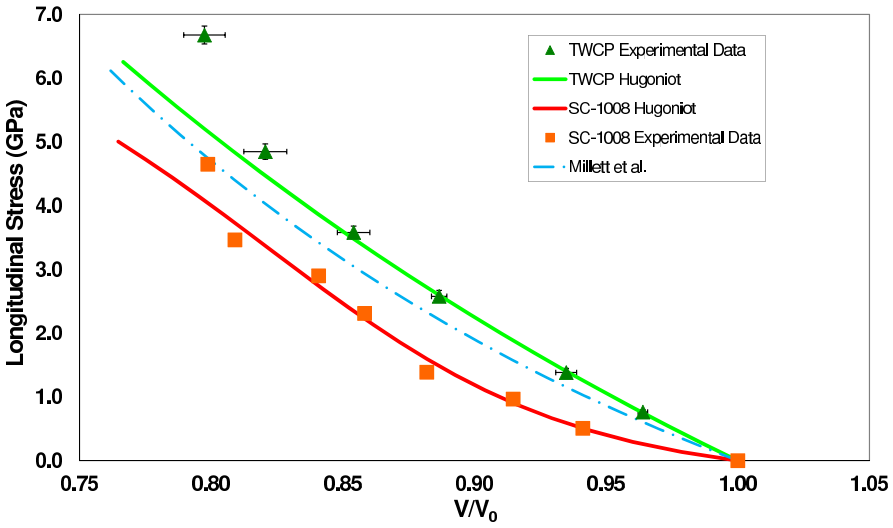

Figure 4.16: Hugoniot in the pressure-volume plane for TWCP for the 0° lay up.

4.4.2 Oscillations Within the 0° Orientation

Oscillations have been noted on many of the traces in both the longitudinal and lateral configurations. An example of these oscillations, obtained from the standard longitudinal experiments, are shown in Figure 4.12. With this trace the oscillations are seen on the front gauge only, with the rear gauge not showing this behaviour, which was noted in the composite investigated by Millett *et al.* [16]. This is most likely due to the impedance mismatch between the TWCP and the PMMA backing which results in a damping behaviour, causing the loss of oscillations on the rear gauge. These oscillations were also seen with laterally orientated gauges as shown in Figure 4.17. The lateral traces shown in Figure 4.17 show an increased rise time on the highest velocity trace. This increase in rise time implies a misalignment with the laterally orientated gauge within this experiment, however this will not greatly affect the lateral stress as reported by Appleby-Thomas *et al.* [101]. It can be seen that the traces individually have a consistent frequency which, however, increases with the shock velocity. This behaviour was also noted in the carbon fibre composite investigated by Millett *et al.*, and was attributed to interactions between the carbon fibre weave and the matrix material. This also seems to be the case for the TWCP with the 0° weave orientation. By using the simple equation

velocity equals distance over time the distance corresponding to the oscillations can be found. The time can be found from the period of the oscillations between adjacent peaks or troughs. For the velocity the corresponding experimental shock velocity is used. This then alters the equation into the one seen in Equation 4.10.

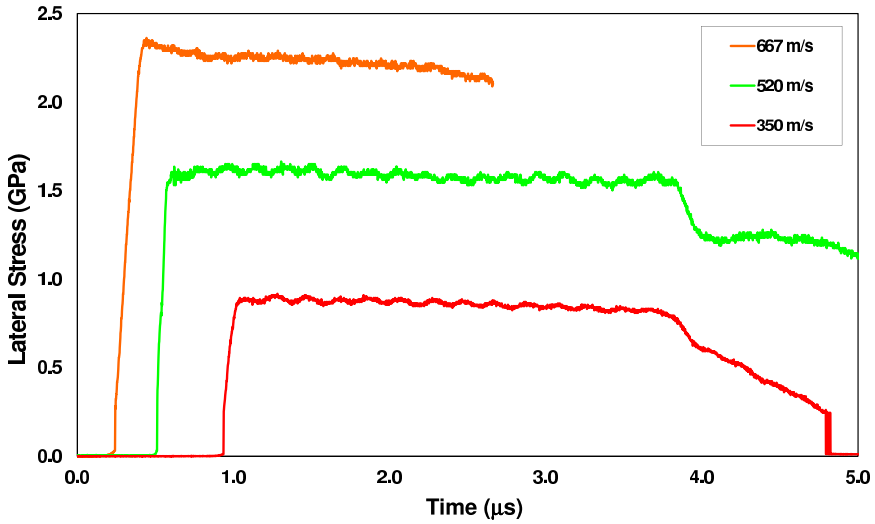

Figure 4.17: Lateral traces from the 0° orientation which include the observed oscillations.

$$x = U_S T \tag{4.10}$$

Based on the longitudinal and lateral orientated traces, Table 4.10 shows the experimental data pertaining to observed oscillations, with the shock velocity and the average period. Using this data and Equation 4.10 the distance relating to the oscillations can be ascertained. This distance was found to between 700 and 800 μm. This corresponds to approximately twice the thickness of the interlayer which was found from Figure 4.8. The oscillations appear to result from wave reverberation between composite layers. Interestingly, the oscillations seem to have no effect on the underlying shock profile as the plateau is still visible and the oscillations are only a small percentage of the overall shock pressure. Essentially, they appear to be super-imposed on top.

In conclusion the TWCP with a 0° weave orientation has a linear Hugoniot with the

Velocity m s^{-1}	U_S mm μs^{-1}	Average Period (t) μs	Distance μm	Distance/2 μm
350	3.81	0.2128	811	406
350	3.84 (Estimated)	0.2079	799	400
520	3.96 (Estimated)	0.1756	695	348
530	4.02	0.1760	708	354
870	4.16	0.1744	726	363

Table 4.10: Experimental results for the oscillations seen in the TWCP.

Equation $U_S = 3.69 + 0.59u_p$. Convergence in the U_S-u_p plane was seen between the 0° TWCP material and the phenolic resin matrix material Durite SC-1008 for $u_p \sim 0.9$ mm μs^{-1}. Deviation was also seen between the Hugoniot and the experimental data above a σ_x value of 5 GPa in the pressure-volume plane, behaviour which was attributed to material strengthening. Finally, oscillations were observed in some of the experimental traces and attributed to the interlayer interactions of the fibre weaves.

4.4.3 90° Lay up

For the 90° weave orientation a few methods for investigating the shock wave were employed. The standard Hugoniot shock experiments detailed in Section 3.1 were performed with the resultant data given in Table 4.11. This experimental set up involved using 50 μm of Mylar® for the gauge protection/insulation as shown in Figure 3.4a. A typical trace for this is shown in Figure 4.18. As it can be seen both the front and rear gauges have rapid rise times (of the order of 55 ns), with a plateau in stress seen of just under 5 GPa, before gauge failure is observed. Crosstalk can also be seen between the front and rear gauge. The lower velocity impacts tend to have a notable amount of noise associated with them as can be seen in the Appendix.

The method used by Millett *et al.* [16] and Hazell *et al.* [17] of giving the rear gauge extra protection using a *ca.* 1.6 mm piece of PMMA was also used as shown in Figure 3.5, with the results given in Table 4.12. A typical trace for this method is shown in Figure 4.19. It is important to note that the stress of the rear trace is the stress in the PMMA

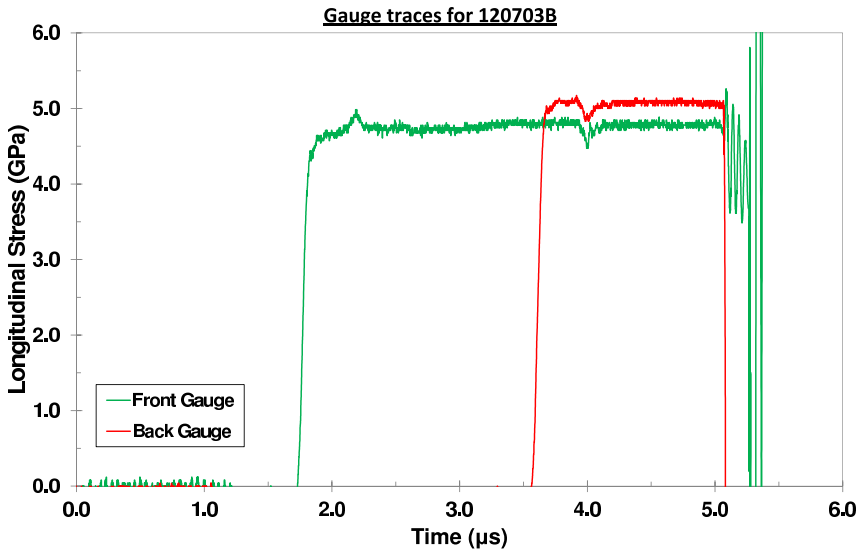

Figure 4.18: Experimental traces for shot 120703B for a 10 mm copper projectile impacting at 890 m s^{-1}.

and not the stress in the sample as the standard longitudinal traces are. Due to this fact the front gauge is the one used for calculation of σ_x. Due to the rear gauge gauge having the extra encapsulation for protection, the rear gauge tends to have a longer rise time - especially at the lower end, which can be seen with the figure presented here. Possibly caused by an elastic wave travelling ahead of the shock which will be discussed later in this section.

Finally a method of using both longitudinal and lateral gauges to gather multiple experimental values was trialled. This method used the lateral gauge as a replacement for the rear gauge in standard longitudinal experiments, and has been previously used in tungsten carbide by Appleby-Thomas *et al.* [90] and is shown schematically in Figure 3.6. This allowed values of U_S, σ_x and σ_y to be ascertained in one experiment; the corresponding/resultant data is shown in Table 4.13. A typical trace for this set up is shown in Figure 4.20. As can be seen, this method induces more noise within the traces but the data needed can still be ascertained. With the lower velocity experiments this method had quick reloading on the lateral gauges making obtaining a value of σ_y more difficult, leading to larger errors on these traces.

Experiment Number	Velocity $m\ s^{-1}$	Flyer Thickness/ Material mm	U_S $mm\ \mu s^{-1}$	u_p $mm\ \mu s^{-1}$	Volume $cm^3\ g^{-1}$	σ_x GPa
110311	353	10 Al	4.17	0.24	0.64	1.43
120702	530	10 Cu	4.15	0.45	0.61	2.73
110809	600	10 Cu	4.13	0.51	0.60	3.21
120703A	689	10 Cu	4.08	0.59	0.59	3.70
110810	834	10 Cu	4.31	0.71	0.57	4.05
120703B	890	10 Cu	4.40	0.76	0.57	4.76
120704	1016	5 Cu	4.39	0.87	0.55	5.61

Table 4.11: Experimental results for the TWCP with the cloth angled perpendicular to the shock front for the standard longitudinal experimental set up.

Experiment Number	Velocity $m\ s^{-1}$	Flyer Thickness/ Material mm	U_S $mm\ \mu s^{-1}$	u_p $mm\ \mu s^{-1}$	Volume $cm^3\ g^{-1}$	σ_x GPa
110520A	549	10 Al	3.39	0.35	0.61	2.18
110520B	580	10 Cu	3.41	0.39	0.61	3.20
110527	625	10 Cu	3.99	0.58	0.58	3.05
110317B	667	10 Cu	4.68	0.64	0.59	3.41
110324A	1000	5 Cu	4.54	1.00	0.53	5.56

Table 4.12: Experimental results for the TWCP with the cloth angled perpendicular to the shock front for the longitudinal experimental set up with a PMMA offset.

Experiment Number	Velocity $m\ s^{-1}$	Flyer Thickness/ Material mm	U_S $mm\ \mu s^{-1}$	u_p $mm\ \mu s^{-1}$	Volume $cm^3\ g^{-1}$	σ_x GPa	σ_y GPa	2τ GPa
110929A	292	5 Al	3.68	0.21	0.65	1.16	⋯	⋯
111021	312	10 Al	3.75	0.31	0.63	1.25	0.56	0.69
111010	350	10 Al	3.50	0.25	0.64	1.53	0.53	1.00
110804B	350	10 Al	4.17	0.26	0.64	1.56	0.60	0.96
110831	538	10 Al	3.70	0.39	0.61	2.30	1.19	1.10
110804A	632	10 Cu	4.21	0.46	0.61	2.81	1.82	0.99
110930	908	10 Cu	4.70	0.77	0.57	4.70	3.13	1.57

Table 4.13: Experimental results for the TWCP with the cloth angled perpendicular to the shock front for the lateral and longitudinal, and lateral only, experimental set up.

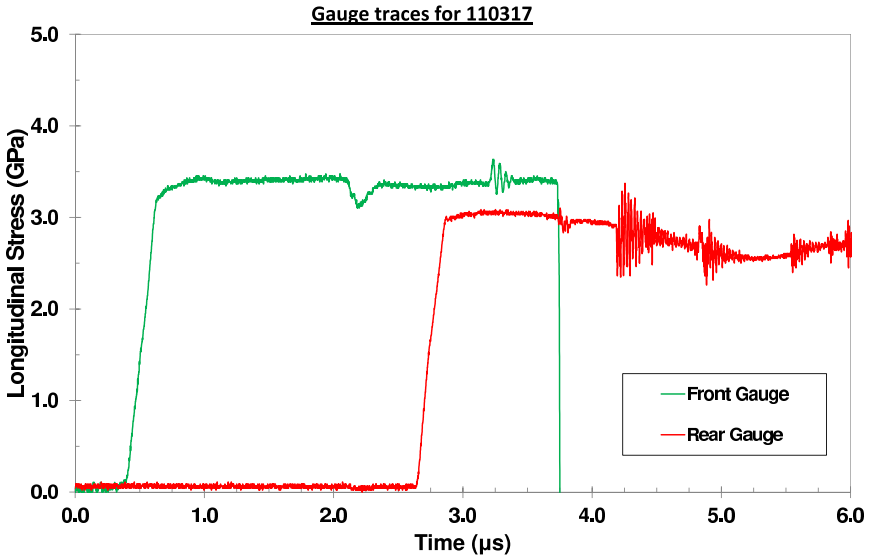

Figure 4.19: Experimental traces for shot 110317 for a 10 mm copper projectile impacting at 667 m s^{-1}.

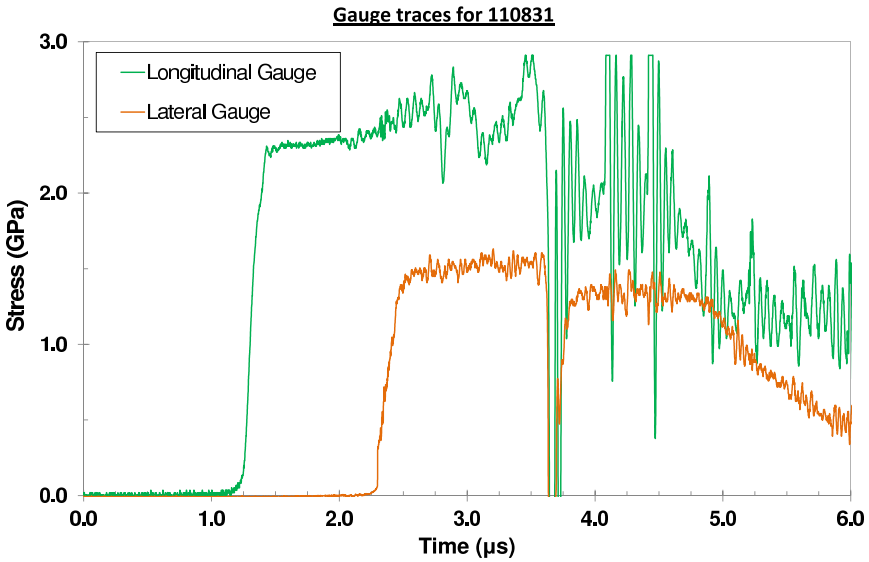

Figure 4.20: Experimental traces for shot 110831 for a 10 mm copper projectile impacting at 538 m s^{-1}.

Using this data the Hugoniot in the U_S-u_p plane is obtained as shown in Figure 4.21. As it can be seen in Figure 4.21 there is a lot of scatter in the data. By separating out the different methods patterns start to emerge. The greatest amount of scatter in all of the techniques was caused by the PMMA offset protection. This method was used to

give extra protection to the rear gauge. However looking at the traces for the standard experimental shots, this extra level of protection was not needed. The scatter seen in the PMMA offset data could be due to the high rate response of PMMA not being as well defined as it could have been; *e.g.* due to a different composition from the data in the literature. This effect was seen by Barker and Hollenbach in Reference [26], where the scatter in data was due to different manufacturing procedures. It could also be due to a longer rise in the rear gauge due to its excessive encapsulation combined with the elastic wave causing a ramp like loading, or a combination of these effects. The lateral and longitudinal data sets also have scatter in their results, but less so than when compared to PMMA offset experiments. The scatter in this data is more likely to be caused by misalignment of the gauge element. As the gauge element has a 16 mm width it is difficult to align the gauge completely flat and parallel to the front surface of the target. Also it is possible for the gauge to move slightly as noted by Appleby-Thomas [101]; this means that the measured distance between the gauge elements may have changed due to the glue interlayer. Another possible cause for the scatter in the data arises due to the physical size of the gauge itself. The active element of the gauge is smaller than each fibre cloth, however as the fibres are perpendicular this should not make a difference to shock traces. The least amount of scatter in the data was given by the standard experimental technique of two gauges protected with only Mylar®. Using these standard traces a linear Hugoniot was found as shown in Equation 4.11. Also included on the Hugoniot in the U_S-u_p plane are the Hugoniots obtained for the phenolic resin Durite SC-1008 and the 0° TWCP weave orientation. At the higher particle velocities all of the Hugoniots appear to converge, however as noted previously insufficient data exists to confirm this trend for u_p of ~ 0.9 mm μs^{-1}. Interestingly, such behaviour was noted by Willows *et al.* [18], who observed that orientation becomes unimportant above a u_p value of approximately 1 mm μs^{-1}.

$$U_S = 3.96 + 0.46u_p \tag{4.11}$$

Reducing this U_S-u_p Hugoniot down to the standard two longitudinally orientated

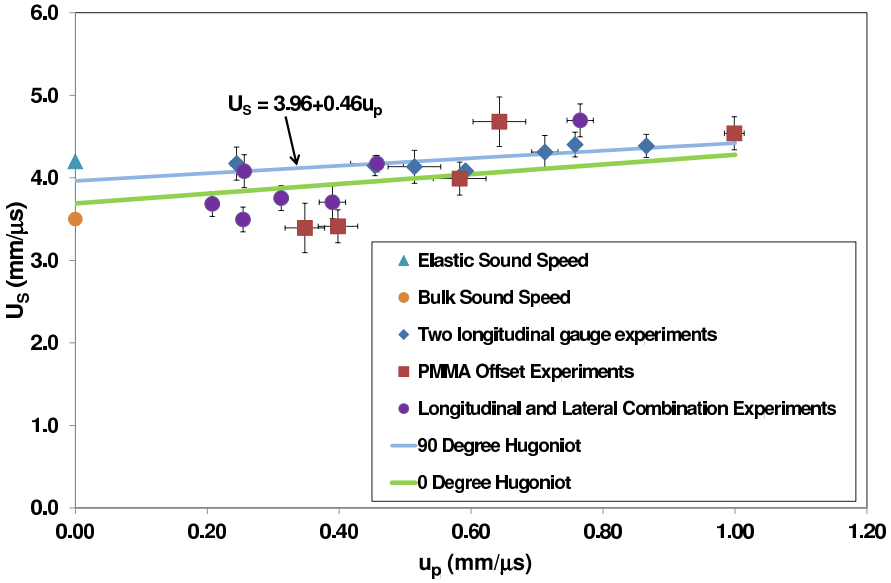

Figure 4.21: Hugoniot in the U_S-u_p plane for TWCP with the 90° lay up for all of the experimental methods.

manganin pressure gauges, as well as including the data collected by Hazell *et al.* [17], Figure 4.22 was obtained. For the TWCP with the 90° fibre weave orientation the Hugoniot is nearly flat in nature. This is due to the elastic sound velocity having a value of 4.2 mm μs^{-1}. From both Figure 4.22 and Table 4.11 it can be seen that the lowest four u_p data points are elastic in nature with the values of U_S being approximately that of c_L. This behaviour carries on until a u_p value of 0.6 mm μs^{-1}, where above this value it deviates from the value of c_L. The Hugoniot from the carbon fibre composite investigated by Hazell *et al.* has a considerably steeper slope than the 90° TWCP Hugoniot, with the intersection occurring at a u_p value of about 0.9 mm μs^{-1}. It is also interesting to note that a slight amount of scatter is seen on the data by Hazell *et al.*, possibly due to the low number of experiments, over a limited range; or it also a possibility that the nature of the weave leads to this scatter. Scatter was also seen in the Millett *et al.* data [16] which has not been included here due to no corresponding Hugoniot equation being given. This scatter seems to be a consistent artifact of this orientation of carbon fibre composites. Also seen in the composite investigated by Millett *et al.* was convergence between the perpendicular fibre weave orientation, which is behaviour seen in the TWCP composite

here, lending credence to the fact that above a u_p value of 1 mm μs^{-1} orientation is unimportant.

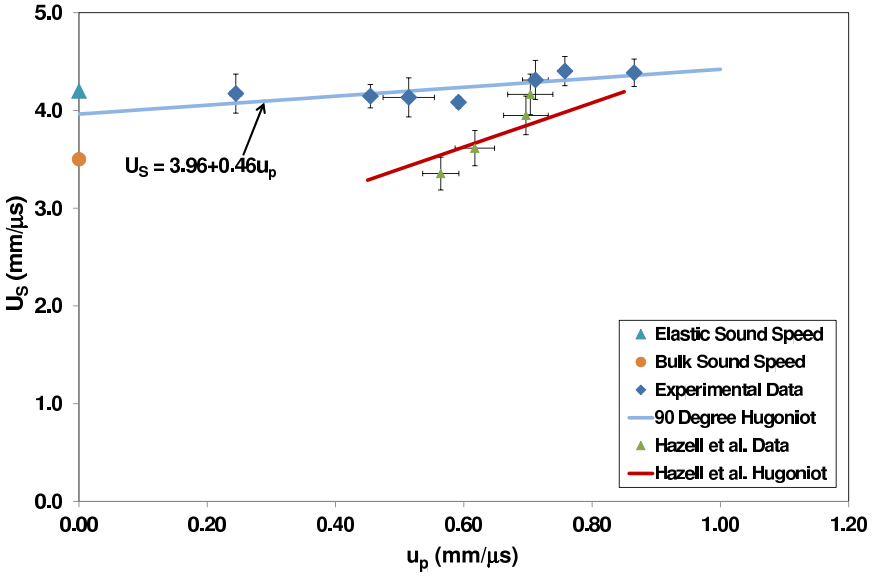

Figure 4.22: Hugoniot in the U_S-u_p plane for TWCP with the 90° lay up for the reduced experimental data.

By plotting data derived from all of the experimental techniques as well as the Hugoniot for the 0° and 90° in the pressure-volume plane, Figure 4.23 is obtained. The Hugoniot for 90° weave orientation was obtained from the reduced data shown in Figure 4.22. As with the Hugoniot in the U_S-u_p plane, scatter is seen between the different experimental techniques. Convergence between orientations is seen as well in the pressure-volume plane, where convergence will occur at about 7 GPa. The Hugoniot for the 90° is less compressible than the 0° orientation. This is expected due to the orientations of the fibres leading to increased stiffness in the direction of the applied shock wave.

By reducing the data down to the standard two manganin gauge set up Figure 4.24 is obtained. As seen with the U_S-u_p reduced data the experimental data sits close to or on the Hugoniot curve. No deviation is seen between the Hugoniot and the experimental data meaning there is no strengthening as was tentatively noted in the 0° orientation. The Hugoniot obtained by Hazell *et al.* for their investigated carbon fibre composite is also

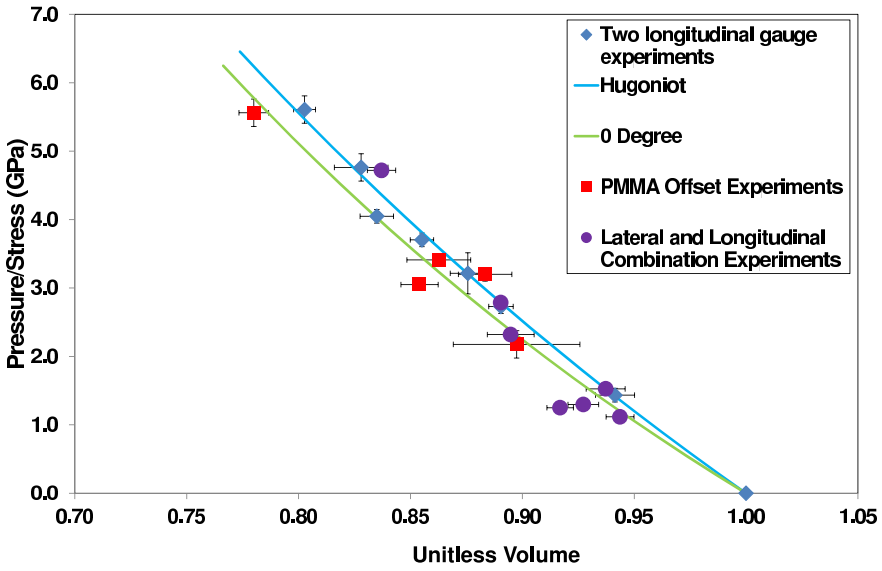

Figure 4.23: Hugoniot in the pressure-volume plane for TWCP with the 90° lay up for all of the experimental methods.

included in Figure 4.24 [17]. The individual data points are not shown on this figure due to them not being included in the corresponding paper. Convergence between the TWCP and the composite investigated by Hazell *et al.* occurs at approximately 6 GPa, before which the TWCP is less compressible than the other carbon fibre composite.

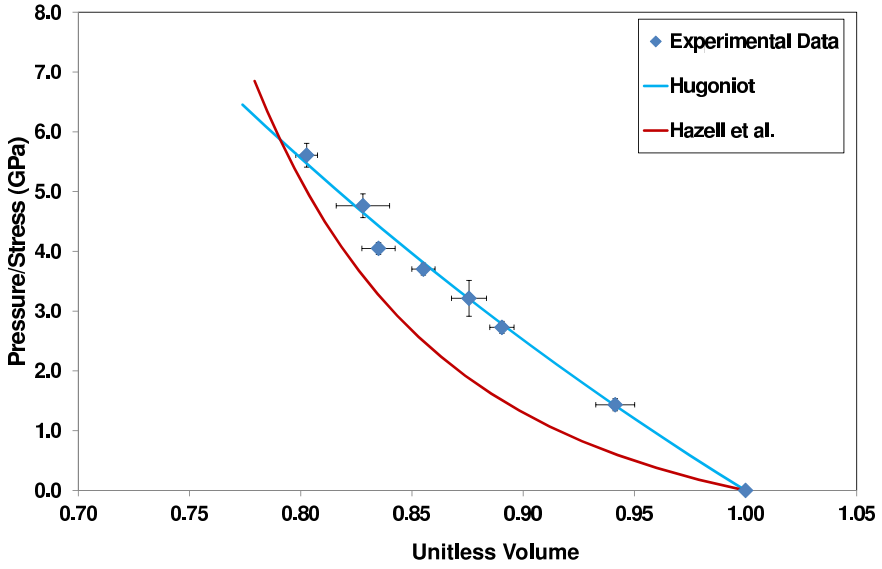

Figure 4.24: Hugoniot in the pressure-volume plane for TWCP with the 90° lay up for reduced experimental data.

Observation of the experimental traces shows a potential elastic precursor as was seen in other composite materials such as Dyneema® [58], glass fibre composites [14], aramid fibre composites [20] and carbon fibre composites [16, 17]. However unlike the results found by Millett *et al.* [16] and Hazell *et al.* [17] the elastic precursor here decreases in amplitude as the longitudinal stress increases. This behaviour can be seen in the experimental traces shown in Figures 4.25, 4.26 and 4.27. For Figures 4.25 and 4.26 the precursors seen are nearly identical in nature with a peak stress amplitude of approximately 0.15 GPa before a decrease in stress before the main shock front catches up. This decrease in stress before the main shock has been seen in a magnesium alloy Electron 675, where it was thought to be due to a capacitance effect of the gauges [102]. Also noted on the gauge traces was crosstalk between the gauges, with a reloading effect seen on the front gauge as the precursor is seen on the rear gauge.

It has been proposed that this precursor is due to an elastic wave travelling down the fibre. Millett *et al.* found a value of approximately 7 mm μs^{-1} for this elastic wave [16], with the value found by Hazell *et al.* being about 6.2 mm μs^{-1} [17]. The value found for the TWCP material investigated here is shown in Table 4.14 with Δt being the time from the shock seen on the front gauge until the start of the elastic precursor on the rear gauge. Using this value the elastic speed was calculated, and it can be seen that this elastic velocity decreases as the shock velocity was increased. As it was suggested this value was due to the elastic sound speed value of the fibres, Equation 4.12 could be used to estimate what value should be expected for the composite, for comparative purposes. In Equation 4.12 superscript C stand for the composite as a whole, F for the fibres and M for the matrix. The values of 0.54 and 0.46 relate to the volume fraction of the composite with respect to the fibres and matrix respectively. Applying Equation 4.12 with values for c_L^F found from the elastic precursor seen in Figures 4.25, 4.26 and 4.27 (given in Table 4.14) and the value of c_L^M obtained from Table 4.1, a value of c_L^C can be obtained. This value is shown in Table 4.14. For the experiments 120702 and 110809 values of c_L^C of 3.87 and 3.84 mm μs^{-1} were obtained. These values sits between both the 0° and 90°

Experiment Number	Impact Velocity m s^{-1}	Flyer Thickness/ Material mm	Δx mm	Δt μs	U_S^F/c_L^F mm μs^{-1}	c_L^C mm μs^{-1}
120702	530	10 Cu	8.00	1.27	6.30	3.87
110809	600	10 Cu	8.00	1.31	6.12	3.84
120703A	690	10 Cu	7.98	1.66	4.80	3.51

Table 4.14: Experimental results with potential elastic precursor and potential fibre elastic velocities.

elastic sound speed values obtained from the ultrasonic measurement technique (Table 4.4). This is perhaps not surprising as ultrasonic measurement techniques tend to smear individual wave components (*e.g.* c_L^F and c_L^M) out.

$$\frac{1}{c_L^C} = \frac{0.54}{c_L^F} + \frac{0.46}{c_L^M} \tag{4.12}$$

Figure 4.28 shows a comparable shot (copper projectile impacting at 625 m s^{-1}) which has no elastic precursor. The difference with this shot compared to shots detailed here was the use of PMMA to protect the rear gauge. Clearly this extra protection damped out the elastic precursor so that it was not observed by the rear gauge. The decrease in precursor demonstrates the complexity of composite systems and the importance of impact conditions.

In the experiments without the PMMA offset, the elastic precursor is being overdriven by the main shock front at the higher velocities hence its disappearance. This would generally be expected, as at higher velocities when the orientation is unimportant as discussed by Willows *et al.* [18]. For this given material and orientation it is interesting to note that this precursor decreases in value until it disappears at a u_p value of approximately 0.6 mm μs^{-1}. This value is approximately where the U_S-u_p Hugoniot alters from being elastic in nature to plastic.

In summary, a linear Hugoniot with the equation of $U_S = 3.69 + 0.46u_p$ was found for the 90° weave orientation. Up until a u_p value of 0.6 mm μs^{-1} the behaviour of the TWCP was elastic in nature. Convergence between the 90° and 0° was seen between the

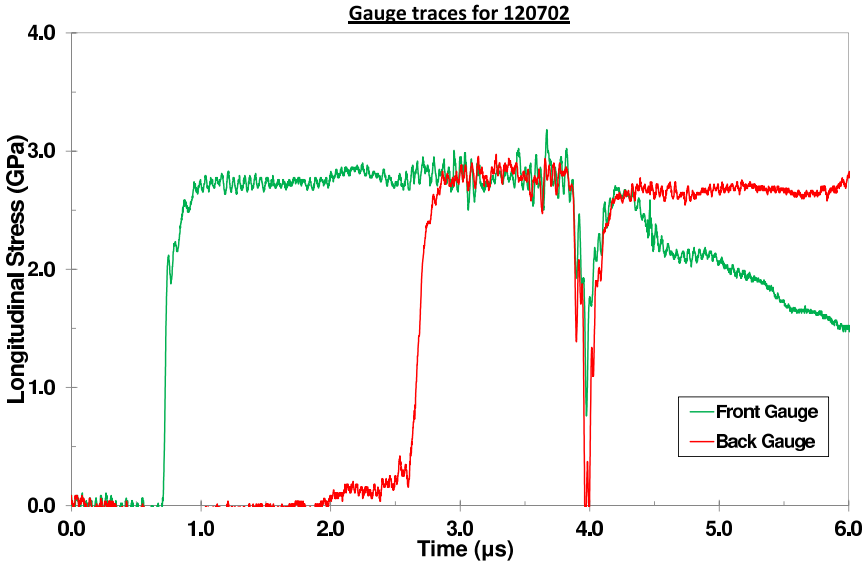

Figure 4.25: Experimental traces for shot 120702 showing precursor behaviour for a copper projectile impacting at 530 m s^{-1}.

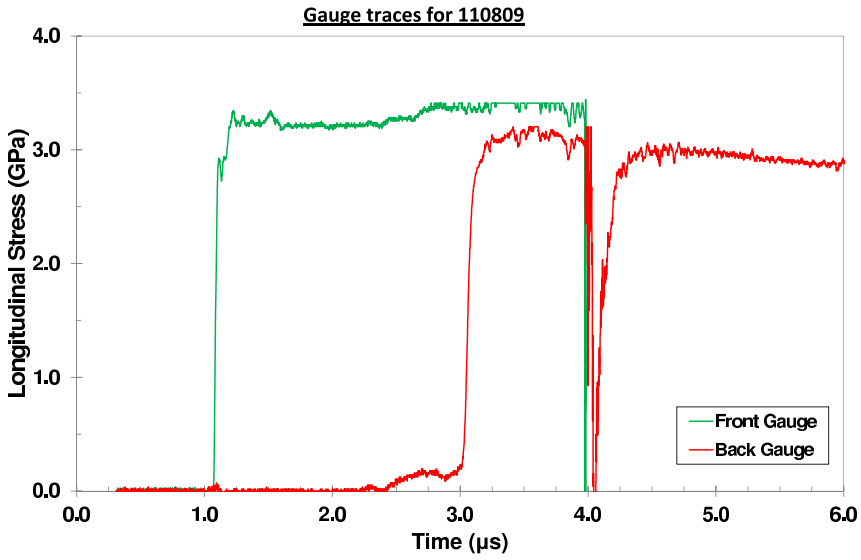

Figure 4.26: Experimental traces for shot 110809 showing precursor behaviour for a copper projectile impacting at 600 m s^{-1}.

Hugoniots at higher u_p values. Scatter was noted among the experimental data and found to be due to the experimental technique. No deviation was seen from the Hugoniot in the pressure-volume plane meaning no strengthening of the material as was seen with the 0° weave orientation results.

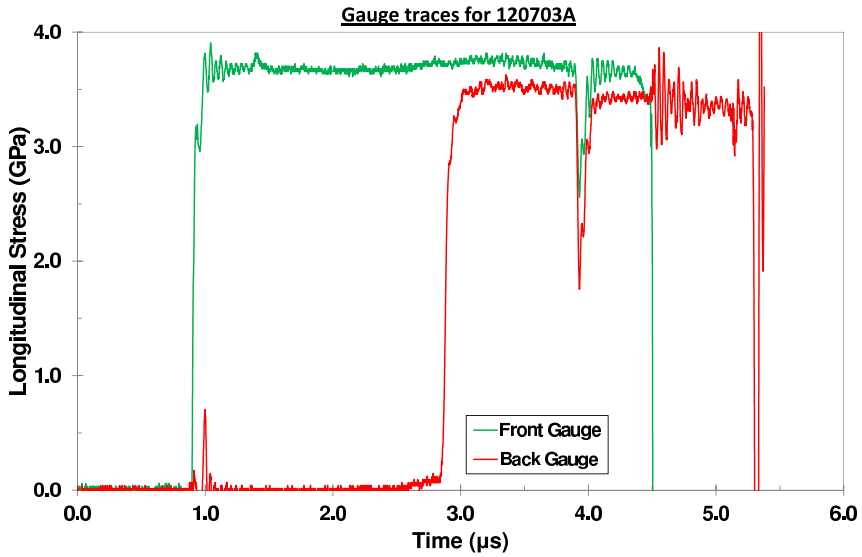

Figure 4.27: Experimental traces for shot 120703A showing precursor behaviour for a copper projectile impacting at 689 m s^{-1}.

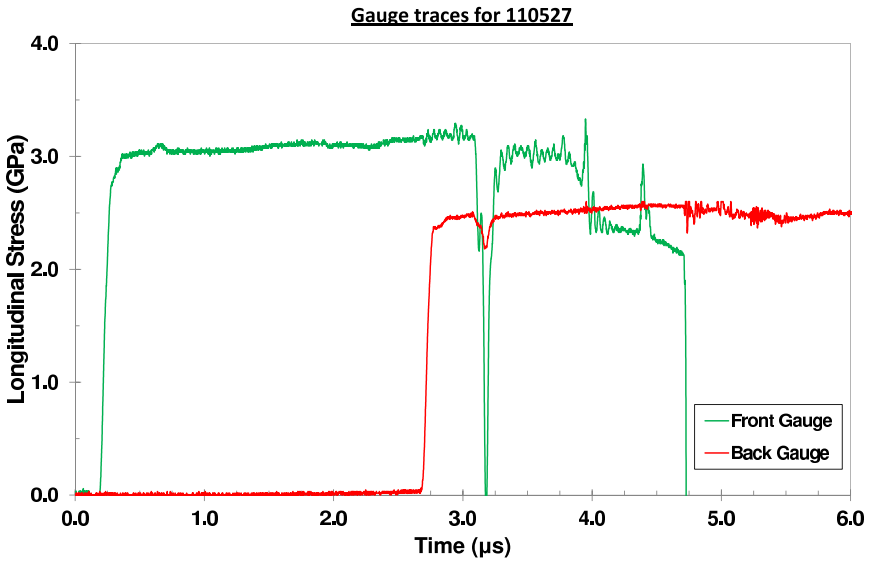

Figure 4.28: Experimental traces for shot 110527 showing no precursor behaviour for a copper projectile impacting at 625 m s^{-1}.

4.4.4 25° Lay up

Table 4.15 shows the experimental data obtained for the 25° weave angle. This data includes a mixture of data obtained via the standard experimental technique (two longitudinal gauges) and the longitudinal and lateral gauge combination, as shown in

Figures 3.4a and 3.6 respectively. A representative standard longitudinal traces is shown in Figure 4.29. This traces starts with rapid rise times on both the front and rear gauge until about 2 GPa where the rise becomes slower and in the case of the rear gauge curved in nature. The plateaus of both gauges show an amount of noise, although this is minimal. A typical pair of traces for the longitudinal and lateral combined experiment is shown in Figure 4.30. It can be seen that the rise time on the longitudinal gauge is less than the rise time on the lateral gauge which is expected due to the respective geometries of each gauge. Less noise is seen on the longitudinal gauge than was seen in Figure 4.29, more than likely due to the higher stress imparted into the TWCP sample. Very slight oscillations can be seen on the lateral gauge trace, potentially due to the fibre weave as was seen with the 0° orientation. This is the only trace at this orientation to show this behaviour, although it would be reasonable to expect this behaviour to be damped out at off-axis orientations.

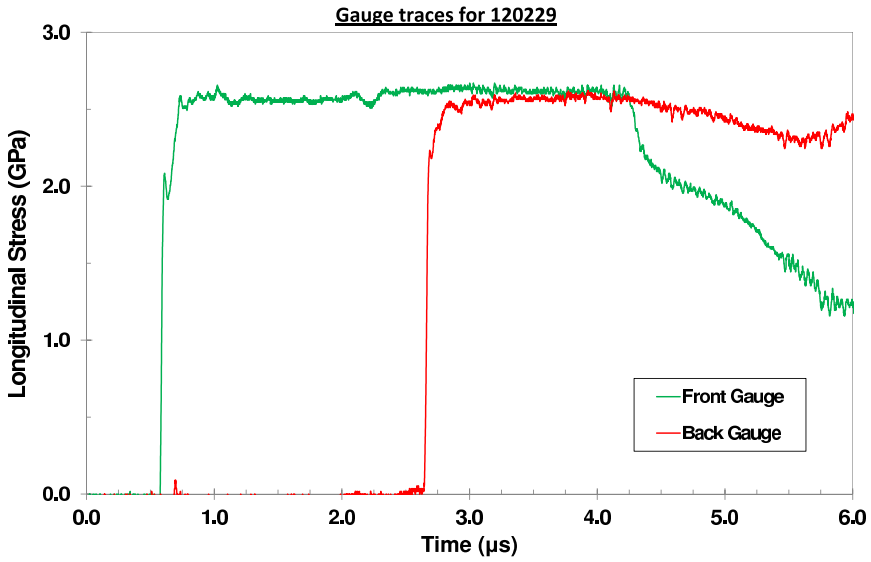

Figure 4.29: Experimental traces for shot 120229 for a 10 mm copper projectile impacting at 508 m s^{-1}.

Using the data from Table 4.15, Figure 4.31 is obtained for the Hugoniot in the U_S-u_p plane. Also included in this figure is the Hugoniot obtained for the 0° TWCP, as well as the Hugoniot found by Burrell *et al.* for a TWCP orientated at 20° [19]. There is a

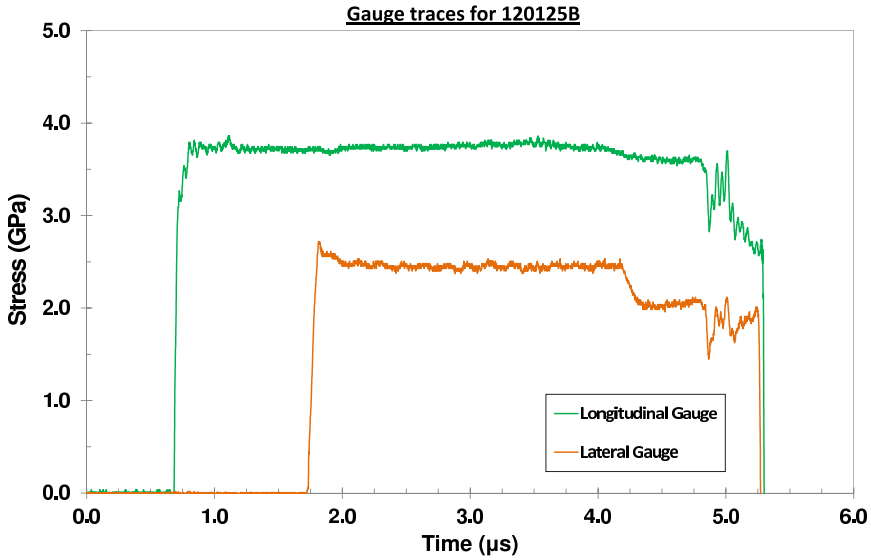

Figure 4.30: Experimental traces for shot 120125B for a 10 mm copper projectile impacting at 691 m s^{-1}.

notable degree of scatter apparent in the data for the TWCP material, a response which can also be seen in the experimental data gathered by Burrell *et al.*; however the data does not contain as much scatter as was seen with the 90° TWCP data as seen in Figure 4.21. The scatter in this case is most likely due to using both longitudinal and lateral gauges in the same sample, which as discussed previously will lead to a greater error in the known distance between the gauges. It is interesting to note that 6 out of 10 data points (60%) agree with the Hugoniot found for the 0° orientated TWCP, meaning that if the scatter is caused by the experimental method and not the material, that at least for the 0° and 25° arrangements, orientation is unimportant in the shock response. For reference however, the line of best fit for the 25° material, is given by Equation 4.13. Again as seen with the 90° TWCP Hugoniot (Figure 4.21) convergence occurs at the higher u_p values as seen in Figure 4.31. The Hugoniot ascertained by Burrell *et al.* also converges with the 25° data, at an approximate u_p value of 1 mm μs^{-1}. Interestingly, it would have been expected that a difference in the weave orientation of 5° would not result in a difference in the observed Hugoniots, but one is seen here. This may be due to a change in the makeup of the composite, either in terms of the type/ratio of constituents employed or in the amounts

Experiment Number	Velocity m s^{-1}	Flyer Thickness/ Material mm	U_S mm μs^{-1}	u_p mm μs^{-1}	Volume cm^3 g^{-1}	σ_x GPa	σ_y GPa	2τ GPa
120308	330	10 Al	3.80	0.23	0.64	1.30	···	···
120619A	349	10 Al	3.86	0.25	0.64	1.51		
120125A	397	10 Al	3.54	0.29	0.63	1.62	0.72	0.90
120116A	437	10 Al	3.54	0.32	0.62	1.78	0.77	1.01
120229	508	10 Cu	3.89	0.44	0.61	2.60	···	···
120209A	534	10 Al	3.48	0.39	0.61	2.21	1.09	1.11
120210A	600	10 Cu	3.93	0.52	0.59	3.08	1.71	1.38
120125B	691	10 Cu	3.88	0.60	0.58	3.74	2.11	1.63
120116B	822	10 Cu	3.74	0.71	0.55	4.36	2.75	1.61
120301	1155	5 Cu	4.34	0.99	0.53	6.89	···	···

Table 4.15: Experimental results for the TWCP with the cloth angled 25° to the shock front.

employed (*e.g.* changes in the volume fraction).

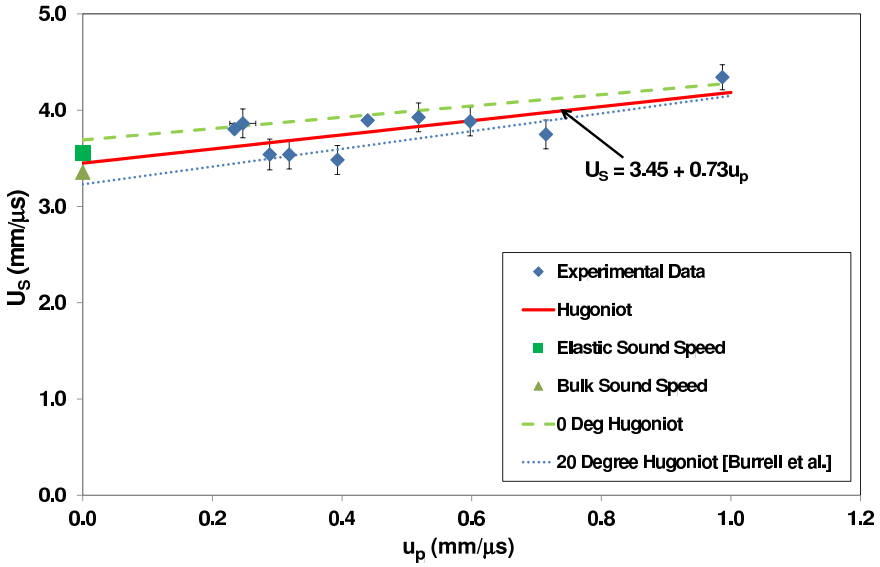

Figure 4.31: Hugoniot in the U_S-u_p plane for TWCP with the 25° lay up for all of the experimental methods.

$$U_S = 3.45 + 0.73u_p \tag{4.13}$$

Plotting the data in the pressure-volume plane Figure 4.32 is obtained. Also included on this figure is the Hugoniot found by Burrell *et al.* as well as the Hugoniot found for

the 0° TWCP. Scatter can be seen in the pressure-volume plane, as was seen in the U_S-u_p plane. Similar to what was seen in the U_S-u_p plane 7 out of 10 data points (70% of the data) agree with the Hugoniot found for the 0° orientation. The Hugoniot obtained is slightly more compressible than the one obtained for the 0° TWCP. Here deviation from the 25° material was seen between the Hugoniot and the experimental data points at a σ_x value of 7 GPa, in line with deviation seen between the experimental data points and the Hugoniot for the 0° orientated TWCP as seen in Figure 4.16.

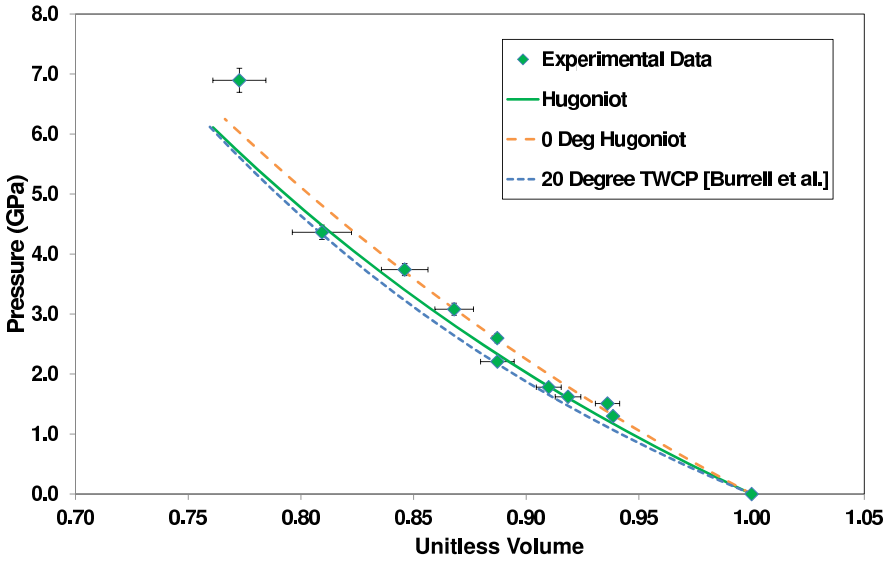

Figure 4.32: Hugoniot in the pressure-volume plane for TWCP with the 25° lay up for all of the experimental methods.

In summary, a linear Hugoniot for the TWCP material with a 25° orientation was found, which was comparable in nature to the Hugoniot found for the 0°. The equation found for the 25° lay up was $U_S = 3.45 + 0.73u_p$. A degree of scatter was seen in the data, however the majority of data agreed well with the Hugoniot obtained for the 0° orientation. When compared to the data obtained by Burrell *et al.* [19] deviation was seen, but convergence did occur at a u_p value of approximately 1 mm μs^{-1}. This difference implies a change in the make up of the composite, as a 5° orientation change should not cause this change. In the pressure-volume plane very little difference was noted between the investigated 25° and 0° lay ups as well as the 20° investigated by Burrell *et alii*. Again

the majority of data for the 25° orientation (70%) agreed with the 0° Hugoniot. Deviation was also observed at elevated pressure as was seen with the 0° weave angle data in the pressure-volume plane.

4.4.5 45° Lay up

Table 4.16 shows the experimental data gathered for the TWCP with a weave angle of 45°. This data includes a mixture of data from the standard experimental technique (two longitudinal gauges) and the longitudinal and lateral gauge combination (as shown in Figures 3.4a and 3.6 respectively). Typical experimental traces are shown in Figures 4.33 and 4.34 for the standard longitudinal experimental set up and for the longitudinal and lateral gauges combined respectively. The standard longitudinal experimental traces shown in Figure 4.33 exhibit the usual rapid rise of the gauges with a sight amount of noise at the initial part of the plateau. The rest of the traces have very little noise except for where cross-talk between the gauges occur. For the combined longitudinal and lateral experiential traces shown in Figure 4.34 the behaviour exhibited is similar to the standard longitudinal traces. A large overshoot can be seen on the lateral gauge trace which has been seen on other lateral gauge traces.

The experimental data from Table 4.16 is plotted in the U_S-u_p plane in Figure 4.35. More scatter is present on this data than on the 25° results, but less than found on the 90° data. This suggests that the scatter seen is directly related to the angle of the weave, *i.e.* as the angle increases so does the scatter. Two of the data points sit lower than the rest and match up with the resin Hugoniot, with one point sitting higher than expected. These three data points are from the experimental technique of a longitudinal front gauge coupled with a laterally orientated "rear" gauge. It should be noted however that two of these longitudinal and lateral experiments match nearly perfectly with the standard two longitudinal gauge experiments. This implies that the technique of the longitudinal and lateral gauge method is useful, if care is taken when it is employed. This means that target preparation is extremely important for this technique, especially due to the size of

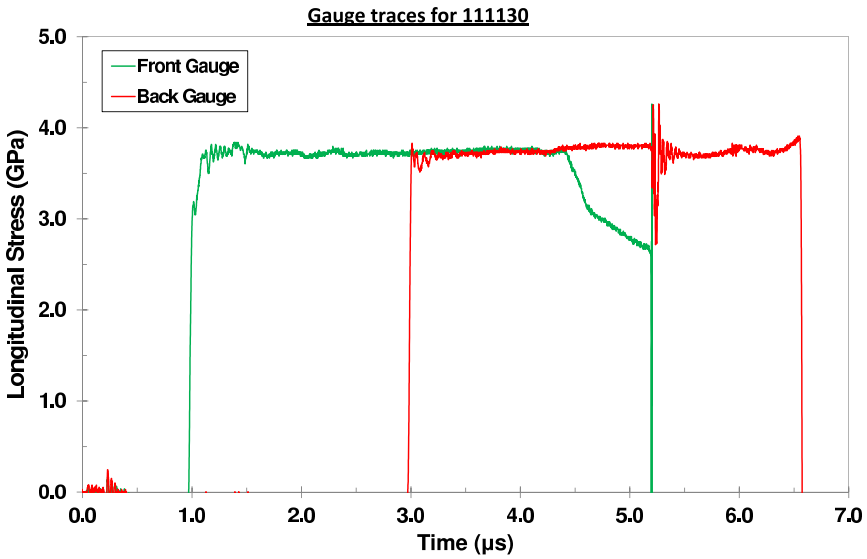

Figure 4.33: Experimental traces for shot 111130 showing precursor behaviour for copper projectile impacting at 679 m s^{-1}.

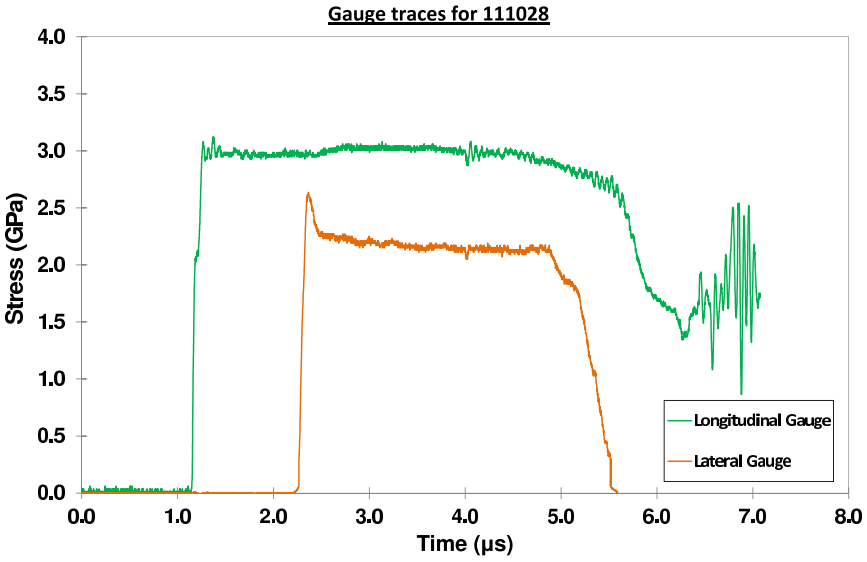

Figure 4.34: Experimental traces for shot 111028 showing precursor behaviour for copper projectile impacting at 579 m s^{-1}.

the laterally orientated gauge. This is evident from experiment 111118B which is shown in Figure 4.36. While the rear lateral trace is of very good quality, an anomaly occurred on the front gauge. This premature gauge failure is what has caused the excessively large error bars for this experimental data point.

Experiment Number	Velocity m s^{-1}	Flyer Thickness/ Material mm	U_S mm μs^{-1}	u_p mm μs^{-1}	Volume cm^3 g^{-1}	σ_x GPa	σ_y GPa	2τ GPa
120427	350	10 Al	3.87	0.25	0.64	1.4	···	···
111031	351	10 Al	3.03	0.26	0.63	1.41	0.74	0.67
111122	538	10 Al	3.78	0.39	0.61	2.11	1.25	0.86
120418	548	10 Al	3.82	0.39	0.61	2.17	···	
111028	579	10 Cu	3.43	0.51	0.58	2.97	1.92	1.05
120510	676	10 Cu	4.03	0.58	0.59	3.42	2.06	1.36
111130	697	10 Cu	4.04	0.60	0.58	3.73	···	···
111118B	824	10 Cu	4.75	0.69	0.59	4.81 Est.	2.81	2.00
120419	839	10 Cu	4.34	0.72	0.57	4.51	···	···
111206	983	5 Cu	4.41	0.84	0.56	05.51	···	···

Table 4.16: Experimental results for the TWCP with the cloth angled 45° to the shock front.

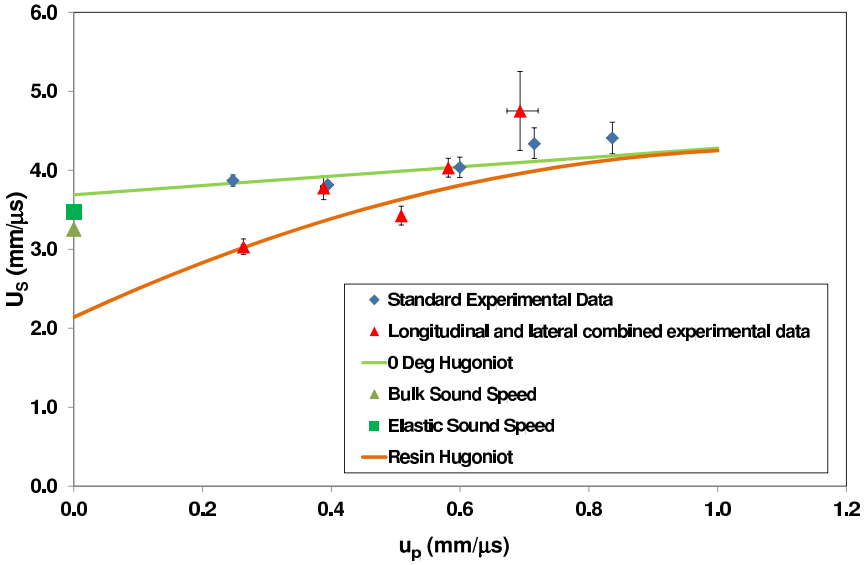

Figure 4.35: Hugoniot in the U_S-u_p plane for TWCP with the 45° lay up for all of the experimental methods.

Removing the Hugoniot for the phenolic resin, as well as the anomalous data points, we obtain Figure 4.37. With this reduced equation of state, 5 of the 7 data points agree with the Hugoniot obtained for the 0° lay up. Further, the highest two data points when combined with the error bars nearly match up with the Hugoniot for the 0° orientation. This behaviour corresponds to what was seen with the 25° TWCP orientation. A least

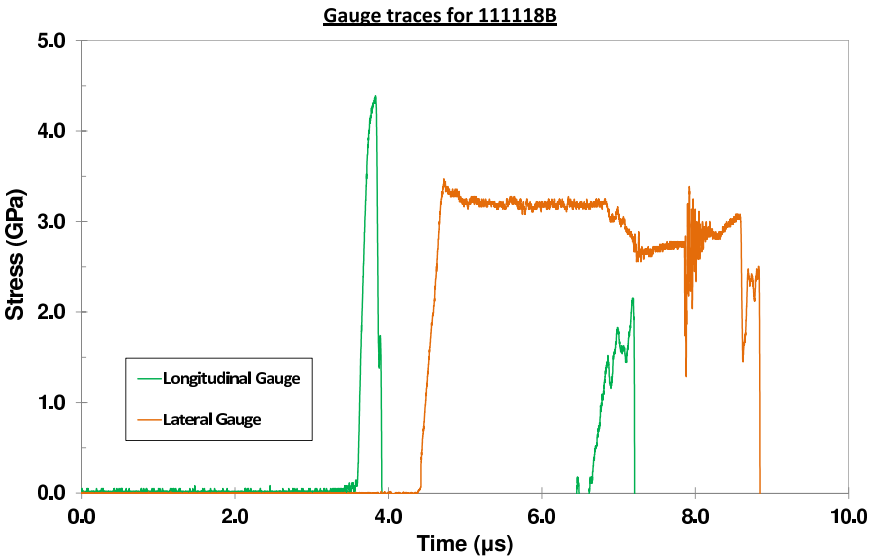

Figure 4.36: Traces for the experiment 111118B (see Table 4.16).

square fit applied to the reduced data provides Equation 4.14. Again this is linear in nature with a higher value of S than seen with the other orientations. As S is related to the first pressure derivative of bulk modulus, this would imply a less compressible material than the other fibre weaves. The intercept c_0 matches closely to the value obtained using ultrasonic techniques of c_L. Usually the value of c_0 would match up with c_B, but for this material due to the low c_S value c_B and c_L have similar values.

$$U_S = 3.44 + 1.12u_p \tag{4.14}$$

Figure 4.38 shows the Hugoniot in the pressure-volume plane for the reduced data set for the 45° weave orientation. Interestingly, no deviation is seen between the experimental data and the Hugoniot. Deviation is seen between the Hugoniot of 0° and 45° arrangements at the higher pressures, and correspondingly deviation is seen between the experimental data and the 0° TWCP Hugoniot. As implied by the higher value of S there is less compressibility in the pressure-volume plane for the 45° lay up as compared to the 0° orientation.

In summary, again a linear Hugoniot in the U_S-u_p plane was found, with the equation

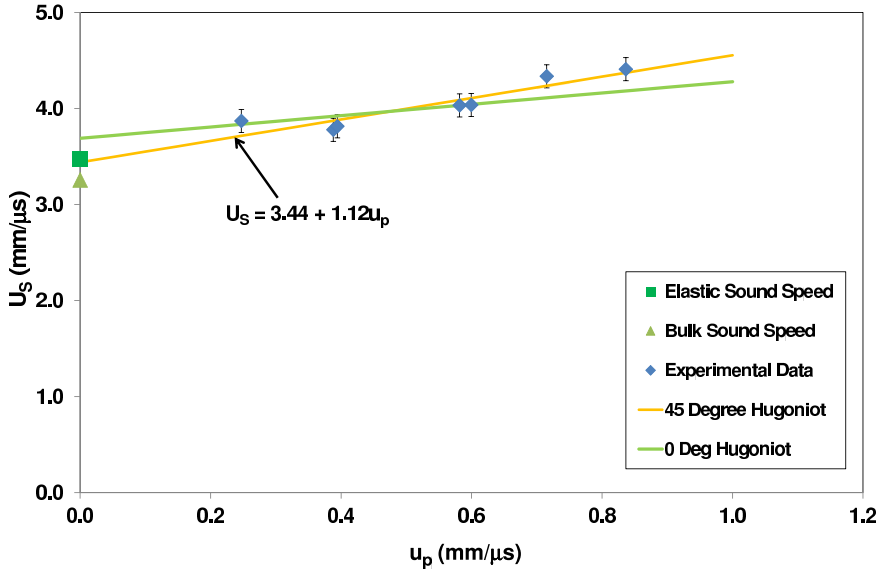

Figure 4.37: Hugoniot in the U_S-u_p plane for TWCP with the 45° lay up for all of the reduced experimental data.

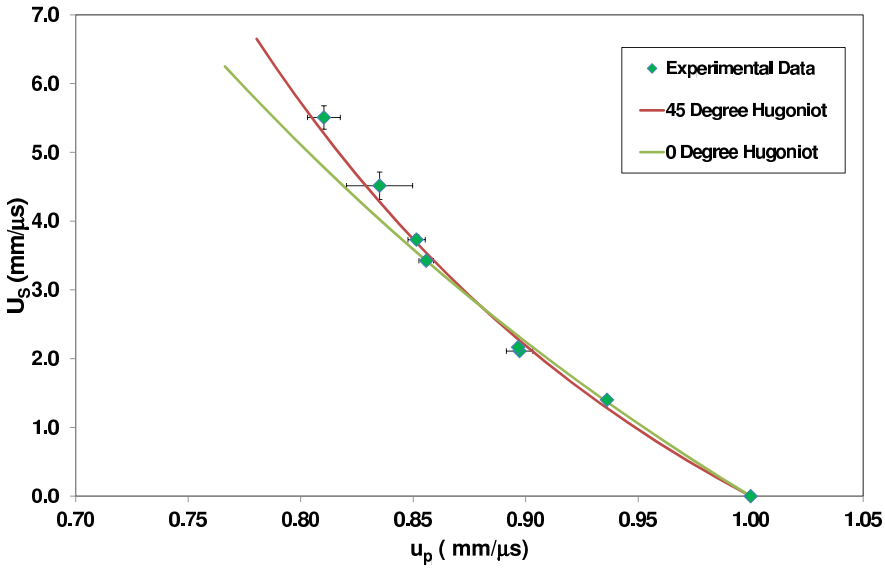

Figure 4.38: Hugoniot in the pressure-volume plane for TWCP with the 45° lay up for all of the reduced experimental data.

given by $U_S = 3.44 + 1.12u_p$. The majority of the data points agreed with the Hugoniot that was ascertained for the 0° orientated TWCP samples. Further, no deviation was seen between the experimental data and the Hugoniot in the pressure-volume plane; though the compressibility of the 45° orientation compared to the 0° lay up.

4.5 The effect on the shock traces with respect to orientation

It would be reasonable to assume that the change in orientation of the carbon fibre weave would lead to an alteration in the shock traces. To investigate whether this was the case four comparable experiments were compared to one another. All these experiments were performed with a 10 mm copper flyer traveling at velocities between 820 and 890 m s^{-1}. Figure 4.39 is the 0° orientation data, Figure 4.40 is the 90° orientation, Figure 4.41 is the 25° orientation and Figure 4.42 is the 45° result. The first item to note is the rise time of the gauge with respect to angle. The 0° orientation traces have the lowest rise time followed by the 90°, with the intermediate angles having longer rise times. This implies that orientation does have some effect on the shock response seen, with the fibres effecting the shock response by increasing the rise time especially for the orientations of 25° and 45°. Also noted with the orientations of 25° and 45° was an increased amount of noise at the start of the stress plateau, however this may be coincidental in nature. The main difference between the traces is that oscillations are seen on the 0° orientation that are not observed on the other orientations. Apart from these slight notes the traces are broadly similar in nature, meaning that weave orientation has little effect on the shock profile. This is perhaps explained by the employment of gauges which will average the shock profile over an area meaning any subtle differences will not be seen by this diagnostic technique.

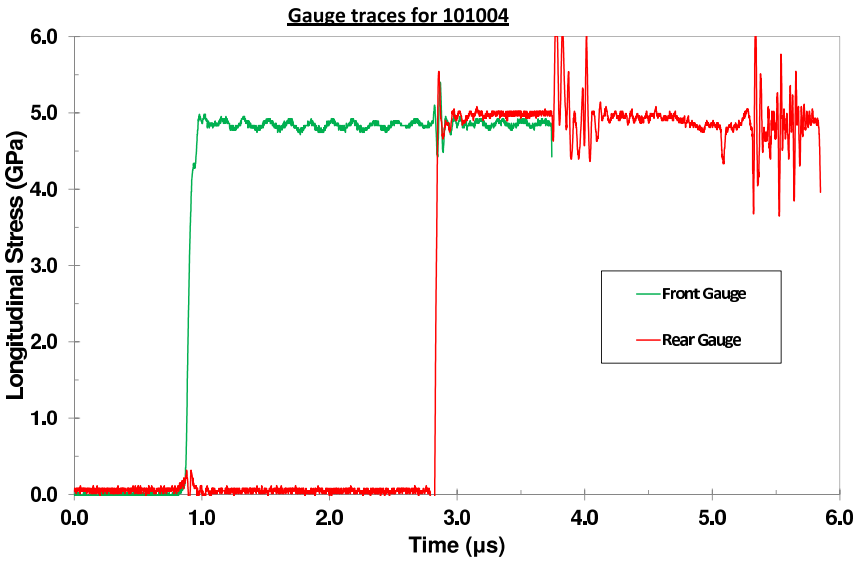

Figure 4.39: Traces for the experiment 101004 which consisted of a 10 mm copper projectile impacting a 0° TWCP sample at 869 m s^{-1}.

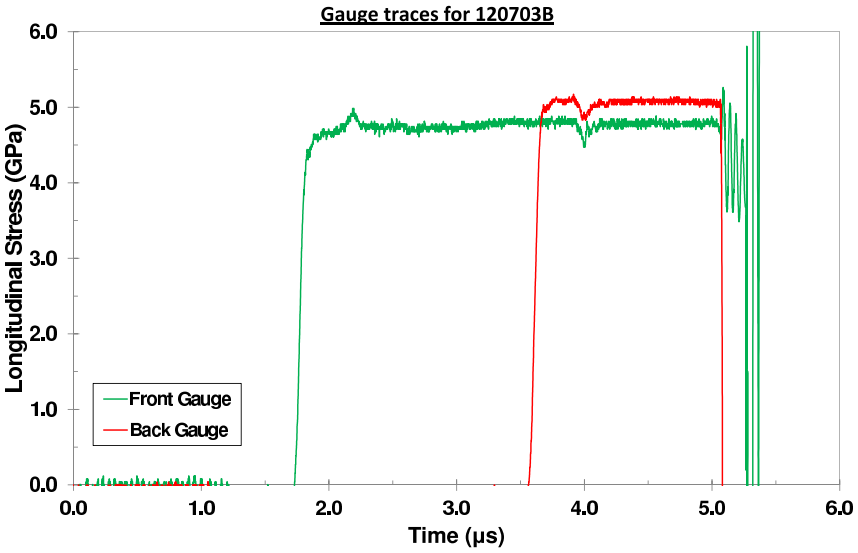

Figure 4.40: Traces for the experiment 120703B which consisted of a 10 mm copper projectile impacting a 90° TWCP sample at 890 m s^{-1}.

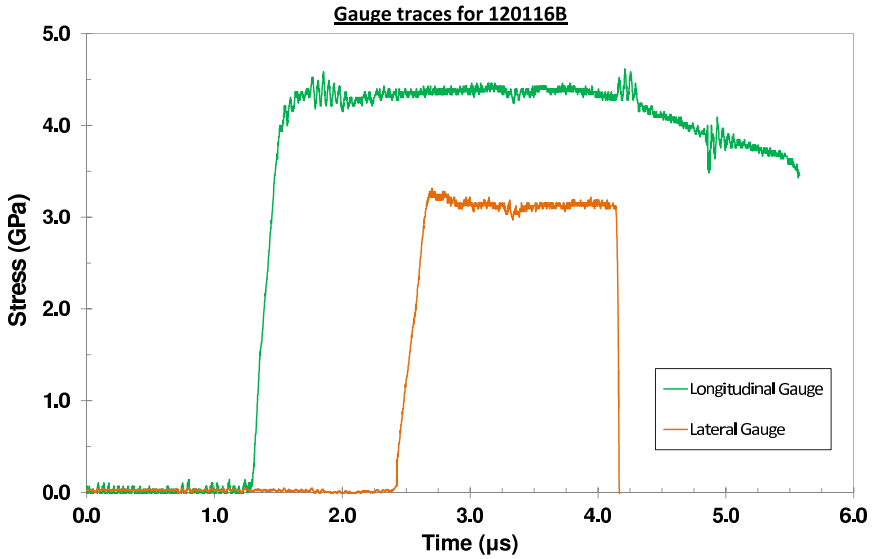

Figure 4.41: Traces for the experiment 120116B which consisted of a 10 mm copper projectile impacting a 25° TWCP sample at 822 m s^{-1}.

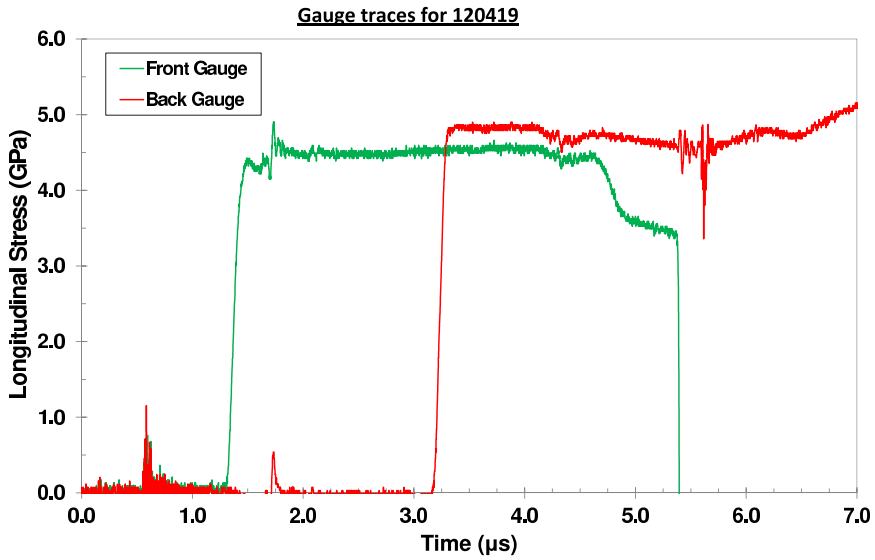

Figure 4.42: Traces for the experiment 120419 which consisted of a 10 mm copper projectile impacting a 45° TWCP sample at 839 m s^{-1}.

4.5.1 Oscillations

As noted with Figure 4.30, oscillations were observed with the lateral gauge at an orientation of 25°; for clarity, this figure is repeated in Figure 4.43. Oscillations were also seen with the 0° lay up as discussed in Chapter 4.4.2, with an example given in Figure 4.44 and also at 45° which is shown in Figure 4.45. No oscillations were seen in the 90° experimental trace results. The oscillations seen at the orientations of 25° and 45° were not as pronounced as the 0° orientation. Also for the orientations of 25° and 45° the only oscillations seen are shown below in Figures 4.43 and 4.45, implying that these oscillations need a precise set of conditions to become prominent enough to observe (both experiments performed were nearly identical with a difference in velocity of 15 m s^{-1}).

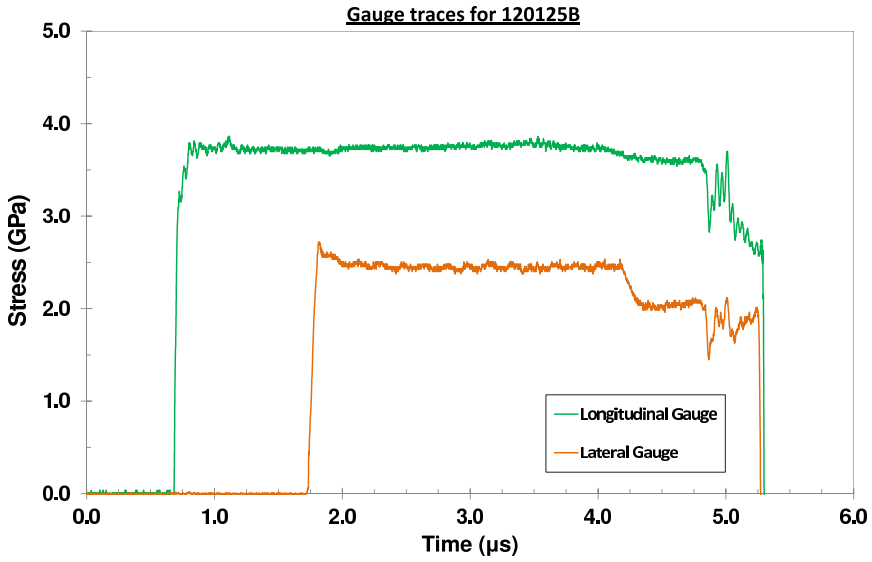

Figure 4.43: Traces for the lateral experiment 120125B which consisted of a 10 mm copper projectile impacting a 25° TWCP sample at 691 m s^{-1}.

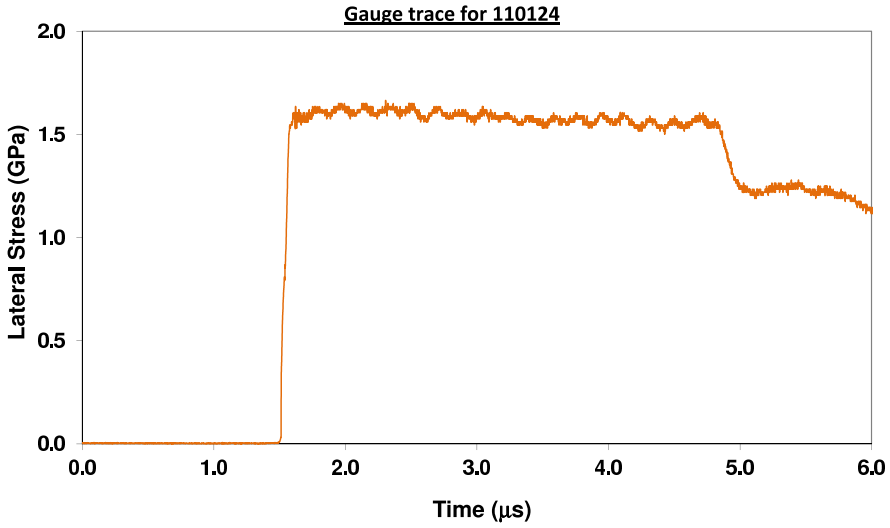

Figure 4.44: Traces for the lateral experiment 110124 which consisted of a 10 mm copper projectile impacting a 0° TWCP sample at 520 m s^{-1}.

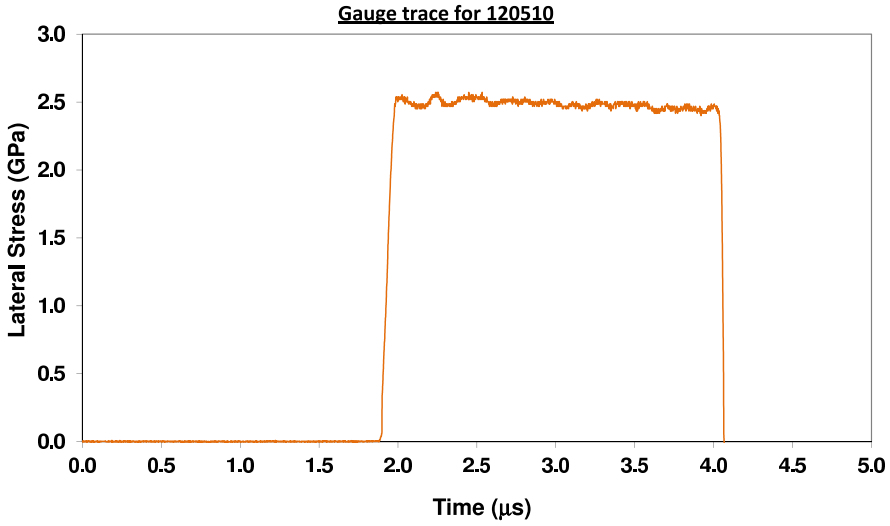

Figure 4.45: Trace for the lateral experiment 120510 which consisted of a 10 mm copper projectile impacting a 45° TWCP sample at 676 m s^{-1}.

4.6 Lateral Stress Measurements

All of the lateral data for the different weave orientations of the composite TWCP have been collated into one place to facilitate comparison and analysis. Initially the orientations will be looked at individually before being collated and contrasted. In addition, the

corresponding longitudinal experimental data has been repeated here for quicker reference as required.

4.6.1 Lateral Stress for the 0° Orientation

For the 0° orientated TWCP material the lateral stress data was gathered using a laterally orientated manganin gauge as shown in Figure 3.4b. Due to this all of the σ_x values are estimated using the known impact conditions, and the experimentally derived equation of state. Table 4.17 shows the experimental data obtained using the laterally orientated manganin gauges for the TWCP with a weave orientation of 0°. To obtain the shear strength and ultimately the Hugoniot elastic limit (HEL) of the material, Equation 2.25 combined with the elastic prediction given by Equation 2.31, leads to a deviation which is the HEL. The elastic prediction is based on the value of Poisson's ratio, which for this orientation is 0.28. As shown in Figure 2.6 with the method explained in Chapter 2.1 the deviation between the elastic prediction and the experimental data is the HEL. This led to an HEL value of 0.99±0.20 GPa. This is a comparable value to that reported by Dandekar *et al.* in Reference [12] (a HEL value of between 1.3 and 3.1 GPa) for a 0° lay up; however this is for a glass fibre composite so it would be expected that shock behaviour of these materials would be different, partially explaining the difference between the HEL of these materials. However this value is an approximation of the bulk properties of the composite and not necessarily a good representation of what will happen in practice. In practice the matrix material will plastically deform at a much lower value than the composite as a whole.

Experiment Number	Velocity m s^{-1}	Flyer Thickness/ Material mm	U_S mm μs^{-1}	u_p mm μs^{-1}	σ_x GPa	σ_y GPa	2τ GPa
110127	200	10 Al	3.78	0.14	0.76	0.41	0.35
110304	350	10 Al	3.84	0.25	1.45	0.84	0.61
110124	520	10 Cu	3.96	0.46	2.65	1.64	1.01
110330A	667	10 Cu	4.03	0.57	3.38	2.30	1.08
110303	900	10 Cu	4.08	0.65	3.96	2.65	1.31

Table 4.17: Lateral experimental results for the TWCP in the 0° orientation.

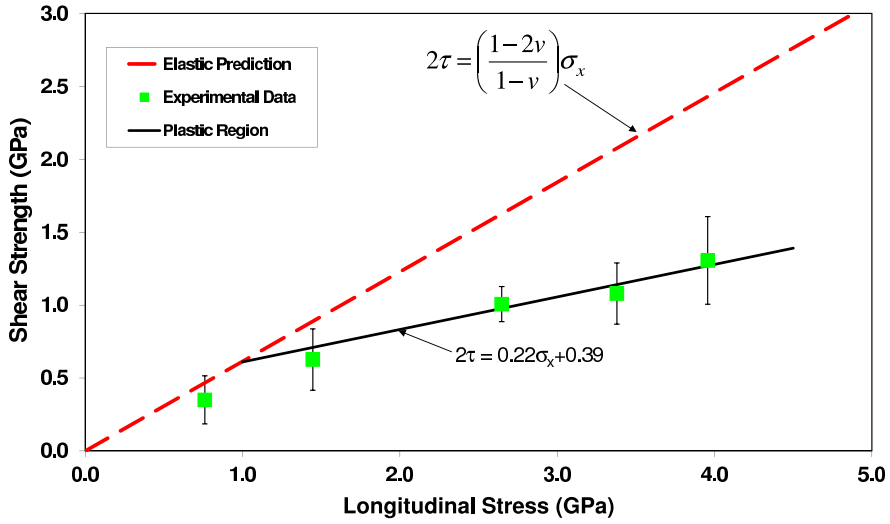

Figure 4.46: Variation of shear strength with impact stress for TWCP in the 0° orientation.

4.6.2 Lateral Stress for the 90° Orientation

Figure 4.47 shows the shear strength for the 90° weave orientation, with the data obtained from Table 4.18. The deviation between the elastic prediction and the plastic experimental data leads to a HEL value of 1.38±0.30 GPa. This value is slightly higher than the HEL found for the 0° orientation. A higher value would be expected due the increased stiffness of the TWCP material in the orientation as demonstrated by Poisson's ratio. However, it should be noted that, within the error bounds, the lowest value for the HEL of the 90° orientation and the highest value for the HEL of the 0° do overlap.

Experiment Number	Velocity m s^{-1}	Flyer Thickness/ Material mm	U_S mm μs^{-1}	u_p mm μs^{-1}	σ_x GPa	σ_y GPa	2τ GPa
110929A	292	5 Al	3.68	0.21	1.16	···	···
111021	312	10 Al	3.75	0.31	1.25	0.76	0.49
111010	350	10 Al	3.50	0.25	1.30	0.82	0.48
110804B	350	10 Al	4.17	0.26	1.53	0.87	0.66
110831	538	10 Al	3.70	0.39	2.32	1.47	0.85
110804A	632	10 Cu	4.21	0.46	2.79	1.94	0.85
110930	908	10 Cu	4.70	0.77	4.72	3.45	1.27

Table 4.18: Experimental results for the TWCP with the cloth angled perpendicular to the shock front for the lateral and longitudinal, and lateral only, experimental set ups.

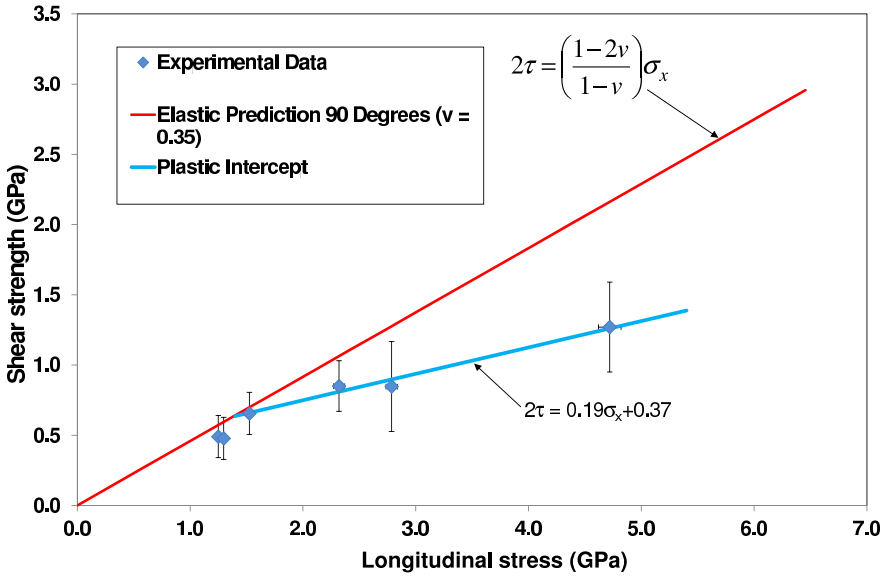

Figure 4.47: Variation of shear strength with impact stress for the 90° lay up.

4.6.3 Lateral Stresses for Intermediate Orientations (25° and 45°)

The shear strength behaviours for both the 25° and 45° orientations have been combined into one section due to the similarities in their behaviour as well as the resultant discussion. Tables 4.19 and 4.20 show the lateral experimental data relevant to the 25° and 45° lay ups respectively. Graphically this data is shown in Figure 4.48 for the 25° and Figure 4.49 for the 45° systems. In the figures it can be seen that the experiential data sits above the elastic prediction for the corresponding orientations, which is unrealistic in nature. Intersections with these data points do occur with the 90° (and conversely the

Experiment Number	Velocity m s^{-1}	Flyer Thickness/ Material mm	U_S mm μs^{-1}	u_p mm μs^{-1}	σ_x GPa	σ_y GPa	2τ GPa
120125A	397	10 Al	3.54	0.29	1.60	1.00	0.60
120116A	437	10 Al	3.54	0.32	1.77	1.05	0.72
120209A	534	10 Al	3.48	0.39	2.19	1.39	0.80
120210A	600	10 Cu	3.93	0.52	3.0.3	2.10	0.93
120125B	691	10 Cu	3.88	0.60	3.75	2.45	1.30
120116B	822	10 Cu	3.74	0.71	4.36	3.15	1.21

Table 4.19: Experimental results for the TWCP with the cloth angled at 25° to the shock front.

Experiment Number	Velocity m s^{-1}	Flyer Thickness/ Material mm	U_S mm μs^{-1}	u_p mm μs^{-1}	σ_x GPa	σ_y GPa	2τ GPa
111031	351	10 Al	3.03	0.26	1.43	0.94	0.49
111122	538	10 Al	3.78	0.39	2.10	1.47	0.63
111028	579	10 Cu	3.43	0.51	2.97	2.23	0.74
120510	676	10 Cu	4.03	0.58	3.42	2.49	0.93
111118B	824	10 Cu	4.75	0.69	4.80 Est.	3.25	1.56

Table 4.20: Experimental results for the TWCP with the cloth angled at 45° to the shock front.

0° which has been omitted from the figure for clarity), but are deemed to be due to the interpretation of the elastic prediction. The elastic prediction is based on Poisson's ratio which is ascertained from both the longitudinal and shear sound speed values (c_L and c_S respectively) as discussed in Sections 2.1 and 3.4. With both the 25° and 45° orientations, the longitudinal and shear sound speeds are at best "quasi" in their nature (as seen by Dandekar *et al.* in Reference [13]). This is due to the values being a component of their respective sound speed. Due to this behaviour it is not inconceivable that this would greatly affect the value of Poisson's ratio leading to a value that would be unrepresentative of the the composite as a whole, at these orientations. These longitudinal and shear sound speed would also effect the lateral strength measured due to the inclusion of Poisson's ratio for the value of β within the calibration of the lateral gauges as shown in Section 3.2.2.

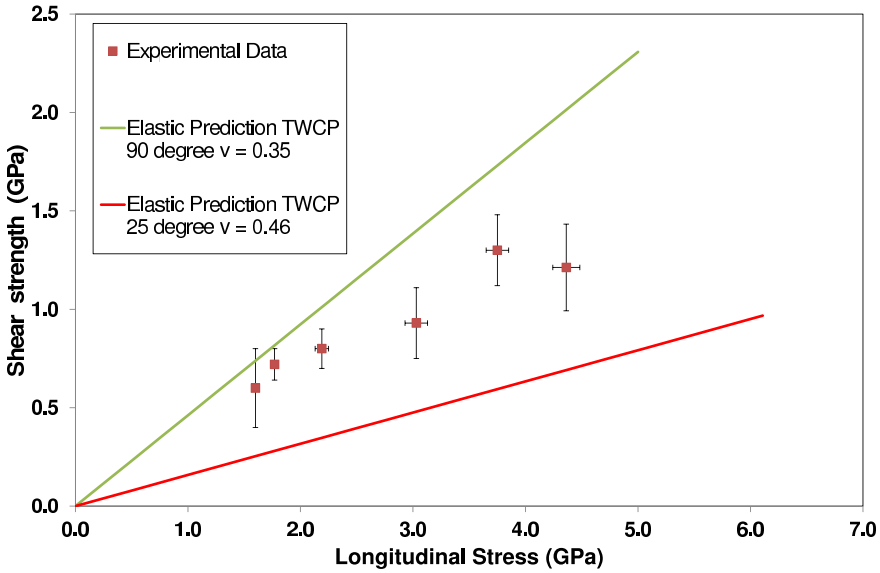

Figure 4.48: Variation of shear strength with impact stress for the 25° lay up.

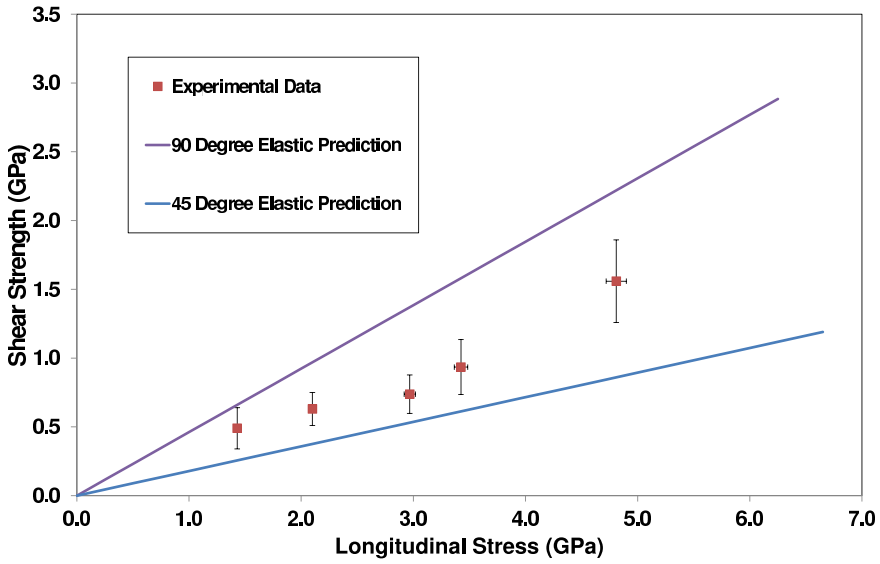

Figure 4.49: Variation of shear strength with impact stress for the 45° lay up.

4.6.4 Lateral Stress Discussion

Lateral gauges by their nature are an intrusive technique and due to this it is worth considering whether the lateral data obtained here is due to the composite or a response closer in behaviour to the matrix material. By comparing all of the lateral stress data gathered for the sample with respect to a given u_p value, Figure 4.50 is obtained. From

this it seems that lateral stress is the same regardless of the orientation, or whether it is the composite or matrix material under investigation. This implies that the strength laterally is dominated by the matrix material, or alternatively that the lateral gauges are too intrusive for the TWCP samples, as it would be expected that the inclusion of the fibres would increase the lateral stress. The deviation seen in shear strength would then be due to the fibres in the composite causing a difference in longitudinal stress.

The assumption that the matrix material is dominant in lateral stress response could be explained in terms of the fact that as the first damage mechanisms that occur are due to the matrix material in the composite (matrix cracking and delamination) as discussed by Richardson and Wisheart [53]. The elastic constants for the composite given in Equation 4.8 are broadly similar, meaning that any elastic behaviour in the composite is comparable in nature, which would lead to HEL values that are not too dissimilar. However as seen by Bordzilovsky *et al.* [20] the HEL value decreased in the traces as the angle orientated off axis. This would be the expected behaviour meaning that the most likely reason for the lateral stress to be dominated by the matrix is due to the lateral gauge technique breaking up the long range order seen in the fibres.

Figure 4.51 compares the pressure against the particle velocity (the pressure-u_p plane is used due to the sensitivity of volume to both U_S and u_p). For this figure the pressure is calculated using the Hugoniot equations, hence the similarity between the orientations of the TWCP. Due to deviation of some of the TWCP orientations at the higher u_p values, Figure 4.52 has been created using the data gathered experimentally. Examining the experimental data it can seen there is little to no scatter between the different orientations. The most extreme deviation is seen for the highest stress experiment for the weave orientation of 0°; this however was seen as deviation from the hydrostat, behaviour that was not observed at any of the other orientations. As all orientations of the TWCP composite as well as the matrix material respond the same laterally it is possible that the lateral gauges are too intrusive and break any long range order that is present within the composite.

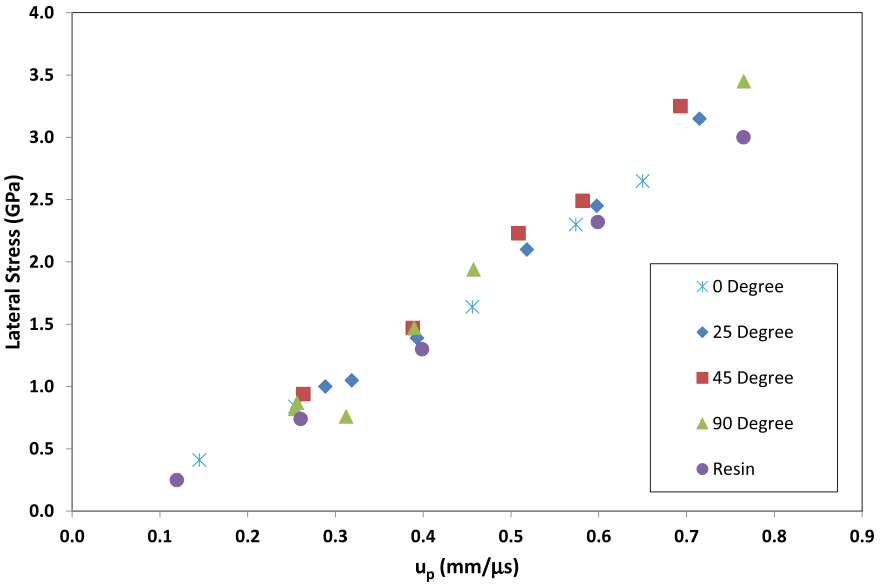

Figure 4.50: Lateral stress against u_p for all targets investigated.

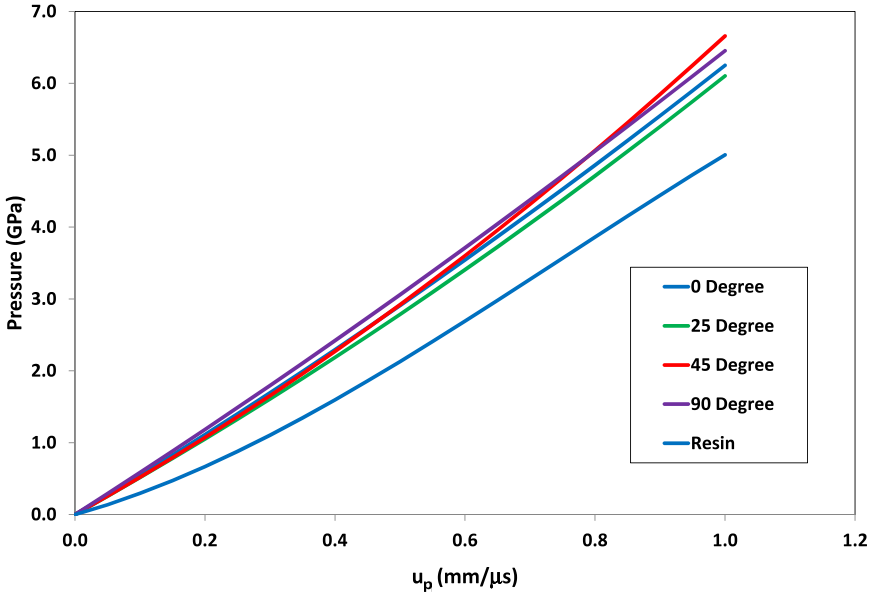

Figure 4.51: Hugoniot pressure compared with particle velocity for all investigated materials.

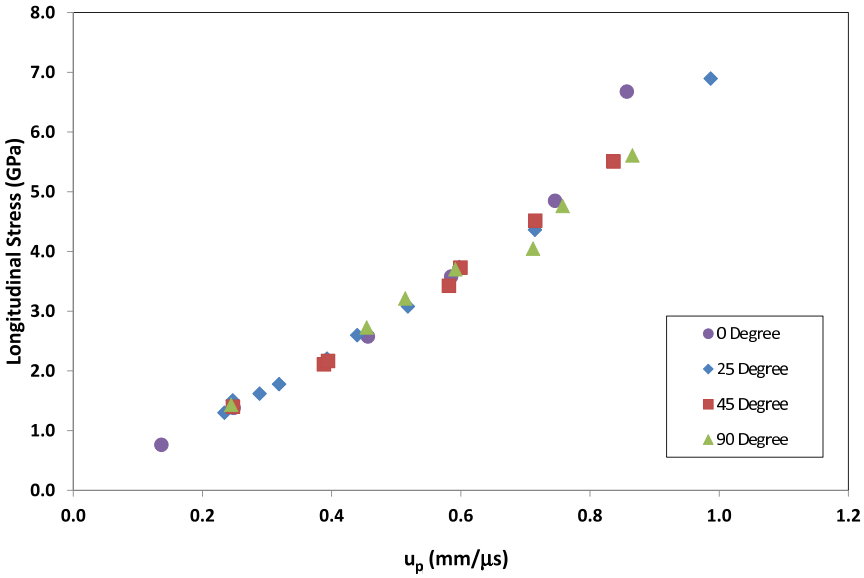

Figure 4.52: Longitudinal stress compared with particle velocity for all investigated materials using experimental data only.

4.7 Data Collation for the TWCP

As it is possible to say that the lateral stress may be dominated by the matrix material, it is worth investigating whether the shock profiles can also be reduced down into one data set. Figure 4.53 shows the experimental data (with the scatter removed) for the four different orientation of TWCP superimposed onto the same graph. Looking at the data, scatter is most apparent for the 25° and 90° orientation. The 0° and 45° lay ups shows consistent results over the investigated range. It was expected that the 90° would show more deviation from the rest of the orientations due to the shock wave being elastic through most of the investigated pressure regime. For the 90° orientation the values of U_S up to a u_p of 0.6 mm μs^{-1} were *ca.* 4.2 mm μs^{-1}; *i.e.* the c_L value. The 25° orientation is more surprising however given how well the 45° matches up with the 0° data. This may be due to the scatter induced in the data by using multiple diagnostic methods. It can be seen that only a few 25° experimental data points are low-lying causing the observed scatter. If these were removed then the 25° data would sit very well alongside the data for the 0° and 90°. By taking all of the experiments as one data set a Hugoniot in the U_S-u_p plane was found which was linear in nature with the equation shown in Equation 4.15, which can be seen in Figure 4.54. While there is scatter the majority (about two thirds) of data intersect this Hugoniot if their associated error bars are taken into account. While this will not be as exact as taking each individual Hugoniot it is a good approximation. It also goes to show that for this material, the orientation does not affect the shock properties as much as one would expect. However there is greater deviation with the 90° material due to the high longitudinal sound speed c_L leading to elastic behaviour.

$$U_S = 3.56 + 0.84u_p \tag{4.15}$$

Using the reduced data Hugoniot on the pressure-particle velocity plane the data matches up very well. Some deviation is seen at the higher end, but overall the agrement is very good over the investigated range.

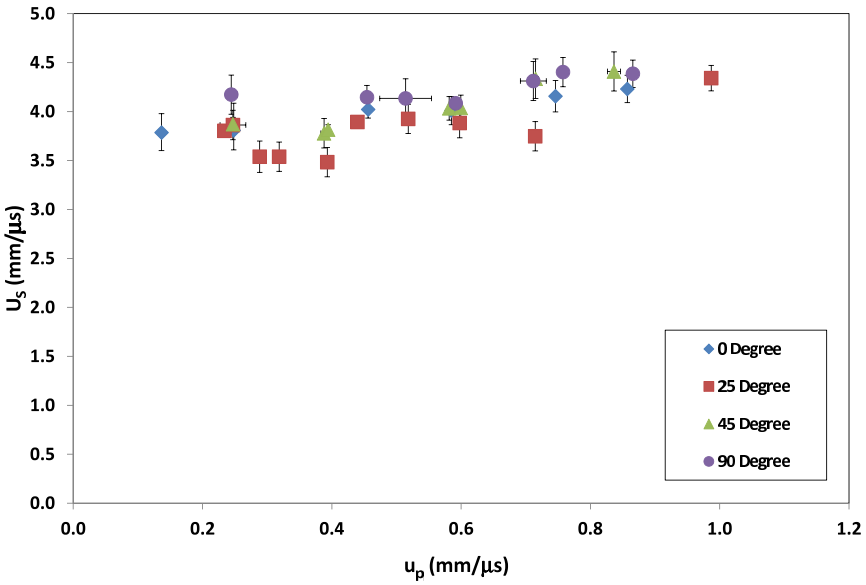

Figure 4.53: All of the experimental data for the different TWCP orientations.

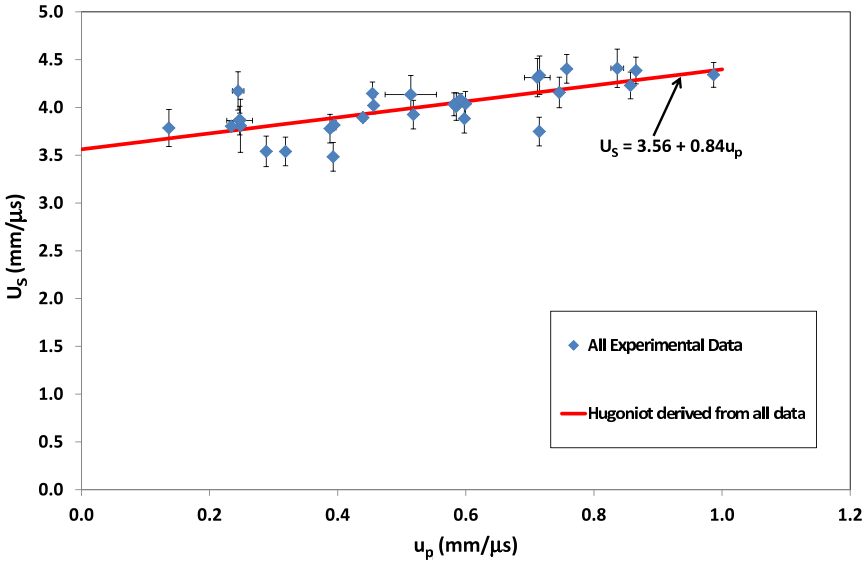

Figure 4.54: All experimental data reduced into one data set.

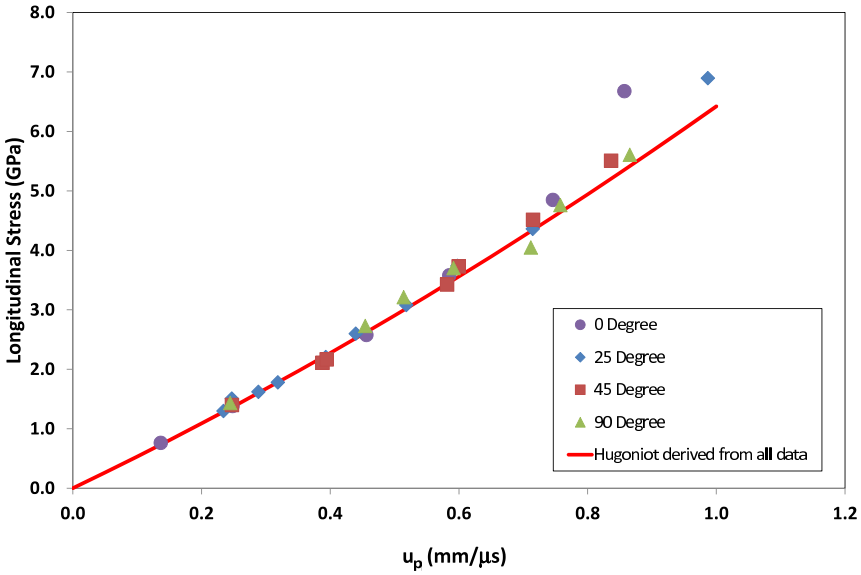

Figure 4.55: Hugoniot found from reduced data set compared with the experimental data.

By using this data it is possible to use a single Hugoniot for all of the data sets in both the U_S-u_p and P-u_p planes, with better agrement found in the P-u_p plane up to a particle velocity of 1 mm μs^{-1}.

Chapter 5

Conclusions

Through the use of a single stage gas gun combined with manganin pressure gauges situated in both the longitudinal and lateral orientation, the shock response of a carbon fibre composite has been investigated. This composite, known by the acronym TWCP, has been investigated along with the matrix material a phenolic resin named Durite SC-1008. For the TWCP, four orientations were investigated to see the effect that the weave angle has on the shock response. These angles were 0° (fibre weave orientated parallel to the shock front), 25°, 45° and 90°.

5.1 Shock Hugoniot

For the matrix material Durite SC-1008, a non-linear U_S-u_p Hugoniot with the equation of $U_S = 2.14 + 3.79u_p - 1.68u_p^2$ was found. This non-linear behaviour is similar to that observed elsewhere in other polymeric materials such as PMMA [26], PRR [27] and various epoxy resins investigated by Carter and Marsh [28]. This non-linear behaviour was attributed to the nature of the polymeric material; *e.g.* to a two-stage collapse under shock, with the initial weaker inter chain forces being overcome before the backbone begins to be compressed. Between u_p values of 0.7 to 0.9 mm μs^{-1} data found by Carter and Marsh for the phenolic resin Durite HR-300 Borden agreed well with the Hugoniot found here. This suggests that it is possible that phenolic resins will have consistently

broadly similar Hugoniots as has been seen with epoxy resins (*e.g.* Munson and May [69]), as the densities and sound speeds of these phenolic resins are different. If this were true then it would be expected that the Hugoniot would become linear in nature at the higher end (above a u_p value of 0.6 mm μs^{-1}). Deviation at the higher pressure range in the pressure-volume plane was noticed as well, in line with similar behaviour noted elsewhere in other polymers like RTM-6 [70]. However if the behaviour did become linear at higher u_p values then this noted deviation would disappear. A Hugoniot elastic limit of 0.36±0.10 GPa was also found. Investigating the shock response of the TWCP a level of scatter was noticed and attributed to the different experimental methods used; which were PMMA offset, combined longitudinal and lateral orientated manganin gauges, as well as the standard two longitudinally orientated manganin gauge technique. Also it should be noted that the scatter increased with the angle of the weave (little scatter on 0° (shock front parallel to the fibres) and the most on 90° (shock front perpendicular to the fibres)).

For the 0° orientated TWCP a linear Hugoniot was found with the equation $U_S = 3.69 + 0.59u_p$. Convergence between this Hugoniot and the one ascertained for the matrix material was noted, as was convergence with the composite investigated by Millett *et al.* [16]. Deviation from the Hugoniot pressure was seen at higher stress levels, in line with the similar behaviour also seen in the matrix material (the phenolic resin Durite SC-1008). Oscillations were seen on the stress plateaus of many of the traces, which were attributed to the shock wave interacting with the carbon fibre weave. Consequently, the period of the oscillations corresponded to the thickness of the carbon fibre layer which was between 350 and 400 μm.

The 90° TWCP orientation has also been shown to possess a linear Hugoniot, with the equation $U_S = 3.69 + 0.46u_p$. Due to the high value of c_L the initial data on the U_S-u_p Hugoniot (up until a u_p value of 0.6 mm μs^{-1}) was elastic in nature. Convergence was noted between the 0° and 90° orientated samples. Scatter was noticed in the experimental data and found to be due to using multiple experimental methods. The method that

gave the most scatter was the PMMA offset followed by the combined longitudinal and laterally orientated manganin gauge set up approach. Looking at the data gathered by Millett *et al.* [16] and Hazell *et al.* [17] a degree of scatter, though minimal in nature, can be seen in their experimental data. Both of these author's used the PMMA offset method, so it is likely that this technique is the largest contributor to the scatter seen at this angle.

For the 25° cloth orientation less scatter was noted, especially when compared to the 90° orientation. The majority of data (60%) agreed with the Hugoniot found for the 0° orientation in the U_S-u_p plane with the data in the pressure-volume plane having a 70% correlation with the 0° Hugoniot. The Hugoniot in the U_S-u_p plane had the equation $U_S = 3.45 + 0.73u_p$. Convergence for the Hugoniots for the 0°, 25° and 90° occurred in both the U_S-u_p and the pressure-volume plane, with similar convergence observed with the Hugoniot for a 20° TWCP investigated by Burrell *et al.* [19].

For the TWCP with the 45° lay up, more scatter was seen than when compared to the 25° orientation. When the data was reduced a linear Hugoniot with the equation of $U_S = 3.44 + 1.12u_p$ was obtained. As seen with the 25° material the majority of data agreed with the Hugoniot obtained for the 0° orientation in both the U_S-u_p plane and pressure-volume plane. Interestingly this is the only angle that deviates from the others, after an initial convergence and intersection at a u_p value of 0.5 mm μs^{-1}.

As discussed it was found the four Hugoniots for the different orientations were comparable in nature. It was found that a single Hugoniot equation of $U_S = 3.56 + 0.84u_p$ could be used. In the U_S-u_p plane more than 60% of the experimental data agreed with this Hugoniot if the error bars were taken into account. Better agreement was apparent in the pressure-u_p plane, though some deviation was seen at the higher end which corresponded to the deviation of their respective Hugoniots. This likely implies that orientation does not have as great an affect as would have been thought or has seen in other composite materials.

In summary the four Hugoniots obtained for the different orientations are shown below, as well as the "average" Hugoniot that can be used for all of the data.

- 0° $U_S = 3.69 + 0.59u_p$
- 25° $U_S = 3.45 + 0.73u_p$
- 45° $U_S = 3.44 + 1.12u_p$
- 90° $U_S = 3.96 + 0.46u_p$
- All Data $U_S = 3.56 + 0.84u_p$

5.2 Strength of the TWCP Orientations

For the 0° orientation an HEL of 0.99±0.20 GPa was found. This was comparable to the HEL range for a glass fibre composite investigated by Dandekar *et al.* [12]. With the TWCP in the 90° orientation an HEL value of 1.38±0.30 GPa was obtained. Unexpected behaviour was noted in both the 25° and 45° TWCP orientations. Due to the high values of Poisson's ratio (approximately ν=0.45) no intersection was seen between the experimental data and the elastic prediction. This behaviour has been attributed to the value of Poisson's ratio being altered due to the quasi like nature of the sound speed ascertained via the ultrasonic techniques. This conclusion is backed up by the fact that the lateral stress is the same for the resin and all TWCP orientations. This may mean one of two things, (1) that lateral stress is dominated by the matrix material, or (2) that the insertion of a laterally orientated manganin pressure gauge breaks up the order of the composite - therefore meaning this method is incompatible with these types of composites in general. This difference in shear strength is due to a difference between the TWCP orientations and the matrix material. It was also found that there was no difference between the longitudinal stresses in the composites when examined in the pressure-u_p plane.

5.3 Summary

In summary the aims of this PhD - to investigate the shock behaviour of a carbon fibre composite (TWCP) have been achieved. The equation of state for the matrix material as well as four different orientations have been investigated and contrasted with comparable materials. It was found that.

- Linear Hugoniots exist for all four orientations of TWCP; with a non-linear Hugoniot obtained for the matrix material, which was a phenolic resin
- It is possible to use a single Hugoniot to explain all four TWCP orientations with reasonable accuracy
- Scatter was present in the experimental data, becoming more pronounced as the angle became more extreme with regard to the shock front
- The strength of the material has been investigated with unexpected behaviour noted. In the composite it seems that one of two possibilities exist

    1. The value for Poisson's ratio for the 25° and 45° lay ups is incorrect due to the quasi like nature of the sound speeds
    2. Lateral gauges are not an appropriate technique for these types of composites (ones with long range order)

In conclusion, the main aims of this research project have been achieved. In particular, this study has built on previous work investigating the shock response of fibre-reinforced systems, extending these studies to consider the effects of more than just the typically considered orthogonal (0° and 90°) orientations. The use of manganin gauges in conjunction with such a highly ordered composite is, to the authors' knowledge, a novel approach and has proved successful. In addition to allowing derivations of Hugoniot equations of state, the lateral response of the TWCP was investigated, with behaviour behind the shock providing an insight into shock propagation in this complex layered

system. Combination of the lateral and longitudinal data, along with predicted elastic responses, provided a strong indication that material strength was largely dominated by the matrix - however with the caveat that the active area of the lateral gauges was significantly larger than the underlying composite layer scales, potentially breaking up the systems long range order. Overall, this project has successfully characterised a potentially important aerospace relevant composite, applying established techniques in a relatively novel manner. This provided an insight into its behaviour under shock loading, thereby helping extend the body of knowledge into this important class of materials.

5.4 Future Work

Despite the success of this investigation, there are a number of areas where further study could potentially be warranted. In particular, future work could focus on the removal of the scatter seen in the experimental data, along with interrogation of the cause behind it. The next experimental technique that would be investigated would be the inclusion of lateral gauges. The data suggests that the matrix material is dominating the lateral behaviour of the composite. By using alternative methods of finding material strength like the self-consistent method it may be possible to prove whether lateral gauges are a valid technique for measuring strength in complex composite materials. In addition to development of experimental techniques, other behaviour could also be investigated. The Hugoniots for both the composite and resin would ideally be increased above 1 mm μs^{-1} to observe if the convergence seen in the experimental data continues at higher particle velocities. Comparable materials could also be investigated to elucidate understanding of the physics behind shock wave interactions in composite materials. In particular, this could be facilitated by the fact that multiple materials could used instead of the carbon fibre weave, like sheet metals with the thicknesses of each layer altered, in order to investigate particular mechanics.

Chapter 6

Publication History

Through this PhD a number of conferences have been attended. As well as this a publication history has been built up through the conferences proceedings and journal articles.

6.1 Conferences

The conferences that have been attended are as follow

- The first Institute of Shock Physics (ISP) annual conference, poster presentation given, February 2010 at the Royal Society, London UK
- International Shock Wave Institute (ISWI), presentation given, September 2010 at Cambridge University, Cambridge UK
- The second ISP annual conference, presentation given, February 2011 at Institute of Physics (IOP), London UK
- Cranfield University student symposium, presentation given, May 2011 at Defence Academy of the UK, Shrivenham UK
- Shock Compression of Condensed Matter (SCCM), presentation given, June 2011 at Marriott Hotel, Chicago USA

- The third annual ISP conference, poster presentation given, March 2012 at IOP, London UK

6.2 Conference Proceedings

Three conference proceeding have been published all for the Shock Compressions of Condensed Matter 2011, with the proceedings published by the American Institute of Physics, which can be found in the AIP conference proceeding 1426.

- "The shock response of a tape wrapped carbon fiber composite", D.C. Wood, P.J. Hazell, G.J. Appleby-Thomas and N.R. Barnes, Pages 184-186
- "On the importance of encapsulation environment for lateral gauges", J.D. Painter, G.J. Appleby-Thomas, P.J. Hazell, R.E. Winter, E.J. Harris, G.D. Owen and D.C. Wood, Pages 454-457
- "Experimental and computational investigation of lateral gauge response in polycarbonate", J. Eliot, E.J. Harris, P.J. Hazell, G.J. Appleby-Thomas, R.E Winter and D.C. Wood, Pages 458-461

6.3 Journal Articles

- "On the interpretation of lateral manganin gauge stress measurements in polymers", G.J. Appleby-Thomas, P.J. Hazell, J.M. Wilgeroth and D.C. Wood, Journal of Applied Physics, Volume 108, Pages 033524 (2010)
- "On the dynamic behavior of three readily available soft tissue simulants", G.J. Appleby-Thomas, P.J. Hazell, J.M. Wilgeroth, C.J. Shepherd, D.C. Wood and A. Roberts, Journal of Applied Physics, Volume 109, Pages 084701 (2011)
- "Ballistic behaviour of explosively shattered alumina and silicon carbide targets", H. Nanda, G.J. Appleby-Thomas, D.C. Wood and P.J. Hazell, Advances in Applied

Ceramics, Volume 110, Issue 5, Pages 287-292 (2011)

- "Shock behaviour of a phenolic resin", D.C. Wood, P.J. Hazell, G.J. Appleby-Thomas and N.R. Barnes, Journal of Materials Science, Volume 46, Issue 18, Pages 5991-5999 (2011)

- "On the effects of lateral gauge misalignment in shocked targets", G.J. Appleby-Thomas, P.J. Hazell, D.C. Wood, J.M. Wilgeroth and J.A. Leighs, Review of Scientific Instruments, Volume 83, Issue 6, Pages 063904 (2012)

- "Shock propagation in a tape wrapped carbon fibre composite", D.C. Wood, G.J. Appleby-Thomas, P.J. Hazell and N.R. Barnes, Composites Part A: Applied Science and Manufacturing, Volume 43, Issue 9, Pages 1555-1560 (2012)

References

[1] F.L. Matthews and R.D. Rawlings. *Composite Materials: Engineering and Science*. Woodhead Publishing Limited, Cambridge, 2nd edition, 2002.

[2] J.C.F Millett and N.K. Bourne. The shock Hugoniot of a plastic bonded explosive and inert simulants. *Journal of Physics D: Applied Physics*, 37:2613–2617, 2004.

[3] J.C.F. Millett, N.K. Bourne, and D. Deas. The equation of state of two alumina-filled epoxy resins. *Journal of Physics D: Applied Physics*, 38:930–934, 2005.

[4] M. Edwards. *Comprehensive Composite Materials*, volume 6, chapter Land-based military applications, pages 681–699. Elsevier Science, Oxford, 2000.

[5] T. Windhorst and G. Blount. Carbon-carbon composites: a summary of recent developments and applications. *Materials and Design*, 18:11–15, 1997.

[6] S. Ryan, F. Schäfer, M. Guyot, S. Hiermaier, and M. Lambert. Characterising the transient response of CFRP/Al HC spacecraft structures induced by space debris impact at hypervelocity. *Journal of Impact Engineering*, 35:1756–1763, 2008.

[7] C. Bisagni, G. Di Pietro, L. Fraschini, and D. Terletti. Progressive crushing of fiber-reinforced composite structural components of a formula one racing car. *Composite Structures*, 68:491–503, 2005.

[8] Nobel M600. Website http://www.noblecars.com accessed on 05/09/2011 @ 11.22.

[9] A.B. Strong. Breakthroughs in aerospace composites manufacturing. *Composites Manufacturing*, August 2004.

[10] A.B. Strong. Space structures: Lessons for everyone. *Composites Manufacturing*, April 2003.

[11] L. Tsai, V. Prakash, A.M. Rajendran, and D.P. Dandekar. Structure of shock waves in glass fiber reinforced polymer matrix composites. *Applied Physics Letters*, 90:061909, 2007.

[12] D.P. Dandekar, C.A. Hall, L.C. Chhabildas, and W.D. Reinhart. Shock response of a glass-fiber-reinforced polymer composite. *Composite Structures*, 61:51–59, 2003.

[13] D.P. Dandekar, J.M. Botelar, and P.A. Beaulieu. Elastic constants and delamination strength of a glass-fibre-reinforced polymer composite. *Composites Science and Technology*, 58:1397–1403, 1998.

[14] J.C.F Millett, Y.J.E. Meziere, and N.K. Bourne. The response to shock loading of a glass-fibre-epoxy composite: effects of fibre orientation to the loading axis. *Journal of Physics D: Applied Physics*, 40:5358–5365, 2007.

[15] E. Zaretsky, G. deBotton, and M. Perl. The response of a glass fibers reinforced epoxy composite to an impact loading. *International Journal of Solids and Structures*, 41:569–584, 2004.

[16] J.C.F. Millett, N.K. Bourne, Y.J.E. Meziere, R. Vignjevic, and A. Lukyanov. The effect of orientation on the shock response of a carbon fibre-epoxy composite. *Composites Science and Technology*, 67:3253–3260, 2007.

[17] P.J. Hazell, C. Stennett, and G. Cooper. The effect of specimen thickness on the shock propagation along the in-fibre direction of an aerospace-grade CFRP laminate. *Composites Part A: Applied Science and Manufacturing*, 40:204–209, 2009.

[18] M. Willows, K. Tsembelis, W.G. Proud, and P.D. Church. Shock characterisation of a carbon-fibre composite. In *American Physical Society, 15th APS Topical Conference on Shock Compression of Condensed Matter 2007*, 2008. Poster presentation paper not published.

[19] R.H. Burrell, N.R. Barnes, P.T. Keightley, J.C.F. Millett, and N.K. Bourne. The response of a carbon-fibre-phenolic resin composite to one-dimensional shock loading. In *Americian Physical Society, 16th APS Topical Conference on Shock Compression of Condensed Matter 2009*, 2009. Poster presentation paper not published.

[20] S.A. Bordzilovsky, S.M. Karakhanov, and L.A. Merzhievsky. Shock response of a unidirectional composite at various orientation of fibers. In *American Physical Society, 10th APS Topical Conference on Shock Compression of Condensed Matter 1997*, pages 545–548, 1998.

[21] The Physics Hypertextbook. Shock waves. Website http://physics.info/shock/ accessed on 19/03/2010.

[22] M.A. Meyers. *Dynamic Behavior of Materials*. Wiley-Interscience Publication, New York, 1st edition, 1994.

[23] Y. Horie and A.B. Sawaoka. *Shock compression chemistry of materials*. KTK Scientific Publisher, Tokyo, 1st edition, 1993.

[24] J.C.F Millett and N.K. Bourne. Lateral stress measurements in a shock loaded alumina: Shear strength and delayed failure. *Journal of Materials Science*, 36:3409–3414, 2001.

[25] L.V. Al'tshuler. Use of shock waves in high-pressure physics. *Soviet Physics Uspekhi*, 8:52–91, 1965.

[26] L.M. Barker and R.E. Hollenbach. Shock-wave studies of PMMA, fused silica and sapphire. *Journal of Applied Physics*, 41:4208–4226, 1970.

[27] G.J. Appleby-Thomas, P.J. Hazell, C. Stennett, G. Cooper, and R. Cleave. The dynamic behaviour of a modified polyurethane resin. In *DYMAT Internatonal Conference Proceedings 2009*, pages 1081–1087. DYMAT, 2009.

[28] W.J. Carter and S.P. Marsh. Hugoniot equation of state of polymers. Technical Report LA-13006-MS, Los Alamos National Laboratory, 1995.

[29] S.P. Marsh. *LASL Shock Hugoniot Data*. University of California Press, 1st edition, 1980.

[30] Z. Rosenberg and N.S. Brar. The influence of the elasto-plastic properties of piezoresistance gauges on their loading-unloading characteristics as lateral shock stress transducers. *Journal of Applied Physics*, 77:1443–1448, 1995.

[31] J.R. Asay and J. Lipkin. A self-consistent technique for estimating the dynamic yield strength of a shock-loaded material. *Journal of Applied Physics*, 49:4242–4247, 1978.

[32] Z. Rosenberg and Y. Partom. Lateral stress measurements in shock-loaded targets with transverse piezoresistance gauges. *Journal of Applied Physics*, 58:3072–3076, 1985.

[33] D.N. Fenner. *Enginering Stress Analysis: A finite element approach with FORTRAN 77 software*. Ellis Horwood Limited, Chichester, 1st edition, 1987.

[34] P.P. Benham, R.J. Crawford, and C.G. Armstrong. *Mechanics of Engineering Materials*. Pearsons, Essex, 2nd edition, 1996.

[35] J.E. Field, S.M. Walley, W.G. Proud, H.T. Goldrein, and C.R. Siviour. Review of experimental techniques for high rate deformation and shock studies. *International Journal of Impact Engineering*, 30:725–775, 2004.

[36] W.N. Sharpe, editor. *Springer Handbook of Experimental Solid Mechanics*. Springer, New York, 1st edition, 2008.

[37] S. Fujiwara. *Shock Compression Technology and Material Science*. KTK Scientific Publisher, Terra Scientific Publishing Company, Tokyo, 1992.

[38] M.A. Meyers and L.E. Murr, editors. *Shock waves and high-strain-rate phenomena in metals*. Plenum Publishing Corporation, New York, USA, 1981.

[39] K.A. Tanaka, M. Hara, N. Ozaki, Y. Sasatani, S.I. Anisimov, K. Kondo, M. Nakano, K. Nishihara, H. Takenaka, M. Yoshida, and K. Mima. Multi-layered flyer accelerated by laser induced shock waves. *Physics of Plasmas*, 7:676–680, 2000.

[40] R. Dendy. *Plasma Physics An Introductory Course*. Cambridge University Press, Cambridge UK, 1996.

[41] M. Boustie, L. Berthe, T. de Resseguier, and M. Arrigoni. Laser shock waves: Fundamentals and applications. In *1st International Symposium on Laser Ultrasonics: Science, Technology and Applications*, 2008.

[42] S.N. Luo, D.C. Swift, T.E. Tierney IV, D.L. Paisley, G.A. Kyrala, R.P Johnson, A.A. Hauer, O. Tschauner, and P.D. Asimow. Laser-induced shock waves in condensed matter: some techniques and applications. *High Pressure Reasearch*, 24:409–422, 2004.

[43] Y. Yang, S.A. Hambir, and D.D. Dlott. Ultrafast vibrational spectroscopy imaging of nanoshock planar propagation. *Shock Waves*, 12:129–136, 2002.

[44] Various Authors. Time-resolved diagnostics: Measurements of behaviour at high strain-rates. Technical report, Institute of Shock Physics, Febuary 2011.

[45] W.M. Isbell. *Shock Waves: Measuring the Dynamic Response of Materials*. Imperial College Press, London, 2005.

[46] Z. Rosenberg, D. Yaziv, and Y. Partom. Calibration of foil-like manganin gauges in planar shock wave experiments. *Journal of Applied Physics*, 51:3702–3705, 1980.

[47] R.L. Simpson, F.H. Helm, and J.W. Kury. Non-reactive HMX shock Hugoniot data. *Propellants, Explosives, Pyrotechnics*, 18:150–154, 1993.

[48] J.R. Vinson and R.L. Sierakowski. *The Behavior of Structures Composed of Composite Materials*. Martinus Nijhoff Publishers, Dordrecht, 1986.

[49] R. Vignjevic, J.C. Campbell, N.K. Bourne, and N. Djordjevic. Modeling shock waves in orthotropic elastic materials. *Journal of Applied Physics*, 104:044904, 2008.

[50] T.T. Wu and Y.H. Liu. On the measurement of anisotropic elastic constants of fiber-reinforced composite plate using ultrasonic bulk wave and laser generated Lamb wave. *Ultrasonics*, 37:405–412, 1999.

[51] D. Hull and T.W. Clyne. *An Introduction to Composite Materials*. Cambridge University Press, Cambridge UK, 2nd edition, 1996.

[52] F.R. Jones. *Handbook of Polymer-Fibre Composites*. Longman Scientific and Technical, 1st edition, 1996.

[53] M.O.W. Richardson and M.J. Wisheart. Review of low-velocity impact properties of composite materials. *Composites Part A: Applied Science and Manufacturing*, 27:1123–1131, 1996.

[54] D. Liu. Impact-induced delamination - a view of bending stiffness mismatching. *Journal of Composite Materials*, 22:674–692, 1988.

[55] O.S. David-West, N.V. Alexander, D.H. Nash, and W.M. Banks. Energy absorption and bending stiffness in CFRP laminates: The effect of 45° plies. *Thin Walled Structures*, 46:860–869, 2008.

[56] L.J. Griffiths and D.J. Martin. A study of the dynamic behaviour of a carbon-fibre composite using the split Hopkinson pressure bar. *Journal of Physics D: Applied Physics*, 7:2329–2341, 1974.

[57] D.J. Chapman, C.H. Braithwaite, and W.G. Proud. The response of Dyneema® to shock-loading. In *American Physical Society, 16th APS Topical Conference on Shock Compression of Condensed Matter 2009*, 2009.

[58] P.J. Hazell, G.J. Appleby-Thomas, X. Trinquant, and D.J. Chapman. In-fiber shock propagation in Dyneema®. *Journal of Applied Physics*, 110:043504, 2011.

[59] B.S. Holmes and F.K. Tsou. Steady shock waves in composite materials. *Journal of Applied Physics*, 43:957–961, 1972.

[60] Y. Oved, G.E. Luttwak, and Z. Rosenberg. Shock wave propagation in layered composites. *Journal of Composite Materials*, 12:84–96, 1978.

[61] S. Zhuang, G. Ravichandran, and D.E. Grady. An experimental investigation of shock wave propagation in periodically layered composites. *Journal of Mechanics and Physics of Solids*, 51:245–265, 2003.

[62] M. Wicklein, S. Ryan, D.M. White, and R.A. Clegg. Hypervelocity impact on CFRP: Testing, material modelling, and numericial simulation. *International Journal of Impact Engineering*, 35:1861–1869, 2008.

[63] R.J. Vignjevic, J.C. Campbell, N. Bourne, O. Matic, and N. Djordjevic. Modelling shock waves in composite materials. In *American Physical Society, 15th APS Topical Conference on Shock Compression of Condensed Matter 2007*, 2007.

[64] A.A. Lukyanov. An equation of state of a carbon-fibre epoxy composite under shock loading. *The European Physical Journal B*, 74:35–45, 2010.

[65] C.E. Anderson, P.A. Cox, G.R. Johnson, and P.J. Maudlin. A constitutive formulation for anisotropic materials suitable for wave propagation computer programs-II. *Computational Mechanics*, 15:201–223, 1994.

[66] Ktech. Staple rayon tape-wrapped carbon phenolic validation: Phase I, mechanicial equation of state. Technical report, 1979.

[67] J.C.F. Millett and N.K. Bourne. The deviatoric response of polymethylmethacrylate to one-dimensional shock loading. *Journal of Applied Physics*, 88:7037–7040, 2000.

[68] J. C. F Millett and N. K. Bourne. The shock induced equation of state of three simple polymers. *Journal of Physics D: Applied Physics*, 37:2901–2907, 2004.

[69] D.E. Munson and R.P. May. Dynamically determined high-pressure compressibilities of three epoxy resin systems. *Journal of Applied Physics*, 43:962–971, 1972.

[70] P.J. Hazell, C. Stennett, and G. Cooper. The shock and release behavior of an aerospace-grade cured aromatic amine epoxy resin. *Polymer Composites*, 29:1106–1110, 2008.

[71] G.J. Appleby-Thomas, P.J. Hazell, and C. Stennett. The variation in lateral and longitudinal stress gauge response within an RTM 6 epoxy resin under one-dimensional shock loading. *Journal of Materials Science*, 44(22):6187–6198, 2009.

[72] J.M. Wilgeroth, P.J. Hazell, and G.J. Appleby-Thomas. The shock response of a rendered porcine fat. *Journal of Applied Physics*, 108:093527, 2010.

[73] G.J. Appleby-Thomas, P.J. Hazell, J.M. Wilgeroth, C.J. Shepherd, D.C. Wood, and A. Roberts. On the dynamic behavior of three readily available soft tissure simulants. *Journal of Applied Physics*, 109:084701, 2011.

[74] C.E. Housecroft and E.C. Constable. *Chemistry*. Pearson, Prentice Hall, Esex, 2006.

[75] T.J. Vogler and L.C. Chhabildas. Strength behavior of materials at high pressures. *International Journal of Impact Engineering*, 33:812–825, 2006.

[76] H.D. Espinosa. On the dynamic shear resistance of ceramic composites and its dependance on applied multiaxial deformation. *International journal of solids and structures*, 32:3105–3128, 1995.

[77] A.S. Abou-Sayed, R.J. Clifton, and L. Hermann. The oblique-plate impact experiment. *Experimental Mechanics*, 16:127–132, 1976.

[78] G. Yuan, R. Feng, and Y.M. Gupta. Compression and shear wave measurements to characterize the shocked state in silicon carbide. *Joural of Applied Physics*, 89:5372–5380, 2001.

[79] L.C. Chhabildas and J.W. Swegle. Dynamic pressure-shear loading of materials using anisotropic crystals. *Joural of Applied Physics*, 51:4799–4807, 1980.

[80] K.J. Frutschy and R.J. Clifton. High-temperature pressure-shear plate impact experiments on OFHC copper. *Journal of the Mechanics and Physics of Solids*, 46:1723–1743, 1998.

[81] S.E. Grunschel, R.J. Clifton, and T. Jiao. Shearing resistance of aluminium at high strain rates and at temperatures approaching melt. In *American Physical Society, 17th APS Topical Conference on Shock Compression of Condensed Matter 2011*, pages 1335–1338, 2012.

[82] E.J. Harris and R.E. Winter. Hydrocode analysis of lateral stress gauges in shocked tantalum. In *American Physical Society, 15th APS Topical Conference on Shock Compression of Condensed Matter 2007*, 2007.

[83] G.T. Gray, N.K. Bourne, and J.C.F Millett. Shock response of tantalum; lateral stress and shear strength through the front. *Journal of Applied Physics*, 94:6430–6436, 2003.

[84] G.J. Appleby-Thomas, P.J.Hazell, J.M. Wilgeroth, and D.C. Wood. On the interpretation of lateral manganin gauge stress measurements in polymers. *Journal of Applied Physics*, 108:033524, 2010.

[85] J. Eliot, E.J. Harris, P.J. Hazell, G.J. Appleby-Thomas, R. Winter, and D.C. Wood. Experimental and computational investigation of lateral gauge response in polycarbonate. In *American Physical Society, 17th APS Topical Conference on Shock Compression of Condensed Matter 2011*, pages 458–461, 2012.

[86] R.E. Winter and E.J. Harris. Simulations of embedded lateral stress gauge profiles in shocked targets. *Journal of Physics D: Applied Physics*, 41:035503, 2008.

[87] J. Lipkin and J.R. Asay. Reshock and release of shock-compressed 6061-T6 aluminium. *Journal of Applied Physics*, 48:182–189, 1977.

[88] H. Huang and J.R. Asay. Compressive strength measurements in aluminium for shock compression over the stress range of 4-22 GPa. *Journal of Applied Physics*, 98:033524, 2005.

[89] N.K. Bourne. A 50 mm bore gas gun for dynamic loading of materials and structures. *Measurement Science And Technology*, 14:273–278, 2003.

[90] G.J. Appleby-Thomas, P.J. Hazell, C. Stennett, G. Cooper, K. Helaar, and A.M. Diederen. Shock propagation in a cemented tungsten carbide. *Journal of Applied Physics*, 105:064916, 2009.

[91] E. Barsis, E. Williams, and C. Skoog. Piezoresistivity coefficients in manganin. *Journal of Applied Physics*, 41:5155–5162, 1970.

[92] Vishay Precision Group Micro-Measurements. Manganin gauge datasheet. Website http://www.vishaypg.com/micro-measurements/list/product-11524/ acsessed on 07/03/2011.

[93] Y. Partom, D. Yaziv, and Z. Rosenberg. Theoreticial account for the response of manganin gauges. *Journal of Applied Physics*, 52:4610–4616, 1981.

[94] Z. Rosenberg and Y. Partom. Longitudinal dynamic stress measurements with in-material piezoresistive gauges. *Journal of Applied Physics*, 58:1814–1818, 1985.

[95] Z. Rosenberg, Y. Partom, M. Mayseless, and J. Falcovitz. Determination of stress-time histories in axially symmetric impacts with the two-gauge technique. *Journal of Applied Physics*, 54:1434–1439, 1984.

[96] Z. Rosenberg, N.K. Bourne, and J.C.F. Millett. On the effect of manganin gauge geometries upon their response to lateral stress. *Measurement Science and Technology*, 18:1843–1847, 2007.

[97] Dynasen Incorporated. Piezoresistive pulse power supply model CK2-50/0.050-300 instruction manual. Technical report, 20 Arnold Place, Goleta, California 93117, January 1994.

[98] Olympus NDT. Olympus ultrasonic transducers technicial notes. Technical report, 2006.

[99] C. Stennett, G. Cooper, P.J. Hazell, and G.J. Appleby-Thomas. Initiation of secondary explosives measured using embedded electromagnetic gauge. In *American Physical Society, 16th APS Topical Conference on Shock Compression of Condensed Matter 2009*, pages 267–270, 2009.

[100] J.C.F. Millett and N.K. Bourne. Shock and release of polycarbonate under one-dimensional strain. *Journal of Materials Science*, 41(6):1683–1690, 2006.

[101] G.J. Appleby-Thomas, P.J. Hazell, D.C. Wood, J.M. Wilgeroth, and J.A. Leighs. On the effects of lateral gauge misalignment in shocked targets. *Review of Scientific Instruments*, 83:063904, 2012.

[102] P.J. Hazell, G.J. Appleby-Thomas, E. Wielewski, C. Stennett, and C. Siviour. The influence of microstructure on the shock and spall behaviour of the magnesium alloy, Electron 675. *Acta Materialia*, 60:6042–6050, 2012.

Appendix A

Shock wave traces

A.1 Traces for the phenolic resin SC-1008

A.1.1 Longitudinal traces

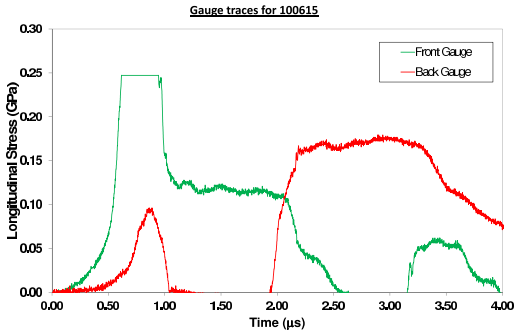

Figure A.1: 10 mm aluminium projectile impacting at 80 m s^{-1} with confinement method.

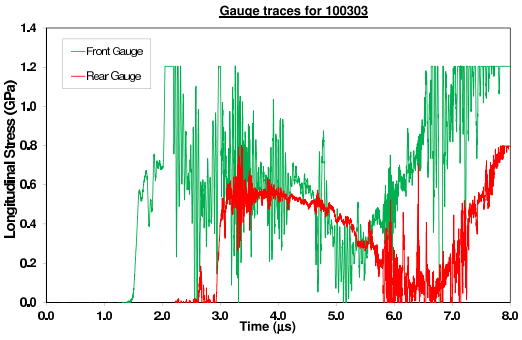

Figure A.2: 10 mm aluminium projectile impacting at 200 m s^{-1} without confinement method.

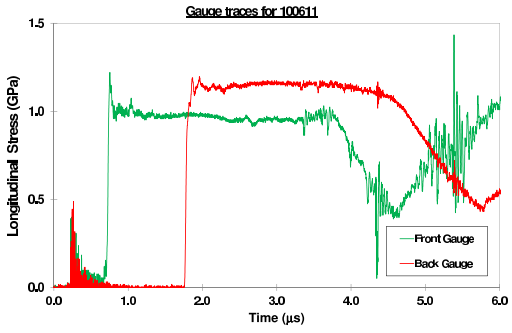

Figure A.3: 10 mm aluminium projectile impacting at 350 m s^{-1} with confinement method.

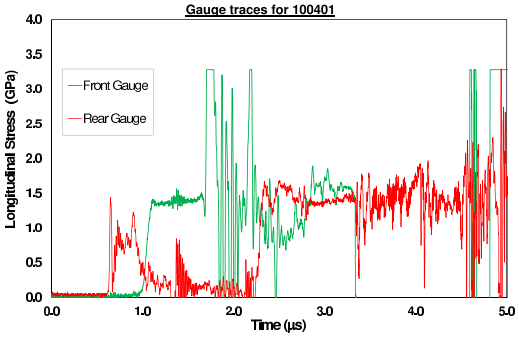

Figure A.4: 10 mm aluminium projectile impacting at 450 m s^{-1} without confinement method.

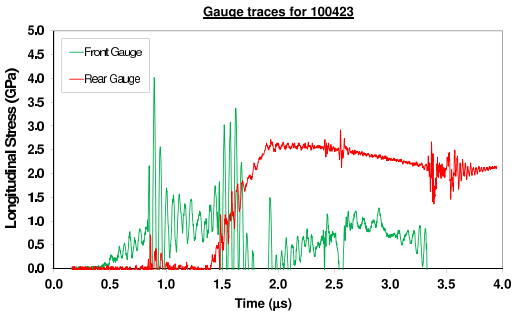

Figure A.5: 10 mm copper projectile impacting at 600 m s^{-1} without confinement method.

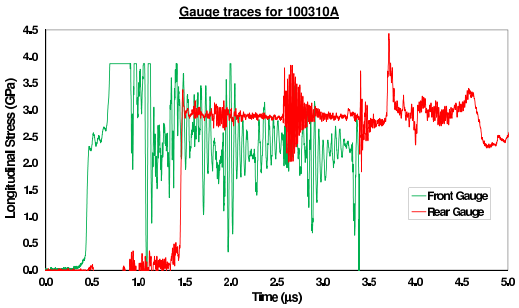

Figure A.6: 10 mm Aluminium projectile impacting at 810 m s^{-1} without confinement method.

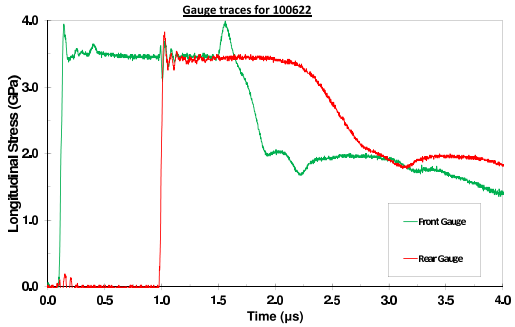

Figure A.7: 5 mm aluminium projectile impacting at 960 m s^{-1} with confinement method.

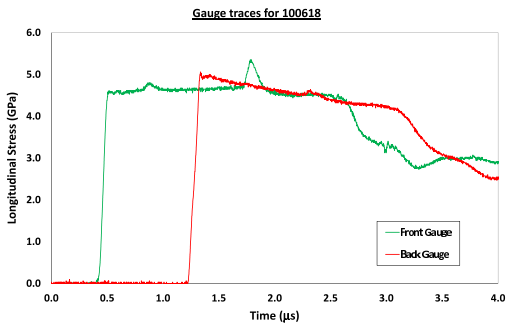

Figure A.8: 5 mm copper projectile impacting at 970 m s^{-1} without confinement method.

A.1.2 Lateral traces

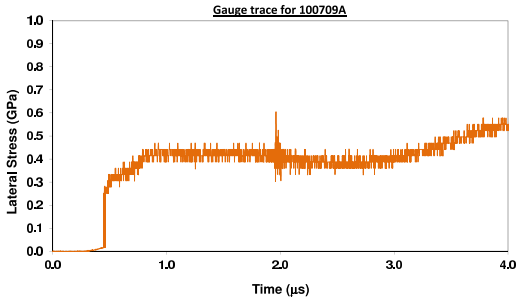

Figure A.9: 10 mm aluminium projectile impacting at 145 m s^{-1} with confinement method.

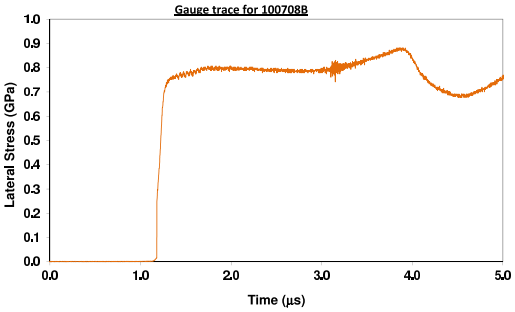

Figure A.10: 10 mm aluminium projectile impacting at 320 m s^{-1} with confinement method.

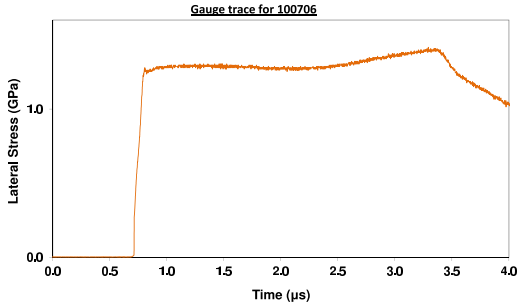

Figure A.11: 10 mm aluminium projectile impacting at 500 m s^{-1} with confinement method.

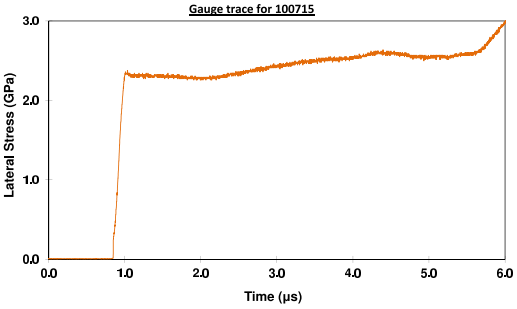

Figure A.12: 10 mm copper projectile impacting at 670 m s^{-1} with confinement method.

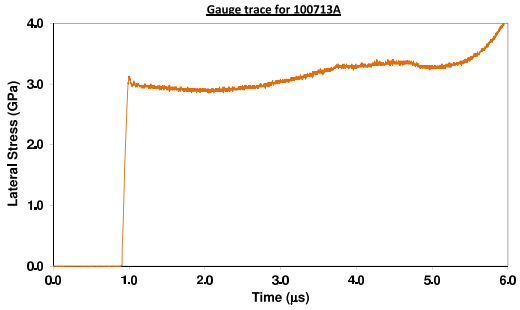

Figure A.13: 10 mm copper projectile impacting at 865 m s^{-1} with confinement method.

A.2 Traces for the TWCP with the 0° weave orientation

A.2.1 Longitudinal traces

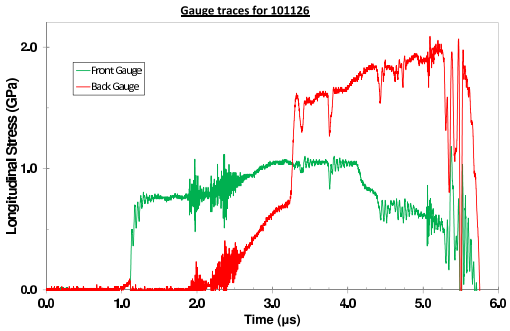

Figure A.14: 10 mm aluminium projectile impacting at 197 m s^{-1}.

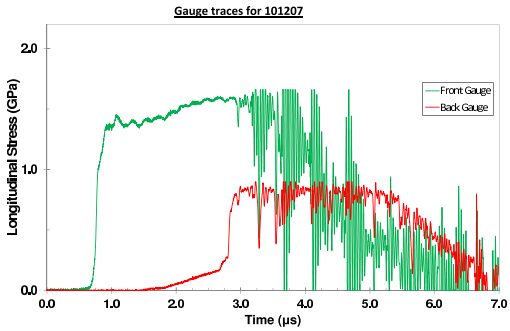

Figure A.15: 10 mm aluminium projectile impacting at 350 m s^{-1}.

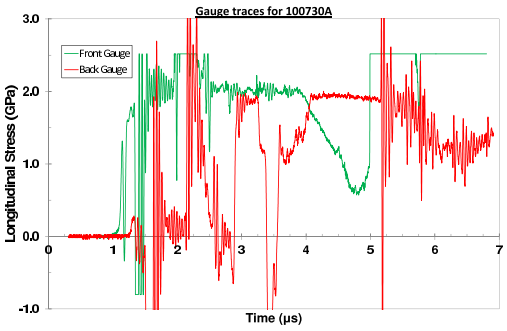

Figure A.16: 10 mm aluminium projectile impacting at 500 m s^{-1}.

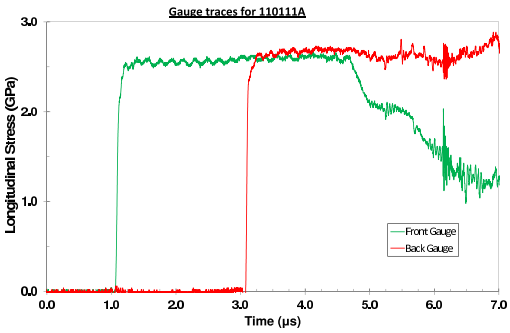

Figure A.17: 10 mm copper projectile impacting at 530 m s^{-1}.

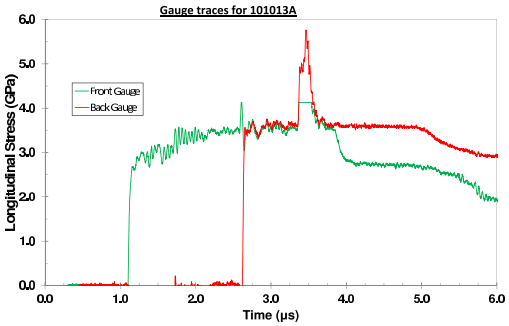

Figure A.18: 10 mm copper projectile impacting at 679 m s^{-1}.

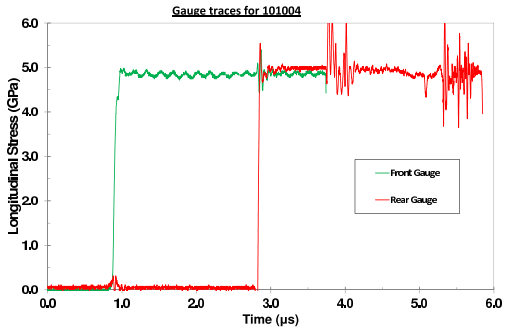

Figure A.19: 10 mm copper projectile impacting at 869 m s^{-1}.

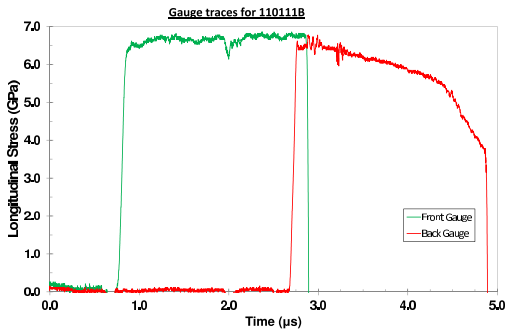

Figure A.20: 10 mm copper projectile impacting at 1000 m s^{-1}.

A.2.2 Lateral traces

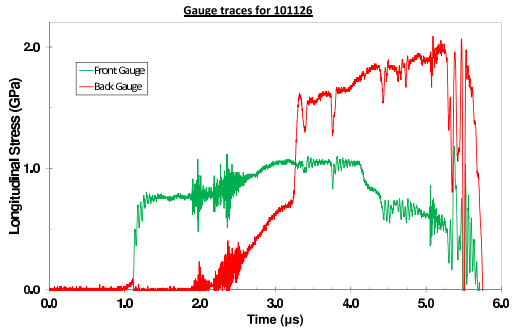

Figure A.21: 10 mm aluminium projectile impacting at 197 m s^{-1}.

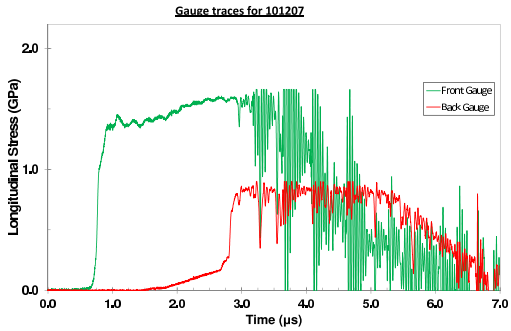

Figure A.22: 10 mm aluminium projectile impacting at 350 m s^{-1}.

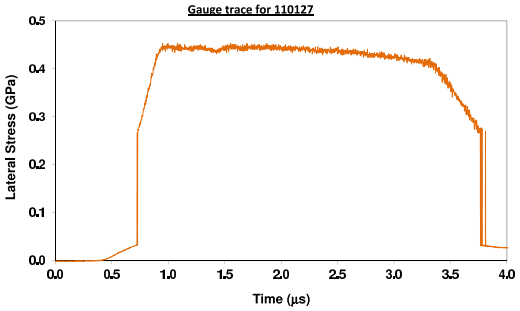

Figure A.23: 10 mm aluminium projectile impacting at 200 m s^{-1}.

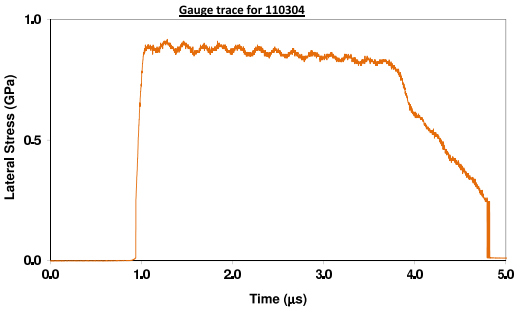

Figure A.24: 10 mm aluminium projectile impacting at 350 m s^{-1}.

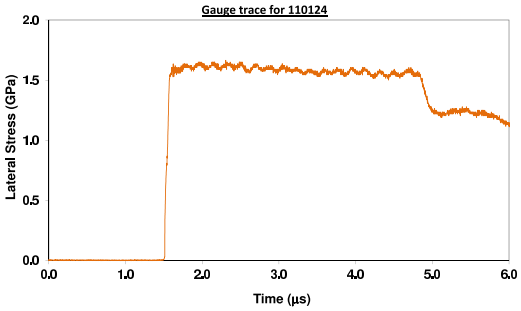

Figure A.25: 10 mm copper projectile impacting at 520 m s^{-1}.

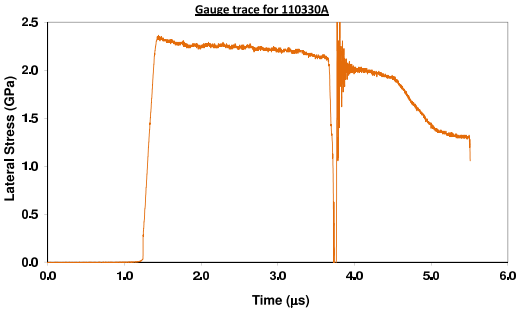

Figure A.26: 10 mm copper projectile impacting at 667 m s^{-1}.

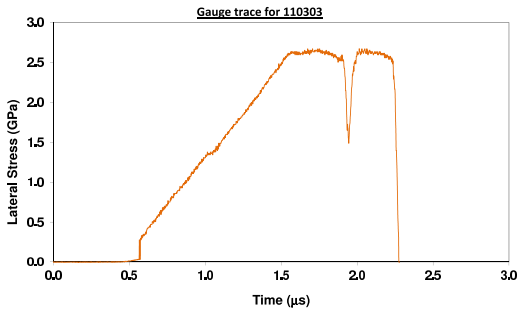

Figure A.27: 10 mm copper projectile impacting at 900 m s^{-1}.

A.3 Traces for the TWCP with the 90° weave orientation

A.3.1 Longitudinal traces

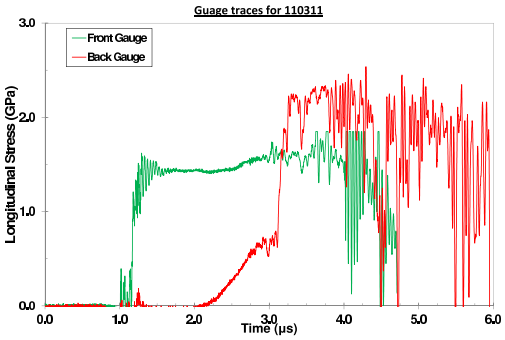

Figure A.28: 10 mm aluminium projectile impacting at 353 m s^{-1}.

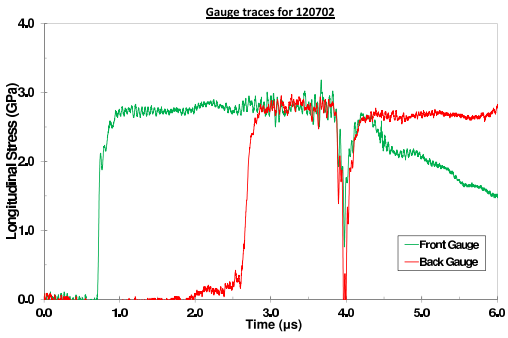

Figure A.29: 10 mm aluminium projectile impacting at 530 m s^{-1}.

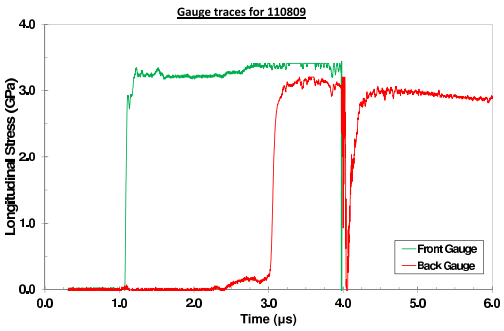

Figure A.30: 10 mm aluminium projectile impacting at 600 m s^{-1}.

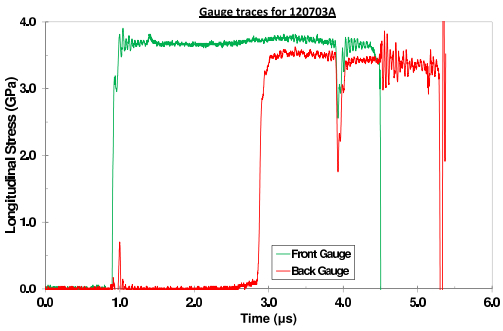

Figure A.31: 10 mm copper projectile impacting at 689 m s^{-1}.

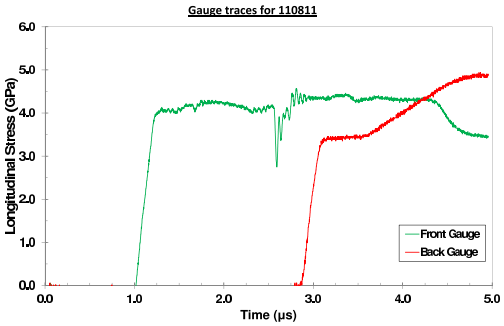

Figure A.32: 10 mm copper projectile impacting at 834 m s^{-1}.

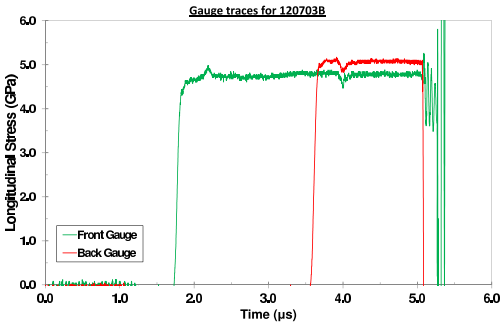

Figure A.33: 10 mm copper projectile impacting at 890 m s^{-1}.

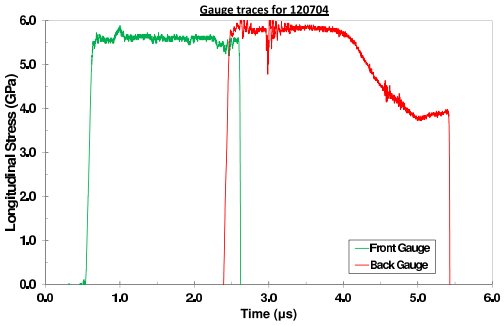

Figure A.34: 5 mm copper projectile impacting at 1016 m s^{-1}.

A.3.2 Longitudinal traces with PMMA offset for protection of the rear gauge

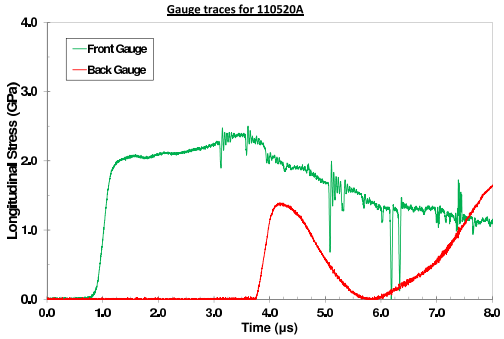

Figure A.35: 10 mm aluminium projectile impacting at 549 m s^{-1}.

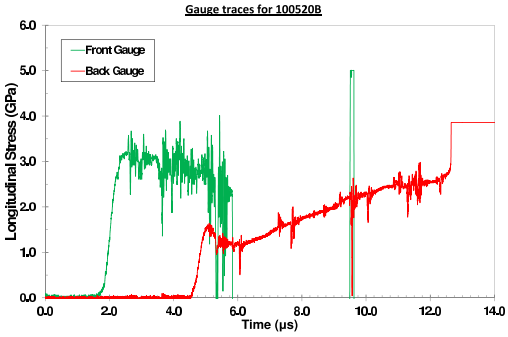

Figure A.36: 10 mm copper projectile impacting at 580 m s^{-1}.

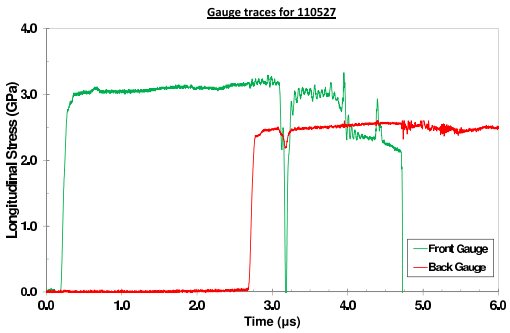

Figure A.37: 10 mm copper projectile impacting at 625 m s^{-1}.

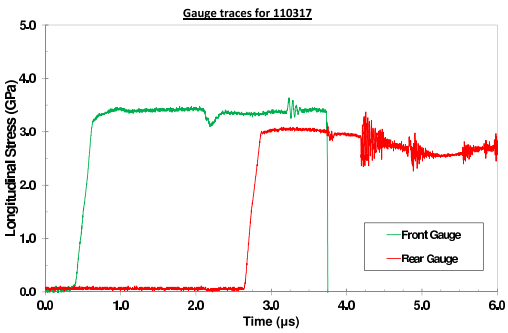

Figure A.38: 10 mm copper projectile impacting at 667 m s^{-1}.

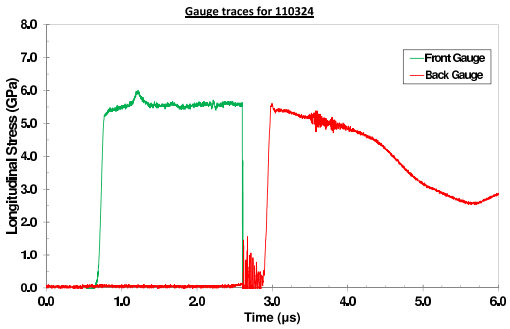

Figure A.39: 5 mm aluminium projectile impacting at 1000 m s^{-1}.

A.3.3 Experimental traces for lateral and longitudinal experiments combined as well as lateral experiments

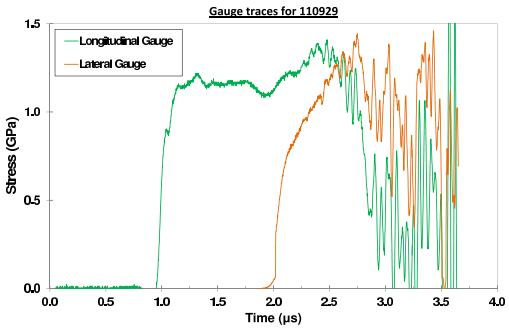

Figure A.40: 5 mm aluminium projectile impacting at 292 m s^{-1}.

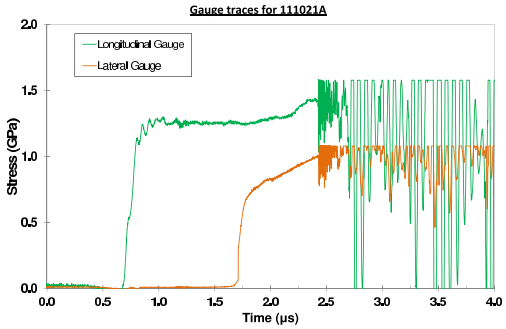

Figure A.41: 10 mm aluminium projectile impacting at 312 m s^{-1}.

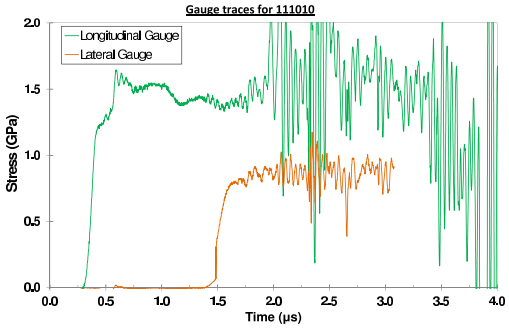

Figure A.42: 10 mm aluminium projectile impacting at 350 m s^{-1}.

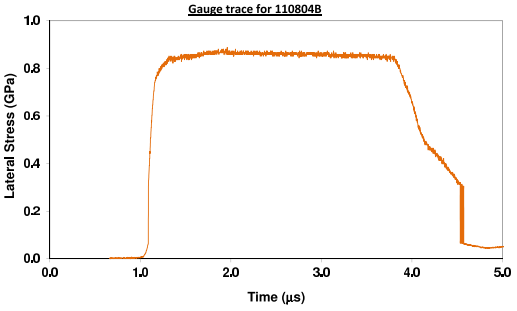

Figure A.43: 10 mm aluminium projectile impacting at 350 m s^{-1}.

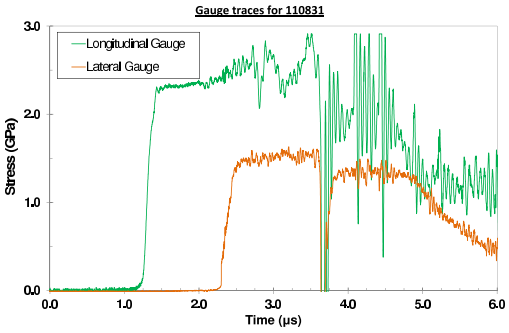

Figure A.44: 10 mm aluminium projectile impacting at 538 m s^{-1}.

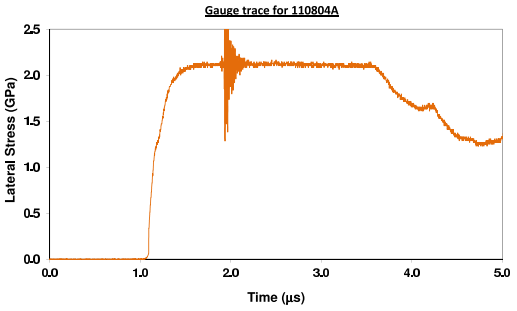

Figure A.45: 10 mm aluminium projectile impacting at 632 m s^{-1}.

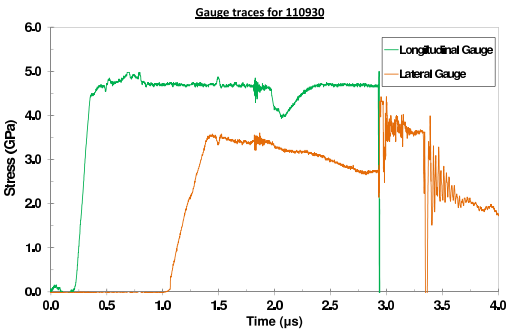

Figure A.46: 10 mm copper projectile impacting at 908 m s^{-1}.

A.4 Traces for the TWCP with the 25° weave orientation

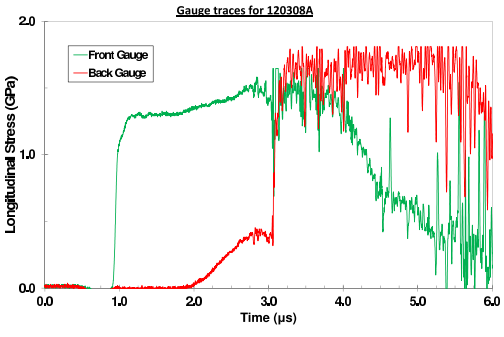

Figure A.47: 10 mm aluminium projectile impacting at 330 m s^{-1}.

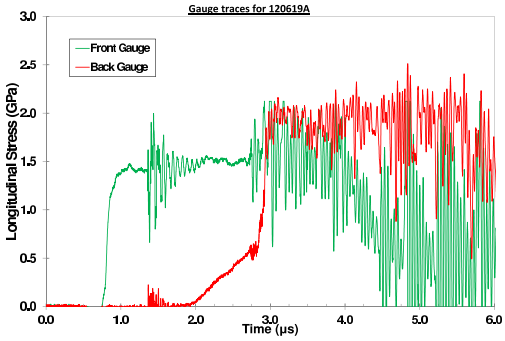

Figure A.48: 10 mm aluminium projectile impacting at 349 m s^{-1}.

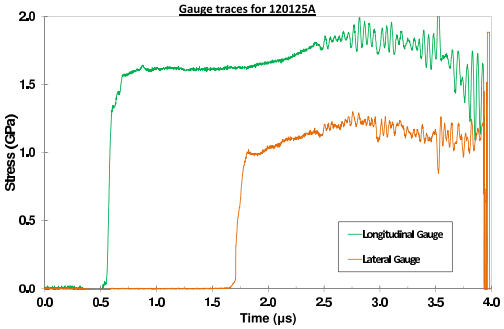

Figure A.49: 10 mm aluminium projectile impacting at 397 m s^{-1}.

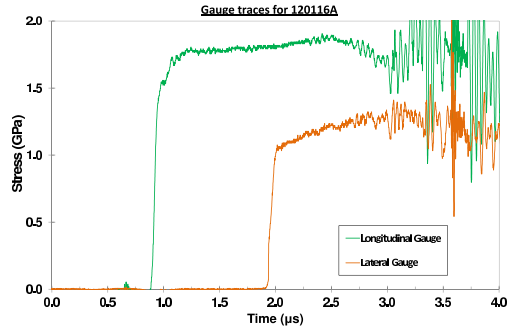

Figure A.50: 10 mm aluminium projectile impacting at 437 m s^{-1}.

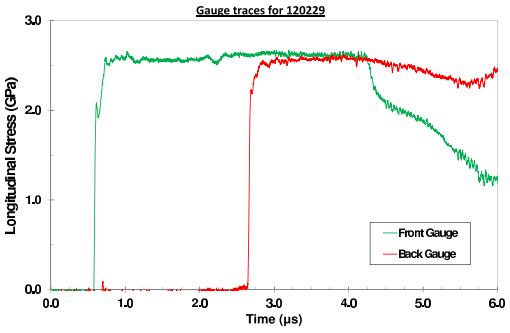

Figure A.51: 10 mm copper projectile impacting at 508 m s^{-1}.

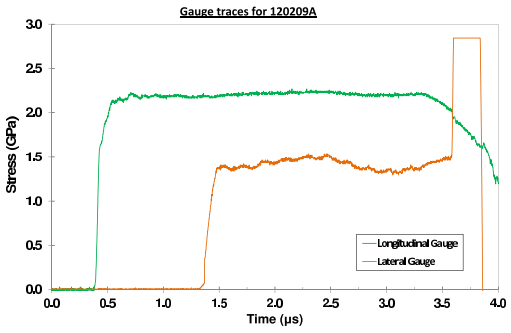

Figure A.52: 10 mm aluminium projectile impacting at 534 m s^{-1}.

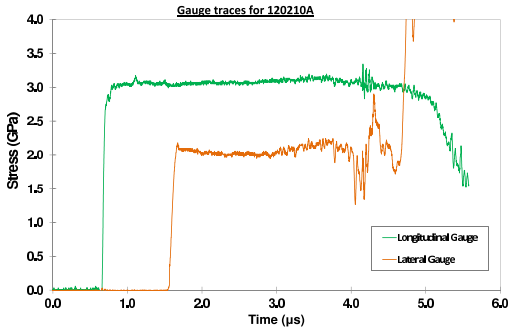

Figure A.53: 10 mm copper projectile impacting at 600 m s^{-1}.

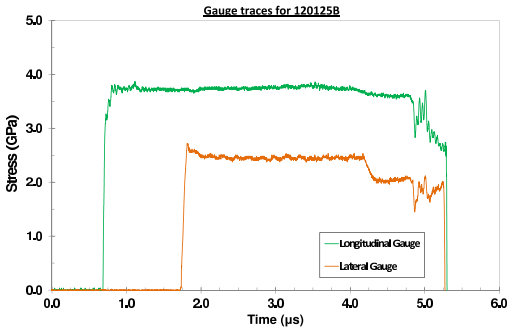

Figure A.54: 10 mm copper projectile impacting at 691 m s^{-1}.

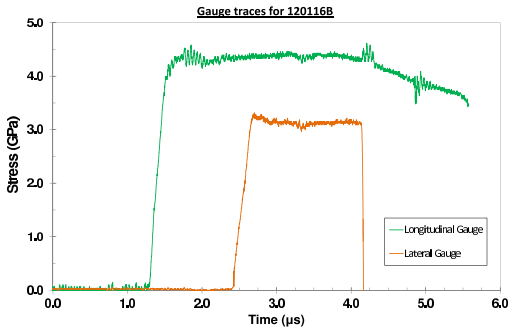

Figure A.55: 10 mm copper projectile impacting at 822 m s^{-1}.

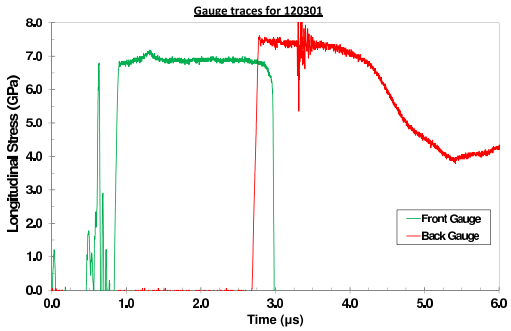

Figure A.56: 5 mm copper projectile impacting at 1155 m s^{-1}.

A.5 Traces for the TWCP with the 45° weave orientation

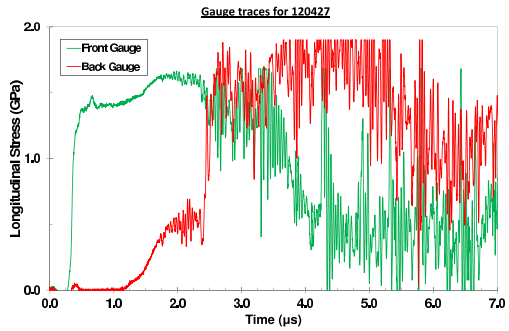

Figure A.57: 10 mm aluminium projectile impacting at 350 m s^{-1}.

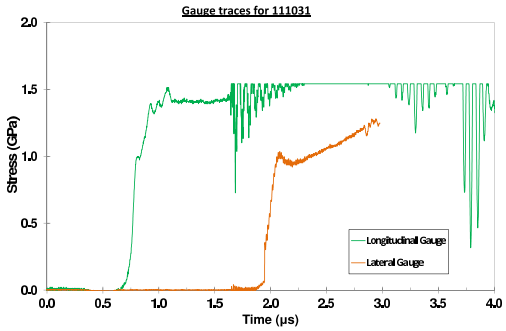

Figure A.58: 10 mm aluminium projectile impacting at 351 m s^{-1}.

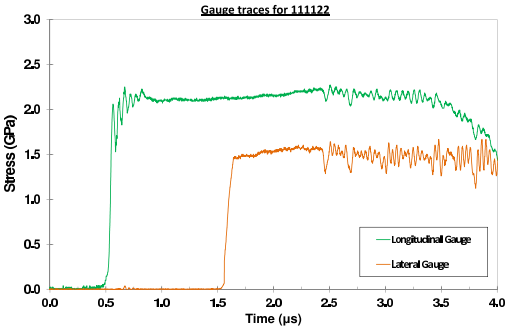

Figure A.59: 10 mm aluminium projectile impacting at 538 m s^{-1}.

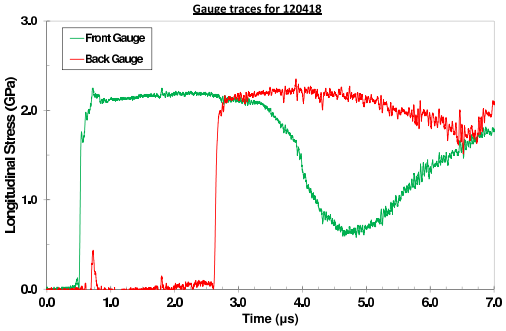

Figure A.60: 10 mm aluminium projectile impacting at 548 m s^{-1}.

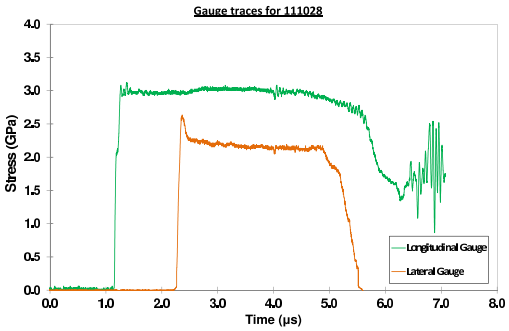

Figure A.61: 10 mm copper projectile impacting at 579 m s^{-1}.

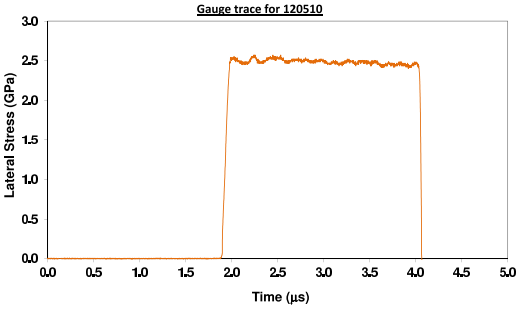

Figure A.62: 10 mm copper projectile impacting at 676 m s^{-1}.

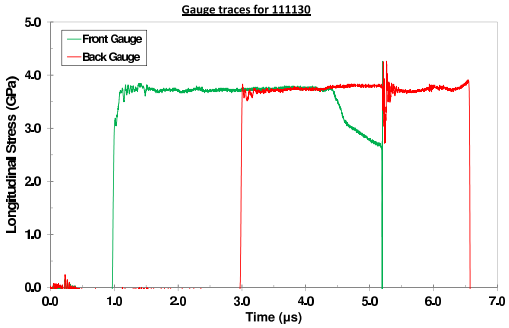

Figure A.63: 10 mm copper projectile impacting at 679 m s^{-1}.

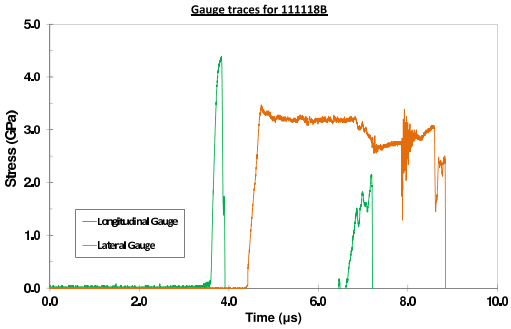

Figure A.64: 10 mm copper projectile impacting at 824 m s^{-1}.

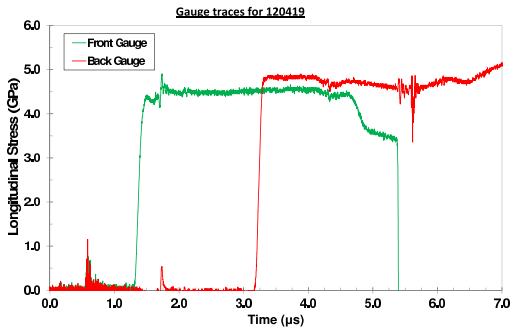

Figure A.65: 10 mm copper projectile impacting at 839 m s^{-1}.

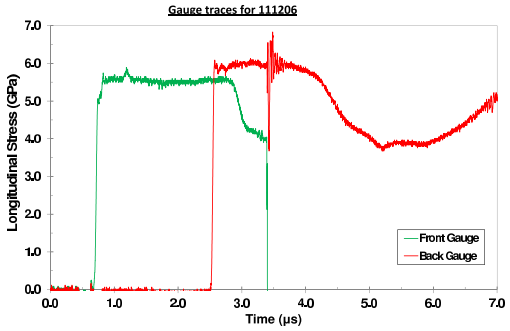

Figure A.66: 5 mm copper projectile impacting at 983 m s^{-1}.